Prediction of Axial Compressor Blade Vibration by Modelling Fluid-Structure Interaction

by

Jacobus Daniël Brandsen

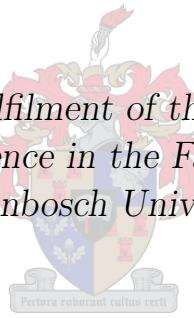

Thesis presented in fulfilment of the requirements for the degree of Master of Science in the Faculty of Engineering at Stellenbosch University

Supervisors:

Dr S. J. van der Spuy
Prof G. Venter

December 2013

Declaration

By submitting this thesis electronically, I declare that the entirety of the work contained therein is my own, original work, that I am the sole author thereof (save to the extent explicitly otherwise stated), that reproduction and publication thereof by Stellenbosch University will not infringe any third party rights and that I have not previously in its entirety or in part submitted it for obtaining any qualification.

Date: .....

Abstract

The Council for Scientific and Industrial Research has developed a vibration excitation system. The system is designed to excite the rotor blades of an axial compressor in the specified vibration mode and at the specified frequency. The vibration excitation system was tested on Stellenbosch University's Rofanco compressor test bench. A two-way staggered fluid-structure interaction (FSI) model was created that was capable of simulating the vibration of the rotor blades excited by the system. The results of the FSI model were verified using available experimental data. It was concluded that the FSI model is able to recreate the vibration excited by the system to within the desired level of accuracy. In addition, the results of the FSI model showed that the vibration excitation system should be able to excite the blades in the selected vibration mode and at the selected frequency provided that the excitation frequency is close the natural frequency of the first bending mode. The results also suggested that a transient computational fluid dynamics model should be sufficient for the prediction of the aerodynamic forces acting on the rotor blades. Furthermore, a one-way staggered FSI model should be adequate for calculating the motions of the blades.

Opsomming

Die Wetenskaplike en Nywerheidnavorsingsraad het 'n vibrasie-opwekkingstelsel ontwerp om die rotorlemme van 'n aksiaalvloei kompressor in die gespesifiseerde vibrasiemodus en teen die gespesifiseerde frekwensie op te wek. Die vibrasie-opwekkingstelsel is met behulp van die Universiteit Stellenbosch se Rofanco kompressortoetsbank getoets. Daarna is 'n tweerigting vloeistof-struktuur-interaksie model geskep om die vibrasie van die rotorlemme, wat deur die stelsel opgewek is, te simuleer. Beskikbare eksperimentele data is gebruik om die resultate van die vloeistof-struktuur-interaksie model te bevestig. Die gevolgtrekking is gemaak dat die model wél die vibrasie van die lemme met die nodige akkuraatheid kan simuleer. Die resultate van die vloeistof-struktuur-interaksie model toon ook dat die stelsel die lemme in die gekose vibrasiemodus en teen die gekose frekwensie behoort te kan opwek, solank die opwekkingsfrekwensie na aan die natuurlike frekwensie van die eerste buigmodus is. Voorts dui die resultate daarop dat 'n berekeningsvloeimeganika model die aërodinamiese laste van die lemme sal kan voorspel. 'n Eenrigting vloeistof-struktuur-interaksie model behoort voldoende te wees om die beweging van die rotorlemme te bereken.

Acknowledgements

The financial assistance of the National Research Foundation (NRF) towards this research is hereby acknowledged. Opinions expressed and conclusions arrived at, are those of the author and are not necessarily to be attributed to the NRF.

I would like to thank my supervisors Dr Johan Van der Spuy and Prof Gerhard Venter for all of their support and guidance, on both a personal and an academic level, throughout the duration of the project. I would also like to thank them for assisting me in getting the funding in place that made this thesis project possible.

I would like to express my gratitude for the funding provided by Project BALLAST.

Thank you to Richard Hamman for his advice and assistance with the simulation software packages used during the project, and for generating the files required to define the model geometry.

Thank you to Andrew Gill and Gert Raubenheimer for providing much of the experimental data used during the project, and for helping me with the additional experimental work conducted.

Finally, I would like to thank my parents, my brother Tiaan, my sister Hetitia and her husband Adrian, and my friends. This thesis project would not have been possible without their constant support and encouragement.

Contents

List of Figures

List of Tables

Nomenclature

Scalar variables

E	Voltage
f	Frequency
GF	Gauge factor
$\hat{l}_i$	Amplitude of l_i
N_{bl}	Number of blades
N_{ex}	Number of exciters
N_{ND}	Number of nodal diameters
N_{pb}	Number of patch boundary
n	Number of degrees of freedom
$\hat{q}_i$	Amplitude of the particular solution of q_i
$\hat{r}_{\text{perp}}$	Amplitude of the resultant force perpendicular to the blade root
T	Temperature
t	Time
Δt	Integration time step size
V	Absolute velocity component
y^+	Wall coordinate
α	Mass matrix multiplier for Rayleigh damping
β	Stiffness matrix multiplier for Rayleigh damping
ϵ_{b}	Bending strain detected by pressure side strain gauge
δ	Tip displacement perpendicular to the blade root

ζ_i	Damping ratio of the ith mode
ϕ	Phase angle
$\Delta\phi$	Difference in phase angle
ω	Angular frequency

Vectors and matrices

$\mathbf{C}$	Damping matrix
$\mathbf{d}$	Degrees of freedom
$\mathbf{I}$	Identity matrix
$\mathbf{K}$	Stiffness matrix
$\mathbf{M}$	Mass matrix
$\mathbf{P}$	Matrix of normalized mode shapes
$\mathbf{r}$	Vector of forces acting on the degrees of freedom
$\hat{\mathbf{r}}$	Amplitudes of the forces acting on the degrees of freedom
$\mathbf{l}$	Vector of forces in the modal coordinate system
$\mathbf{q}$	Modal coordinate system
$\mathbf{u}_i$	Mode shape of the ith mode
$\mathbf{v}_i$	Normalized mode shape of the ith mode
$\mathbf{x}$	Variables representing the solution to a system of equations
$\mathbf{\Omega}$	Diagonal matrix of natural frequencies
$\mathbf{\Gamma}$	Damping matrix for the model coordinate system

Subscripts

ab	Adjacent blades
aj	Adjacent nozzle jets
be	Bridge excitation
br	Bridge
b3	Blade 3 in the actual compressor

b25	Blade 25 in the actual compressor
br3	Bridge voltage for blade 3
br25	Bridge voltage for blade 25
c, i	ith term of the complimentary solution of $\mathbf{d}$
corr	Corrected
cq, i	Complimentary solution of q_i
d, i	Damped natural frequency of the ith mode
ef	Excitation frequency
f	Fluid domain
fl	Fluid
m	Measured
max	Maximum
n, i	Undamped natural frequency of the ith mode
part	Particular solution
pq, i	Particular solution of q_i
pu	Pulsation
r	Radial
cal	Calibration
rot	Rotation
s	Structural domain
w	Hot wires of the x-probe
z	Axial
0	Value at $t = 0$

Abbreviations

CFD	Computational fluid dynamics
CSIR	Council for Scientific and Industrial Research

DC	Direct current
FE	Finite element
FFT	Fast Fourier Transform
FP7	Seventh Framework Program
FSI	Fluid-structure interaction
FUTURE	Flutter-Free Turbomachinery Blades
ND	Nodal diameter
ODE	Ordinary differential equations

Chapter 1

Introduction

This chapter begins by describing the background of the thesis project, and the motivations for undertaking it. The project goal and objectives are then examined. The chapter concludes with a description of the layout of this thesis document.

1.1 Background and motivations

Flutter is the vibration of a mechanical system, at or near its natural frequency, due to aeroelastic instability (Cumpsty, 1989). Aeroelastic instability refers to a situation where the aerodynamic forces, induced by the vibration of the system, feed energy into the system during each period of vibration. This, in turn, causes the amplitude of vibration to increase with each period of vibration (Srinivasan, 1997). Since flutter is the result of instability, no disturbance is required to excite it (Cumpsty, 1989).

Blade flutter is a cause of high cycle fatigue failure in turbomachinery (Srinivasan, 1997). According to El-Aini *et al.* (1997), only 10 % of high cycle fatigue problems make it through development testing. However, these problems represent 30 % of the total development cost of aircraft engines, and 25 % of all engine distress events (El-Aini *et al.*, 1997). Project FUTURE was initiated with the aim of improving the methods used to model flutter, and the design practices adopted in order to prevent its occurrence. Project FUTURE is part of the European Seventh Framework Program (FP7). The project is coordinated by the Swedish university Kungliga Teknista Högskolan. Project FUTURE also has 25 other partners, including Stellenbosch University and the Council for Scientific and Industrial Research (CSIR).

As part of Project FUTURE, the CSIR have developed a vibration excitation system. The vibration excitation system is designed to excites the rotor blades of an axial flow compressor at the specified frequency and in the specified vibration mode. The system consists of 15 exciters that are attached to the outside of

the compressor casing. Each exciter injects additional air, from a pressurised air supply, into the compressor flow path through an opening in the shroud wall. This creates a pulsating jet downstream of each exciter. The pulsating jet induces perturbations in the compressor velocity field which, in turn, excites the rotor blades. The vibration excitation system was created for use in a series of experiments at the Technical University of Darmstadt in Germany. Stellenbosch University was tasked with demonstrating the capabilities of the system before it was transported to Darmstadt. The system was therefore fitted to Stellenbosch University's Rofanco compressor test bench.

Raubenheimer (2011) conducted a series of experiments, using a prototype version of the excitation system, on the Rofanco test bench. The prototype excitation system consisted of only a single exciter and not the full complement of fifteen. During these experiments, Raubenheimer (2011) measured the amplitude of the velocity perturbations induced by the prototype excitation system. Two of the blades in the first rotor blade row were also each fitted with a half-bridge strain gauge assembly. The strain gauge assembly was used by Raubenheimer (2011) to record the vibration of each rotor blade.

The measurements of the velocity perturbations were used by Raubenheimer (2011) to construct a computational fluid dynamics (CFD) model of an excitation system consisting of 15 prototype exciters. Raubenheimer (2011) also calculated a Fast Fourier Transform (FFT) from the aerodynamic force acting on each blade in the CFD model. The FFT revealed that the blade force contained a component at the excitation frequency. However, the blade force also exhibited a number of additional components. The most prominent component occurred at what Raubenheimer (2011) referred to as the nozzle bypass frequency. This component was caused by the motion of the rotor blades through each of the nozzle jets as the compressor rotates (Raubenheimer, 2011). The amplitude of the component at the nozzle bypass frequency was significantly larger than the component observed at the excitation frequency (Raubenheimer, 2011).

The strain data collected by Raubenheimer (2011) partially verified the results from the CFD model. The strain data was measured with the compressor switched off. A FFT of the strain data showed that, when the prototype exciter is firing at the stationary rotor blades, the excitation frequency is indeed detectable in the blade response (Raubenheimer, 2011). The FFT also showed that the blade response contained a component at the natural frequency of the first bending mode (Raubenheimer, 2011). However, the strain data did not reveal the effect of the secondary components of the blade force, such as the component at the nozzle bypass frequency, on the blade response. The strain measurements also did not confirm whether the prototype system could excite the rotor blades at the desired frequency when the compressor is operating. Furthermore, the prototype excitation system could not be used to determine whether it is possible to excite the rotor blade row in the desired mode shape.

The capabilities of the complete vibration excitation system, consisting of 15 exciters, were tested on the Rofanco test bench by Van der Spuy *et al.* (2012).

A portion of the tests consisted of using the strain gauge assemblies to measure the response of the rotor blades for several different settings of the vibration excitation system. The strain measurements showed that the system is indeed able to excite the rotor blades, while the compressor is in operation, at the desired frequency. However, the vibration excitation system was only able to do this if the excitation frequency was sufficiently close to the natural frequency of the first bending mode of each blade (Van der Spuy *et al.*, 2012). The strain data also confirmed that the blade response contained components at the natural frequency of the first bending mode, the nozzle bypass frequency, and at other multiples of the rotation frequency of the compressor. However, since only strain data for two of the rotor blades were available, the strain data did not verify that the system is capable of exciting the entire rotor blade row in the desired vibration mode.

The goal of this thesis project was to construct a fluid-structure interaction (FSI) model which is capable of simulating the motions of the rotor blades induced by the complete vibration excitation system. The motivations for creating such an FSI model are two-fold. Firstly, the FSI model will serve as a useful numerical tool that will allow vibration excitation experiments to be carried out digitally. Secondly, the results from the FSI model can provide additional information which complement the already existing experimental data. The strain data gathered by Raubenheimer (2011) and Van der Spuy *et al.* (2012) only contains the strain measurements of two of the rotor blades, and at one point along the span of each blade. The FSI model, on the other hand, allows the entire displacement, stress, or strain field of each rotor blade to be obtained. The FSI model is therefore able to provide additional insight into the operation of the vibration excitation system that cannot be deduced from the existing experimental data. Further examples of the information that can be provided by the FSI model include the pressure distribution on the blade surface, regions of flow separation, and other features of the compressor flow field.

Im and Zha (2012) used a FSI model to simulate the vibration of the blades in an axial flow compressor. A FSI model was also utilised by Gnesin *et al.* (2000) to simulate the motions of the blades in an axial flow turbine. The FSI models used by Im and Zha (2012) and Gnesin *et al.* (2000) were in both cases constructed by coupling a transient CFD model of the air flow through the compressor or turbine, respectively, to a finite element (FE) model of the structure of the blades. The work of Im and Zha (2012) and Gnesin *et al.* (2000) demonstrated that a FSI model constructed in this manner could be used to successfully predict the vibration of turbomachinery blades.

The transient CFD model created by Raubenheimer (2011) in order to replicate the operation of the prototype excitation system treated the rotor blades of the Rofanco compressor as though the blades were perfectly rigid. The transient CFD model of Raubenheimer (2011) could therefore not predict the motions of the blades caused by the aerodynamic forces. The transient CFD model also did not account for the effect of the motions of the rotor blades on the aerodynamic

forces. However, the transient CFD model utilised by Raubenheimer (2011) included the pulsating nozzle jets of the prototype excitation system which were not present in the simulations of Im and Zha (2012) and Gnesin *et al.* (2000). In order to create a FSI model of the operation of the complete vibration excitation system, the additional complexity of the pulsating nozzle jets from the work of Raubenheimer (2011) must therefore be combined with the FSI modelling techniques already demonstrated by Im and Zha (2012) and Gnesin *et al.* (2000).

1.2 Objectives

As stated in section 1.1, the goal of the project was to create a FSI model that simulates the vibration of the rotor blades excited by the vibration excitation system. Due to time constraints, three restrictions were placed on the goal. Despite these restrictions, the FSI model should still be capable of reproducing and complementing a large the portion of the existing experimental data.

- The FSI model only has to be able to simulate the vibration of the rotor blades for a single specific combination of excitation frequency and supply pressure. The specific combination selected was where the vibration excitation system had been set to an excitation frequency near 650 Hz and a compressed air supply pressure of 2.5 bar. As will be explained in section 3.4, this combination of excitation frequency and supply pressure best complimented the already existing experimental data.

- The component of the blade motion occurring at the excitation frequency is the component that the vibration excitation system is designed to induce. This component was therefore considered of primary importance. It was thus decided that the FSI model only needs to be able to predict this component of the blade motion with sufficient accuracy.

- Only the FSI model's ability to simulate the 0 nodal diameter and +2 nodal diameter preset vibration modes of the system need to be demonstrated. However, if the FSI model can replicate these two modes of operation, then it should also be able to simulate the other preset vibration modes after minor modifications. When the vibration excitation system is set to the 0 nodal diameter and +2 nodal diameter preset vibration modes, the vibration excitation system is designed excite the first rotor blade row of the compressor in the 0 nodal diameter mode and +2 nodal diameter mode, respectively. The 0 nodal diameter mode consists of the first rotor blade row vibrating in such a manner that the motions of all of the blades are in phase. The motions of adjacent blades in the first rotor blade row should be out of phase by $720°/N_{\text{bl}}$ when the blade row is vibrating in the +2 nodal diameter mode. The variable N_{bl} is the number of blades in the first rotor blade row.

In order to achieve the goal, the following objectives had to be accomplished:

1. Perform experiments in order to quantify the velocity perturbations caused by the complete vibration excitation system. This data is required for the boundary conditions of the FSI model.
2. Construct and verify the finite element (FE) model of the first rotor blade row.
3. Construct and verify the CFD model of the first rotor blade row and the vibration excitation system.
4. Couple the FE and CFD models to form the FSI model. Use the FSI model to simulate the 0 nodal diameter and +2 nodal diameter excitation modes of the system.

1.3 Thesis outline

A literature study was conducted throughout the duration of the project. The results of this literature study are discussed in chapter 2. Chapter 3 covers the experimental work performed in order to quantify the velocity perturbations induced by the vibration excitation system. Details of the structural FE model created of the first rotor blade row are provided in chapter 4. This is followed by the examination of the CFD model of the first rotor blade row and the vibration excitation system in chapter 5. Chapter 6 begins with an overview of the modifications made to the FE and CFD models so that they could be coupled to form the FSI model. The simulation of the 0 nodal diameter and +2 nodal diameter modes is then considered. The thesis concludes with a discussion of the results obtained in chapter 7. Recommendations for future work are also provided.

Chapter 2

Relevant concepts and theory

A literature study was conducted throughout the duration of the project. The relevant theoretical concepts and information accumulated during the literature study are described in this chapter.

2.1 Compressor blade vibration

The mode shapes of a compressor blade are often classified as either bending, torsional, or edgewise (Cumpsty, 1989). These mode shapes are illustrated in figure 2.1. The bending modes are also sometimes referred to as flapping or flexural modes. Modes that are too intricate to fit into any of these categories are called complex or plate modes (Cumpsty, 1989). The vibration excitation system is designed to make each blade, in the first rotor blade row of the compressor, vibrate in its first bending mode.

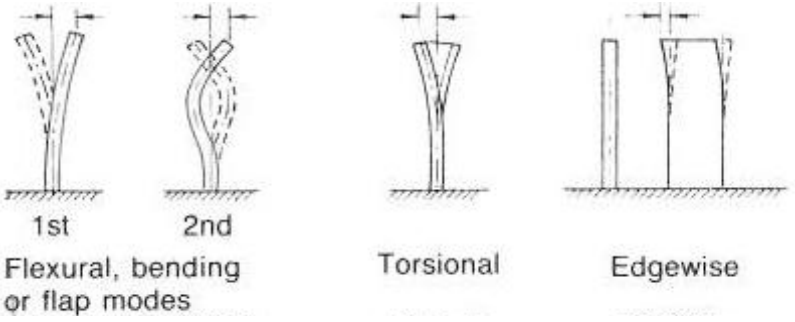

Figure 2.1: The mode shapes of a compressor blade (Armstrong and Stevenson, 1960).

An entire blade row also has mode shapes known as nodal diameter (ND) modes (Srinivasan, 1997). The 2 ND mode and the 0 ND mode of a blade row are illustrated in figure 2.2. A nodal diameter is a vibration node that lies along a

diametral line of the blade row (Cumpsty, 1989). A vibration node is a location at which the amplitude of vibration is always zero. The ND modes are named according to the number of nodal diameters present in the mode shape. As illustrated in figure 2.2a, the 2 ND mode therefore has two nodal diameters.

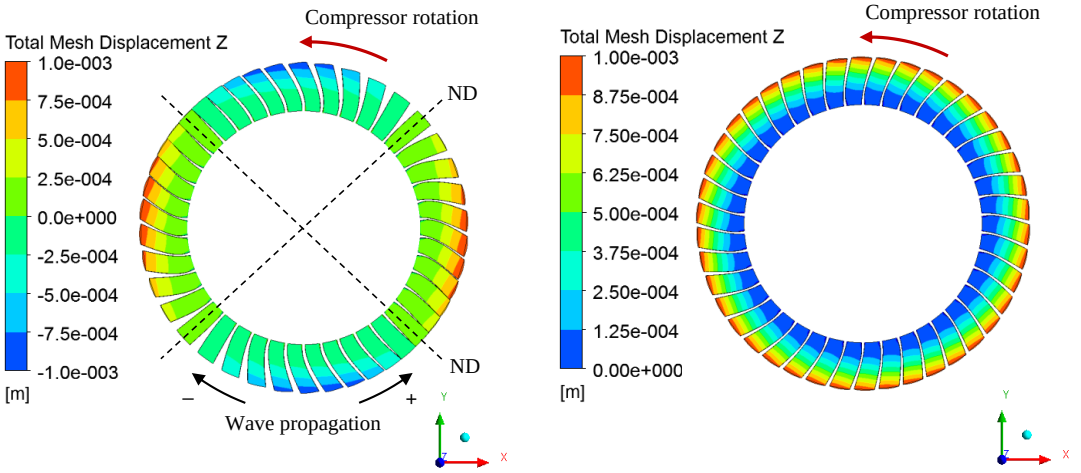

(a) The 2 ND mode (b) The 0 ND mode

Figure 2.2: The 2 ND mode and 0 ND mode of a blade row.

In a ND mode, the blades still vibrate in their individual bending, torsional, or edge-wise modes. The motions of all of the blades are identical except that the motion of each blade is out of phase with respect to the neighbouring blades (Srinivasan, 1997). The difference in phase between adjacent blades is expressed by equation (2.1.1) (Srinivasan, 1997). Note that equation (2.1.1) states that the difference in phase between adjacent blades when vibrating in the 0 ND mode is 0°. When vibrating in the 0 ND, the motions of all of the blades are therefore in phase. This is confirmed by figure 2.2b which shows that the 0 ND mode has no nodal diameters.

$$\Delta\phi_{\text{ab}} = \frac{360^\circ N_{\text{ND}}}{N_{\text{bl}}} \tag{2.1.1}$$

Depending on the frequency of vibration and the ND mode, either a standing wave or a travelling wave is formed along the circumference of the blade row (Srinivasan, 1997). If a travelling wave is formed, the travelling wave propagates along the circumference. As indicated in figure 2.2a, propagation of the wave in the same direction that the rotor rotates in is denoted by a positive sign (Srinivasan, 1997). The mode shape in figure therefore represents the +2 ND mode if the travelling wave is moving in the counter clockwise direction. A negative sign is used instead if the wave travels in the opposite direction to which rotor is rotating in (Srinivasan, 1997).

2.2 Multiple degree of freedom vibration

2.2.1 Equations of motion

The forced damped vibration of a n degree of freedom system, such as a structural FE model, is described by equation (2.2.1) (Cook, 1995). Also required are the initial conditions $\mathbf{d}_0$ and $\dot{\mathbf{d}}_0$. Equation (2.2.1) represents a set of n coupled linear ordinary differential equations (ODEs).

$$\mathbf{M}\ddot{\mathbf{d}} + \mathbf{C}\dot{\mathbf{d}} + \mathbf{K}\mathbf{d} = \mathbf{r} \tag{2.2.1}$$

According to Inman (2009), a common approach is to approximate the damping in the system as viscous damping. One method of achieving viscous damping is to use a damping model known as proportional damping or Rayleigh damping (Cook, 1995). The Rayleigh damping model assumes that $\mathbf{C}$ can be expressed according to equation (2.2.2)) (Cook, 1995). Rayleigh damping is the damping model supported by Ansys Mechanical for transient FE simulations (Ansys Mechanical Application User's Guide, 2012c).

$$\mathbf{C} = \alpha\mathbf{M} + \beta\mathbf{K} \tag{2.2.2}$$

2.2.2 Uncoupling the equations of motion

The mode shapes of the system $(\mathbf{u}_1, \mathbf{u}_2, \cdots, \mathbf{u}_n)$ can be used to uncouple the set of ODEs represented by equation (2.2.1). This is done by transforming $\mathbf{d}$ to the modal coordinate system $\mathbf{q}$. Before this can be done, the mode shapes $\mathbf{u}_i$ need to be scaled to form a new set of normalized mode shapes $\mathbf{v}_i$. The mode shapes are scaled so that they satisfy the condition expressed by equation (2.2.3) (Cook, 1995).

$$\mathbf{P}^{\mathrm{T}}\mathbf{M}\mathbf{P} = \mathbf{I} \tag{2.2.3}$$

The matrix $\mathbf{P}$ in equation (2.2.3) is given by

$$\mathbf{P} = \begin{bmatrix} \mathbf{v}_1, & \mathbf{v}_2, & \cdots, & \mathbf{v}_n \end{bmatrix} \tag{2.2.4}$$

The matrix $\mathbf{P}$ relates the coordinate system $\mathbf{d}$ to the modal coordinate system $\mathbf{q}$ as expressed by equation (2.2.5) (Cook, 1995).

$$\mathbf{d} = \mathbf{P}\mathbf{q} \tag{2.2.5}$$

Pre-multiplying equation (2.2.1) by $\mathbf{P}^{\mathrm{T}}$, substituting in equation (2.2.5) for $\mathbf{d}$, and simplifying yields equation (2.2.6) (Cook, 1995).

$$\ddot{\mathbf{q}} + \mathbf{\Gamma}\dot{\mathbf{q}} + \mathbf{\Omega}^2\mathbf{q} = \mathbf{P}^{\mathrm{T}}\mathbf{r} = \mathbf{l} \tag{2.2.6}$$

The matrix $\mathbf{\Omega}$ has the form

$$\mathbf{\Omega} = \begin{bmatrix} \omega_{\mathrm{n},1} & 0 & \cdots & 0 \\ 0 & \omega_{\mathrm{n},2} & \cdots & 0 \\ \vdots & \vdots & \ddots & \vdots \\ 0 & 0 & \cdots & \omega_{\mathrm{n},n} \end{bmatrix} \tag{2.2.7}$$

If the damping in the system is modelled as viscous damping, the matrix $\mathbf{\Gamma}$ has the form

$$\mathbf{\Gamma} = \begin{bmatrix} 2\zeta_1\omega_{\mathrm{n},1} & 0 & \cdots & 0 \\ 0 & 2\zeta_2\omega_{\mathrm{n},2} & \cdots & 0 \\ \vdots & \vdots & \ddots & \vdots \\ 0 & 0 & \cdots & 2\zeta_n\omega_{\mathrm{n},n} \end{bmatrix} \tag{2.2.8}$$

Equation (2.2.6) now represents a set of n uncoupled linear ODEs. The ith equation in this set is expressed by equation (2.2.9) (Cook, 1995). Equation (2.2.9) has the same form as the equation of motion for a single degree of freedom system. However, the single degree of freedom q_i now represents the contribution of an entire mode shape to the motion of the system.

$$\ddot{q}_i + 2\zeta_i\omega_{\mathrm{n},i}\dot{q}_i + \omega_{\mathrm{n},i}^2 q_i = l_i, \quad i = 0, 1, \ldots, n \tag{2.2.9}$$

If Rayleigh damping is used, the value of ζ_i is given by equation (2.2.10) (Inman, 2009).

$$\zeta_i = \frac{\alpha}{2\omega_{\mathrm{n},i}} + \frac{\beta\omega_{\mathrm{n},i}}{2} \tag{2.2.10}$$

2.2.3 Solutions to the equations of motion

If $\mathbf{r} = \hat{\mathbf{r}}\sin(\omega_{\mathrm{ef}}t)$ and $\zeta_i < 1$, the solution to equation (2.2.9) has the form expressed by equation (2.2.11) (Inman, 2009).

$$q_i = \underbrace{a_i e^{-\zeta_i\omega_{\mathrm{n},i}t}\sin(\omega_{\mathrm{d},i}t + \phi_{\mathrm{cq},i})}_{\text{complementary}} + \underbrace{\hat{q}_i\sin(\omega_{\mathrm{ef}}t + \phi_{\mathrm{pq},i})}_{\text{particular}} \tag{2.2.11}$$

The value of $\omega_{\mathrm{d},i}$ is given by

$$\omega_{\mathrm{d},i} = \omega_{\mathrm{n},i}\sqrt{1 - \zeta_i^2} \tag{2.2.12}$$

Equation (2.2.11) is the solution of a single degree of freedom system experiencing underdamped forced vibration (Inman, 2009). As indicated by equation (2.2.11), the solution is composed of two parts. The two parts are referred to as the complimentary solution and the particular solution. The damping in the system causes the complimentary solution to decay to zero as $t \to \infty$. However, the particular solution persists indefinitely after the complimentary part has vanished. The variable of a_i, in equation (2.2.12), is a constant that represents the amplitude of the complimentary solution.

The amplitude of the particular solution is related to the excitation force by equation (2.2.13) (Inman, 2009). The phase angle of the particular solution is given by equation (2.2.14) (Inman, 2009). According to equation (2.2.13), the value of $\hat{q}_i$ is inversely proportional to the term $(\omega_{\mathrm{n},i}^2 - \omega^2)$ if the damping in the system is small ($\zeta \approx 0$). In this case, the contribution of each mode to the vibration of the system therefore decreases as the difference between $\omega_{\mathrm{n},i}$ and ω increases.

$$\hat{q}_i = \frac{\hat{l}_i}{\sqrt{\left(\omega_{\mathrm{n},i}^2 - {\omega_{\mathrm{ef}}}^2\right)^2 + 2\zeta_i \omega_{\mathrm{n},i} {\omega_{\mathrm{ef}}}^2}} \tag{2.2.13}$$

$$\phi_{\mathrm{pq},i} = \arctan\left(\frac{2\zeta_i \omega_{\mathrm{n},i}\omega_{\mathrm{ef}}}{\omega_{\mathrm{n},i}^2 - \omega_{\mathrm{ef}}^2}\right) \tag{2.2.14}$$

Equation (2.2.11) can be converted back to the coordinate system $\mathbf{d}$ by applying the inverse of the transformation in equation (2.2.5). This results in equation (2.2.15) which is the solution to equation (2.2.1) (Inman, 2009). The variable b_i is a constant symbolizing the amplitude of each term in the complimentary solution.

$$\mathbf{d} = \underbrace{\sum_{i=1}^{n} b_i e^{-\zeta_i \omega_{\mathrm{n},i} t} \sin(\omega_{\mathrm{d},i} t + \phi_{\mathrm{c},i}) \mathbf{u}_i}_{\text{complementary}} + \mathbf{d}_{\mathrm{part}}(t) \tag{2.2.15}$$

2.3 Numerical integration schemes

Consider the generic set of transient linear ODEs expressed by equation (2.3.1). Equation (2.3.1) may represent, for example, the governing equations of fluid flow or structural deformation that have been discretised with respect to space only. In order to solve the system numerically for $\mathbf{x}$, equation (2.3.1) must be discretised and integrated with respect to time. The numerical time integration schemes used to solve equation (2.3.1) can be classified as either explicit or implicit.

$$\dot{\mathbf{x}} = \mathbf{g}(\mathbf{x}) \tag{2.3.1}$$

Equation (2.3.2) is an example of an explicit scheme. The superscript i denotes the value of $\mathbf{x}$ at the end of the ith integration time step. In an explicit scheme, the value of $\mathbf{x}^i$ is calculated using only the values of $\mathbf{x}$ from previous time steps (Zill and Cullen, 2006). This approach is expressed by equation (2.3.2) which states that the value of $\mathbf{x}^i$ only depends on $\mathbf{x}^{i-1}$. An advantage of the explicit scheme is therefore that the value of $\mathbf{x}^i$ can be directly determined from $\mathbf{x}^{i-1}$ without solving a system of linear equations (Zill and Cullen, 2006). However, the solution obtained using the explicit scheme is only stable when using a time step size smaller than a certain critical value (Zill and Cullen, 2006).

$$\dot{\mathbf{x}}^i = \mathbf{h}(\mathbf{x}^{i-1}) \tag{2.3.2}$$

An example of an implicit scheme is represented by equation (2.3.3). Unlike equation (2.3.2), the term $\mathbf{x}^i$ now appears on both sides of equation (2.3.3). This means that a set of linear equations must be solved at each time step in order to calculate the value of $\mathbf{x}^i$ (Zill and Cullen, 2006). However, implicit integration schemes have the advantage that the solution obtained is unconditionally stable irrespective of the integration time step size selected (Zill and Cullen, 2006).

$$\dot{\mathbf{x}}^i = \mathbf{h}(\mathbf{x}^i, \mathbf{x}^{i-1}) \tag{2.3.3}$$

2.4 Approaches to modelling FSI

Equations (2.4.1a) and (2.4.1b) represent a generic coupled system in which fluid-structure interaction occurs (Piperno and Farhat, 1997).

$$\dot{\mathbf{x}}_\mathrm{s} = \mathbf{g}_\mathrm{s}(\mathbf{x}_\mathrm{s}, \mathbf{x}_\mathrm{f}) \tag{2.4.1a}$$

$$\dot{\mathbf{x}}_\mathrm{f} = \mathbf{g}_\mathrm{f}(\mathbf{x}_\mathrm{f}, \mathbf{x}_\mathrm{s}) \tag{2.4.1b}$$

Equations (2.4.1a) and (2.4.1b) represent the development of the variables of the structural domain and fluid domain with time, respectively (Vaassen *et al.*, 2011). This division of the variables into two groups is referred to as a partitioning (Matthies and Steindorf, 2003).

The approaches used to solve equations (2.4.1a) and (2.4.1b) for $\mathbf{x}_\mathrm{s}$ and $\mathbf{x}_\mathrm{f}$, respectively, can be classified as either monolithic or staggered (Vaassen *et al.*, 2011). In the monolithic approach, equations (2.4.1a) and (2.4.1b) are treated as a single set that is solved using only a single solver (Vaassen *et al.*, 2011). In the staggered approach, equations (2.4.1a) and (2.4.1b) are each solved individually by two separate solvers that have been coupled together (Farhat *et al.*, 2006).

The CFD solver Ansys CFX and the structural FE solver Ansys Mechanical were already available at the start of the project. Using these solvers is advantageous as they can be coupled, using the multiphysics solver Ansys MFX, to form a staggered FSI model. This means that no additional coupling algorithm has to be written that handles the transfer of forces and displacements between the solvers. A staggered approach was therefore selected for the FSI simulations of the rotor blades and the vibration excitation system. A staggered approach has also previously been demonstrated as sufficient for simulating the vibration of turbomachinery blades. Im and Zha (2012) successfully used a staggered approach to simulate the vibration of blades in an axial flow compressor. A staggered approach was also utilised by Gnesin *et al.* (2000) to predict the motion of blades in an axial turbine.

The staggered approach used for the FSI simulations in chapter 6 is illustrated in figure 2.3. As shown in figure 2.3, the structural equations and the fluid equations are solved sequentially. This sequential solution of the structural and fluid equations may be repeated several times within each time step. These are referred to as stagger iterations (Ansys CFX Reference Guide, 2012*a*). During each time step, the aerodynamic loads acting on the structure, predicted by the CFD model, are applied to the FE model. The displacements of the structure, calculated by the FE model, are also transferred to the mesh of the CFD model. The system depicted in figure 2.3 is referred to as a two-way coupling as information is transferred in two directions between the structural domain and the fluid domain (Ansys CFX Reference Guide, 2012*a*).

The process illustrated in figure 2.3 can be expressed mathematically by equation (2.4.2a) and equation (2.4.2b) (modified from Vaassen *et al.* (2011)).

$$\dot{\mathbf{x}}_{\mathrm{s}}^{i,j} = \mathbf{h}_{\mathrm{s}}(\mathbf{x}_{\mathrm{s}}^{i,j}, \mathbf{x}_{\mathrm{s}}^{i-1}, \mathbf{x}_{\mathrm{f}}^{i,j-1}) \tag{2.4.2a}$$

$$\dot{\mathbf{x}}_{\mathrm{f}}^{i,j} = \mathbf{h}_{\mathrm{f}}(\mathbf{x}_{\mathrm{f}}^{i,j}, \mathbf{x}_{\mathrm{f}}^{i-1}, \mathbf{x}_{\mathrm{s}}^{i,j}) \tag{2.4.2b}$$

The superscripts i and j represent the value of $\mathbf{x}_{\mathrm{s}}$ and $\mathbf{x}_{\mathrm{f}}$ at the ith time step and the jth stagger iteration, respectively. If no stagger iterations are performed ($j_{\max} = 0$), equations (2.4.2a) and (2.4.2b) are reduced to equations (2.4.3a) and (2.4.3b). This is known as a weakly coupled staggered approach (Vaassen *et al.*, 2011).

$$\dot{\mathbf{x}}_{\mathrm{s}}^{i} = \mathbf{h}_{\mathrm{s}}(\mathbf{x}_{\mathrm{s}}^{i}, \mathbf{x}_{\mathrm{s}}^{i-1}, \mathbf{x}_{\mathrm{f}}^{i-1}) \tag{2.4.3a}$$

$$\dot{\mathbf{x}}_{\mathrm{f}}^{i} = \mathbf{h}_{\mathrm{f}}(\mathbf{x}_{\mathrm{f}}^{i}, \mathbf{x}_{\mathrm{f}}^{i-1}, \mathbf{x}_{\mathrm{s}}^{i}) \tag{2.4.3b}$$

Equations (2.4.3a) and (2.4.3b) behave like an explicit time integration scheme even if the individual solvers make use of implicit schemes (Vaassen *et al.*, 2011). This is because only the values of the fluid variables from time step $(i-1)$ are used to determine the values of the structural variables for time step i. However, the values of the fluid variables at time step i are calculated using the values of

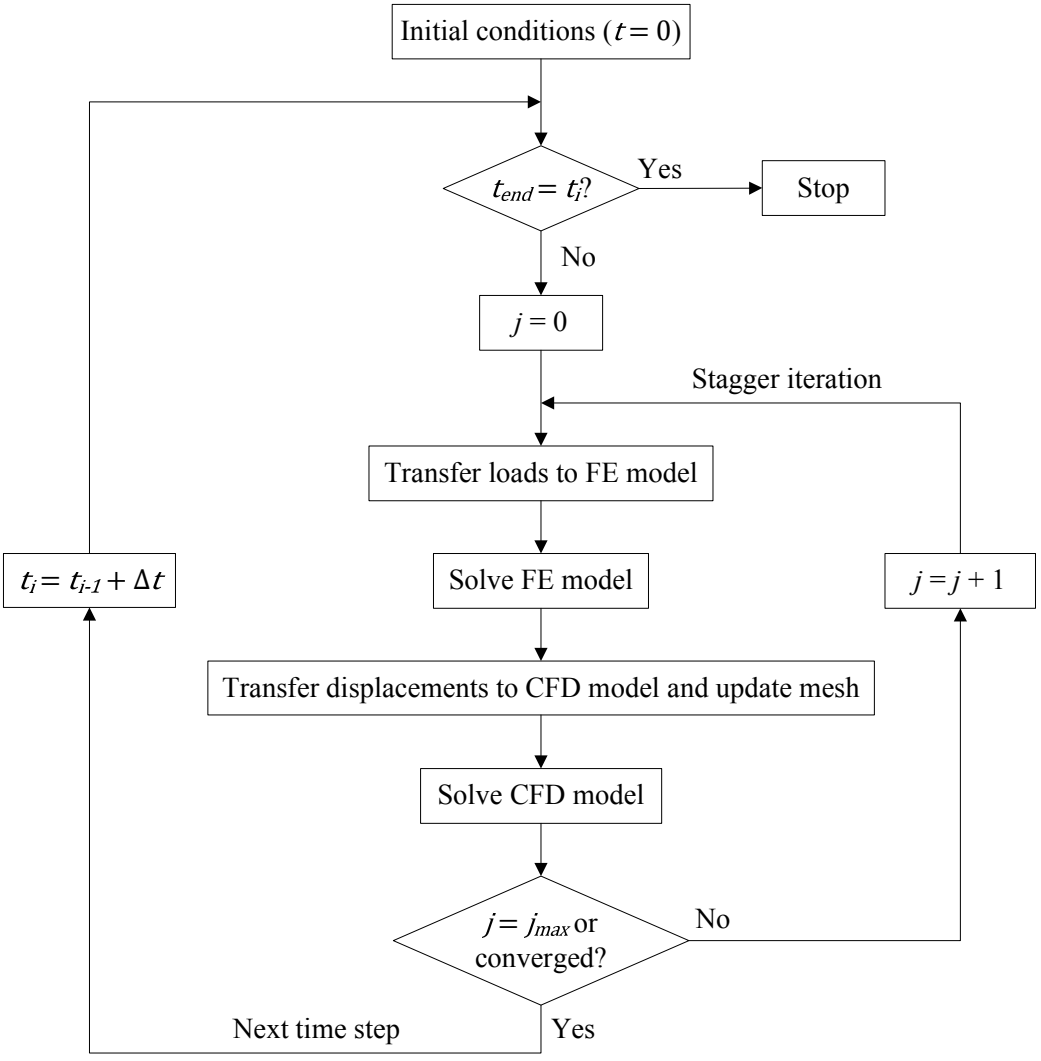

Figure 2.3: The staggered approach used for the FSI simulations (modified from Vaassen *et al.* (2011))

the structural variables from the same time step. There is therefore a lag between the solutions obtained for the domains of the fluid and the structure. This lag means that equations (2.4.3a) and (2.4.3b) cannot both be satisfied during the same time step (Vaassen *et al.*, 2011). The fact that the system of equations behaves like an explicit scheme also means that the solution to the system may be unstable for time step sizes that are too large (Matthies and Steindorf, 2003).

As already mentioned, stagger iterations involve solving equation (2.4.1a) and equation (2.4.1b) several times during the same time step. This is referred to as a strongly coupled staggered approach (Michler, 2005). The aim of this technique is to keep executing stagger iterations during the same time step until the values of $\mathbf{x}_s$ and $\mathbf{x}_f$ satisfy both equation (2.4.2a) and equation (2.4.2b) simultaneously (Vaassen *et al.*, 2011). Stagger iterations therefore reduce the lag

between the structural domain and the fluid domain, and improve the accuracy of the solution obtained (Storti *et al.*, 2006).

When stagger iterations are performed, the value of $\mathbf{x}_\mathrm{s}$ at time step i is no longer calculated using the value of $\mathbf{x}_\mathrm{f}$ at time step $(i-1)$ (refer to equation (2.4.2a)). Instead, the value of $\mathbf{x}_\mathrm{s}$ at time step i is now determined using the value of $\mathbf{x}_\mathrm{f}$ at the same time step and the previous stagger iteration. Equations (2.4.2a) and (2.4.2b) therefore now resemble an implicit time integration scheme (Vaassen *et al.*, 2011). This means that a strongly coupled staggered approach is less sensitive to the stability problems caused by large time step sizes (Storti *et al.*, 2006). A disadvantage of the strongly coupled staggered approach, when compared to the weakly coupled staggered approach, is that the stagger iterations significantly increase the computational costs incurred (Farhat *et al.*, 2006). It is also unclear whether using a strongly coupled approach with a greater number of stagger iterations is more accurate than simply using a weakly coupled approach with a smaller time step size (Farhat *et al.*, 2006).

Chapter 3

Experimental work

This chapter covers the experiments conducted to quantify the axial velocity perturbations induced by the vibration excitation system. This data was required for the boundary conditions of the FSI model. The experiments were performed on Stellenbosch University's Rofanco compressor test bench in collaboration with Van der Spuy, Raubenheimer, and Gill. The results of the experiments are therefore also presented in Van der Spuy *et al.* (2012). The chapter begins with a description of the Rofanco compressor, the vibration excitation system, and the measurement apparatus used. The procedure followed to collect the experimental measurements is then examined. The chapter concludes with an analysis of the results obtained.

3.1 The Rofanco compressor

The Rofanco compressor is a three stage axial flow compressor manufactured by Royston Fan Co. Ltd. A schematic of the Rofanco compressor is given in figure 3.1. The Rofanco compressor was designed to function at a rotation speed of 3000 rpm, and a mass flow rate of 2.66 kg/s. Operating under these settings, and an atmospheric temperature and pressure of 20 °C and 101.3 kPa, respectively, the compressor delivers a total-to-total pressure ratio of 1.022. The flow through the compressor is essentially incompressible over its entire operating map (Gill, 2012).

The Rofanco is driven by a 15 kW electric motor running off a three phase direct current (DC) supply (Raubenheimer, 2011). The electric motor is coupled directly to the rotor of the compressor. Air enters the compressor through the bell mouth inlet duct. The air then passes through a set of inlet guide vanes before entering the three stages. Each stage is made up of a rotor blade row followed by a stator blade row. Air leaves the compressor through the throttle valve. The throttle valve is used to control the mass flow rate through the compressor.

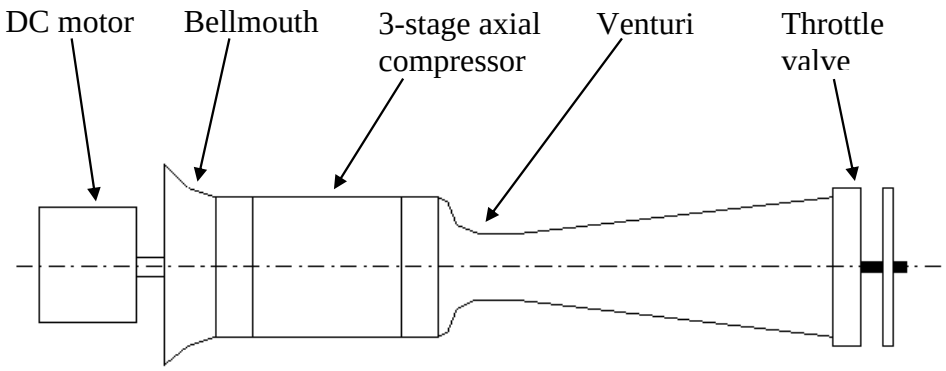

Figure 3.1: Schematic of the Rofanco compressor (Raubenheimer, 2011).

The geometry of each stage of the Rofanco compressor is identical for all three stages. Details of the geometry of each stage and the inlet guide vanes are now provided:

- Hub radius: 150 mm
- Shroud radius: 210 mm
- Inlet guide vanes: 36
- Rotor blades per stage: 43
- Stator blades per stage: 41

All of the blades and inlet guide vanes have a 10 % thick NACA65A profile with a chord of 30 mm. The FSI models in chapter 6 only contain the first rotor blade row of the compressor. Only the stagger and camber angles of the rotor blades are therefore provided in table 3.1. The average tip gap of the first rotor blade row was measured by Gill (2006) to be 0.31 mm.

Table 3.1: Rotor blade stagger and camber angles (Gill, 2012).

Radius (mm)	Stagger angle	Camber angle
150	38.00°	31.04°
165	45.00°	23.48°
180	49.40°	17.93°
195	53.00°	13.85°
210	56.10°	10.90°

There are mounting points for radial traverse brackets on the outside of the compressor casing. At these mounting points, there are also passages that allow access to the compressor flow path through the shroud wall. Using these passages, velocity and pressure probes can be inserted into the flow field upstream and

downstream of each blade row. The passages are filled in with stoppers when they are not in use.

3.2 The vibration excitation system

The vibration excitation system consists of 15 exciters which are mounted on the outside of the compressor casing. Photographs of the vibration excitation system, after being fitted to the Rofanco compressor, are shown in figure 3.2. The exciters are spaced evenly apart along the circumference of the casing. The vibration excitation system is designed to excite each blade in the first rotor blade row in the first bending mode and at the selected excitation frequency. At the same time, the system is designed to make the entire first rotor blade row vibrate, at the excitation frequency, in the selected ND mode.

An illustration of a single exciter is presented in figure 3.3a. It consists of a DC servo motor that has been fitted with a valve mechanism. Compressed air enters the main housing through the inlet port, and leaves the main housing through the nozzle. The exciter is connected to a control unit by cables that attach to the terminals. The control unit sets the rotation speed and angular position of the shaft of each servo motor. It also supplies each of the exciters with power.

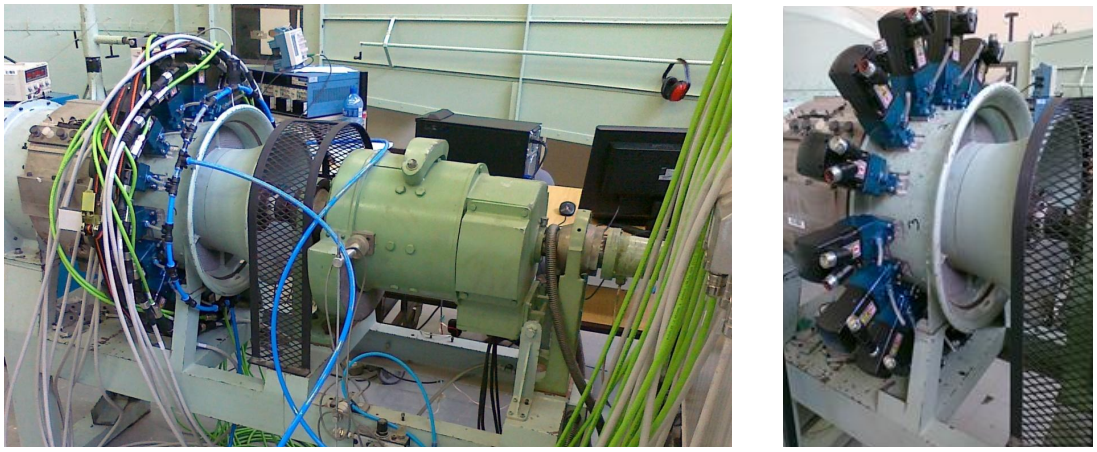

(a) The system fitted to the Rofanco compressor. (b) Close-up of exciters.

Figure 3.2: The vibration excitation system fitted to the Rofanco compressor (Van der Spuy *et al.*, 2012).

A cross section of the main housing of an exciter is shown in figure 3.3b. The valve mechanism is made up of a special rotor disk that is attached directly to the shaft of the servo motor. The rotor disk is enclosed in a chamber in the main housing. The exciter was designed to use two variants of rotor disk. Illustrations of each variant of rotor disk are provided in figure 3.4. The first variant had 16 holes with each hole having a diameter of 3.8 mm. The second variant had 32 holes with each hole having a diameter of 1.9 mm.

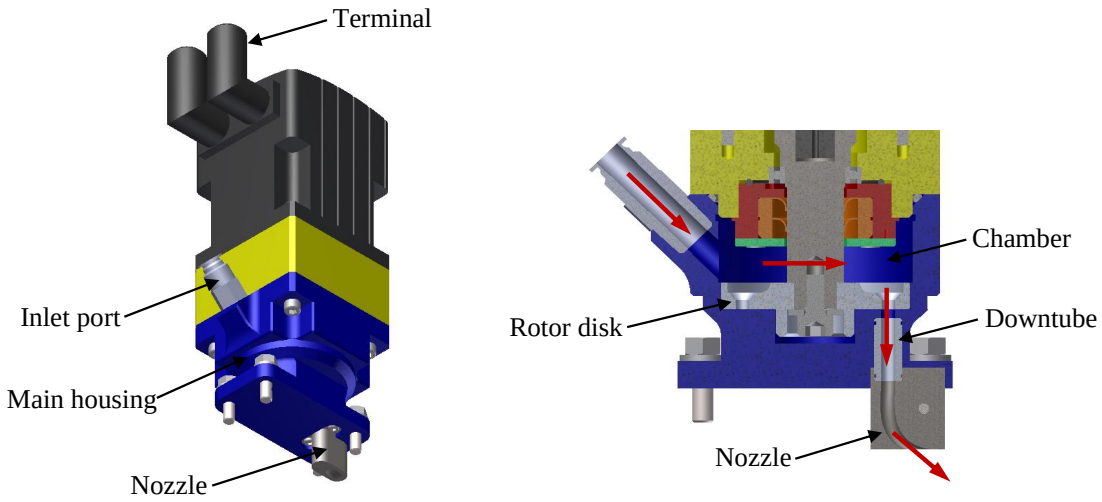

(a) A single exciter (b) Cross-section of the main housing

Figure 3.3: One of the exciters of the vibation excitation system (Wegman *et al.*, 2010).

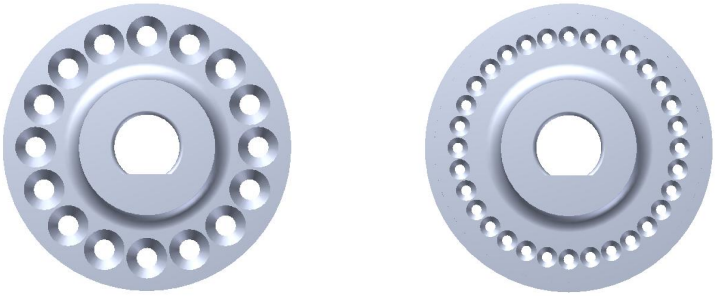

(a) 16 hole (b) 32 hole

Figure 3.4: The two types of rotor disks designed for each exciter (Wegman *et al.*, 2010).

As the shaft of the servo motor rotates, the holes in the rotor disk periodically line up with the hole in the chamber wall (see figure 3.3b). This causes the flow path between the chamber and the nozzle outlet to open and close repeatedly. The opening and shutting of the flow path creates a pulsating jet at the nozzle outlet. The pulsating jet, in turn, causes perturbations in the compressor velocity field. Since the flow path of the exciter nozzle is curved, the nozzle jet has velocity components in both the radial and axial directions. This type of nozzle was referred to by Raubenheimer (2011) as a production axial nozzle. When the exciter is mounted, the nozzle fits into a specially machined slot in the compressor casing so that the nozzle outlet is flush with the shroud wall. The slot is located upstream of the first rotor blade row of the compressor.

The pulsation frequency of the nozzle jet of each exciter is controlled by setting the rotation speed of the servo motor. Each nozzle jet can also be set to fire

in or out of phase with respect to the rest of the nozzle jets. This is done by offsetting the angular position of the rotor of each motor relative to the rotors of the adjacent motors. In order to make the blades vibrate in a specific ND mode, at specific excitation frequency, the pulsation frequency of each nozzle jet must be set according to equation (3.2.1a) (Van der Spuy *et al.*, 2012). The phase difference between adjacent nozzle jets must be set according to equation (3.2.1b) (Van der Spuy *et al.*, 2012).

$$f_{\mathrm{pu}} = f_{\mathrm{ef}} + N_{\mathrm{ND}} f_{\mathrm{rot}} \tag{3.2.1a}$$

$$\Delta\phi_{\mathrm{aj}} = \frac{360^{\circ} N_{\mathrm{ND}}}{N_{\mathrm{ex}}} \tag{3.2.1b}$$

The control unit of the vibration excitation system is connected to a PC. The operator uses the PC to select the desired excitation frequency, ND mode, and the pressure of the compressed air supplied to the exciters. The ND modes that are preprogrammed into the system are the 0 ND, +1 ND, +2 ND, +3 ND, -1 ND, -2 ND, and -3 ND patterns. The interface also allows the operator to specify custom vibration modes. The control unit automatically applies equations (3.2.1a) and (3.2.1b) once the excitation frequency and ND mode have been selected.

3.3 Measuring apparatus

3.3.1 Velocity measurements

Velocity measurements were taken using a hot wire x-probe. A photograph of the probe is shown in figure 3.5. The x-probe features two hot wires that are oriented in the shape of a cross. The convective cooling effect of the air flowing through the probe head induces a voltage across each wire. The voltage outputs from both wires are used to calculate the velocity of the air flowing through the probe head. Details about the calibration of the x-probe are available in Gill (2012). The calibration equations used to calculate the air velocity are only valid at the ambient temperature at which the x-probe was calibrated (Ball *et al.*, 1999). The voltages measured during the experiments therefore have to be corrected if the probe is operated at a temperature other than the calibration temperature. These corrections were implemented using equation (3.3.1) from Ball *et al.* (1999).

$$E^2_{\mathrm{corr}} = E^2_{\mathrm{m}} \frac{(T_{\mathrm{w}} - T_{\mathrm{cal}})}{(T_{\mathrm{w}} - T_{\mathrm{fl}})} \tag{3.3.1}$$

A schematic of the setup for the x-probe is provided in figure 3.6. The x-probe was mounted on a radial traverse. The output terminals of the x-probe were connected to an IFA-100 thermal anemometer. The IFA-100 thermal anemometer

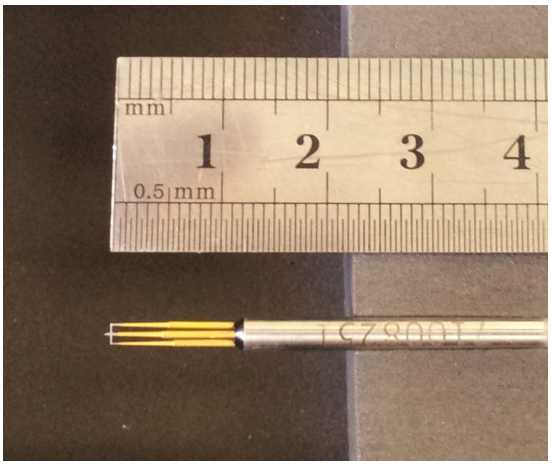

Figure 3.5: Photograph of the hot wire x-probe.

was, in turn, connected to a National Instruments NI UBS-6218 Multifunction signal hub. The signal hub itself was connected to a PC which was used to capture the velocity measurements.

The largest axial velocity perturbations should occur at the midplane of the nozzle jet. The preferred setup is therefore to have the x-probe positioned in line with the midplane of one of the exciter nozzles. This would allow the axial velocity perturbations to be detected as clearly as possible. However, when the exciters were fixed to their designated mounting points, none of the probe access ports lined up with the midplane of any of the exciter nozzles. The probe access port closest to midplane of an exciter nozzle outlet was therefore selected. This was the access port downstream of exciter 3. The angular offset of the velocity probe, relative to the midplane of the nozzle of exciter 3, is shown in figure 3.7a. The axial location of the velocity probe is presented in figure 3.7. The hot wire x-probe was inserted into the compressor 9.5 mm upstream of the first rotor blade row.

3.3.2 Other measurement apparatus

Blade 3 and blade 25, in the first rotor blade row of the Rofanco compressor, were each fitted with a pair of strain gauges by Raubenheimer (2011). The first strain gauge was attached to the pressure side of the blade. The second gauge was fixed to the suction side. The pair of strain gauges was connected in a half bridge configuration. Details of the strain gauges, including their locations on the blade surface, are provided in appendix A. The strain assemblies were not used during the measurement of the axial velocity profiles. However, strain data collected by Raubenheimer (2011) and Van der Spuy *et al.* (2012) was used to verify the FSI models in chapter 6. A brief discussion of the strain gauge assemblies is therefore still provided here. The data of Van der Spuy *et al.* (2012), used for the validation of the FSI models, is presented in appendix B.

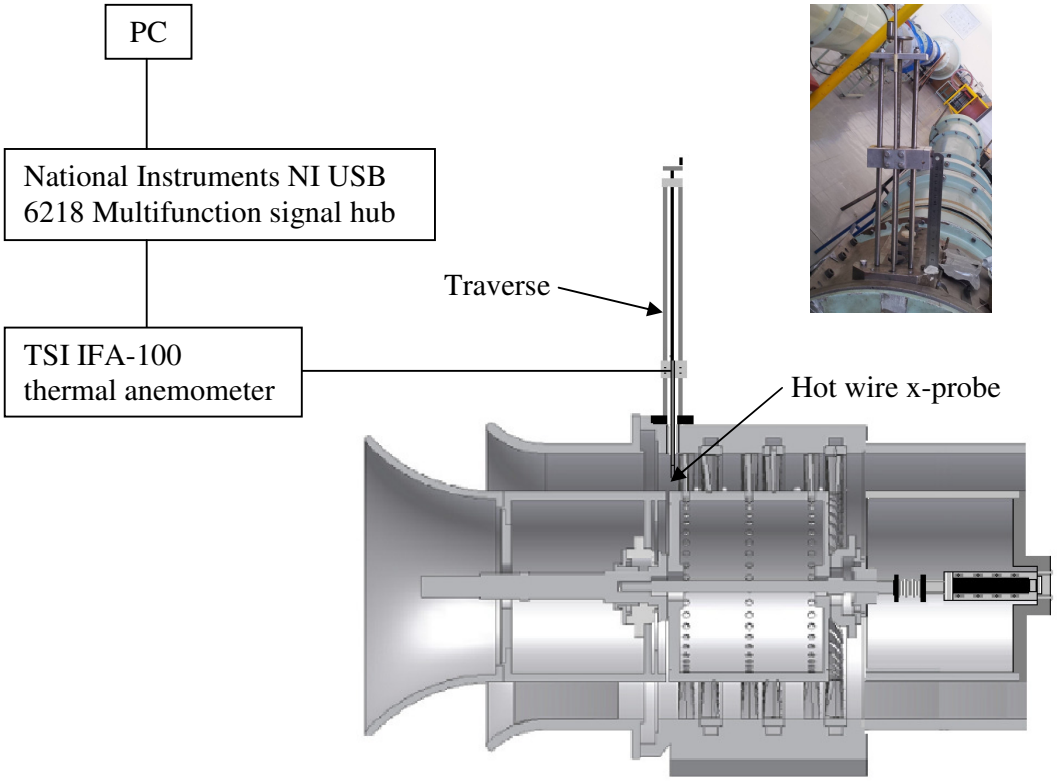

Figure 3.6: Experimental setup for the hot wire x-probe (modified from Raubenheimer (2011)).

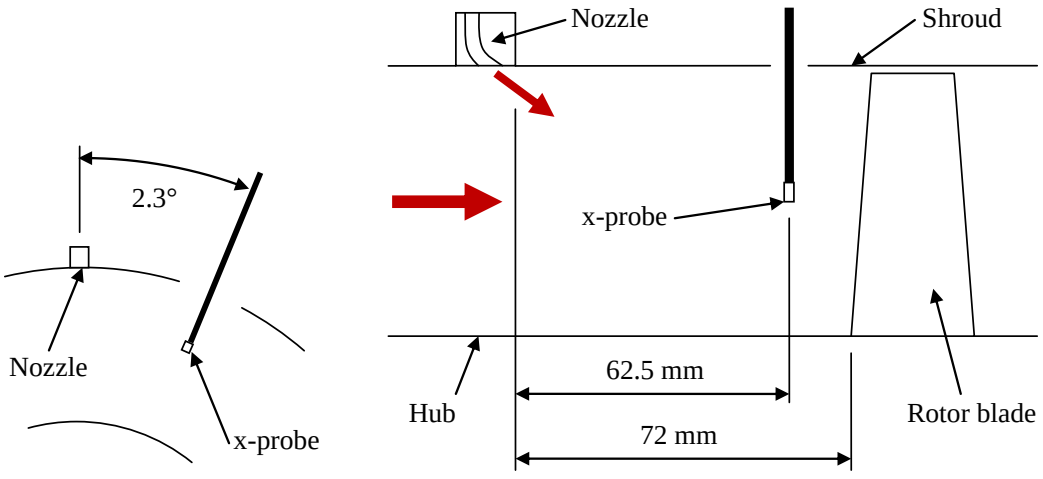

(a) Angular offset. (b) Axial position.

Figure 3.7: Position of the x-probe relative to the exciter nozzle and first rotor blade row.

During the calibration of the strain gauges, Raubenheimer (2011) applied a series of concentrated static tip loads to blade 3 and blade 25. The tip displacement perpendicular to the blade root, and the voltage output from the strain gauge assembly was recorded for each tip load. Raubenheimer (2011) used this data to derive equations (3.3.2a) and (3.3.2b). These equations estimate the tip displacement perpendicular to the root, from the voltage output of each strain gauge assembly, for blade 3 and blade 25, respectively. Further details about the calibration of the strain gauges are supplied in Raubenheimer (2011).

$$\delta_{\mathrm{b3}} = 0.1468 E_{\mathrm{br3}} \tag{3.3.2a}$$

$$\delta_{\mathrm{b25}} = 0.1871 E_{\mathrm{br25}} \tag{3.3.2b}$$

The half-bridge is only capable of providing the normal strain, detected by each strain gauge, due to bending (Figliola and Beasley, 2006). In the case of each rotor blade, the bending strain is in the direction parallel to the blade span. When a rotor blade is subjected to bending, the bending strains detected by each of the two gauges are equal in magnitude, but opposite in direction. The voltage output from each half-bridge assembly is related by equation (3.3.3) to the bending strain detected by the pressure side strain gauge (Figliola and Beasley, 2006).

$$\frac{E_{\mathrm{br}}}{E_{\mathrm{be}}} = \left(\frac{GF}{2}\right)\epsilon_b \tag{3.3.3}$$

The volume flow rate through the compressor was measured using a rotary vane anemometer. The anemometer is located in the venturi section of the compressor. Details of the calibration of the anemometer are available in Gill (2012).

3.4 Test procedure

The settings of the vibration excitation system for which the velocity profile was measured are summarised in table 3.2. The operating settings, of both the compressor and the vibration excitation system, were selected so that the velocity profiles complimented as much of the strain data of Van der Spuy *et al.* (2012) as possible. The majority of the strain data was collected at an excitation frequency near 650 Hz, or a range of excitation frequencies centered about 650 Hz. Raubenheimer (2011) measured the natural frequency of the first bending mode of blade 3 and of blade 25. The values obtained for the blades were 654 Hz and 649 Hz, respectively. An excitation frequency of 650 Hz is therefore close to both the natural frequency of blade 3 and the natural frequency of blade 25.

Each set of strain measurements taken by Van der Spuy *et al.* (2012) involved recording the vibration of the rotor blades for a number of different supply pressure settings of the vibration excitation system. One of the supply pressures

present in every set of strain measurements, collected at or near an excitation frequency of 650 Hz, was that of 2.5 bar. Most of the velocity profiles were therefore also measured with the system set to an excitation frequency of 650 Hz and a supply pressure of 2.5 bar. As shown in table 3.2, additional measurements were also taken at other combinations of excitation frequency and supply pressure. The additional measurements were performed in order to investigate the sensitivity of the axial velocity profiles to changes in excitation frequency and supply pressure.

Table 3.2: Test points at which the axial velocity profile was measured.

Excitation frequency	Supply pressure	Excitation mode
60 Hz	2.5 bar	0 ND
650 Hz	1.5 bar	0 ND
	2.5 bar	0 ND
		+1 ND
		+2 ND
		+3 ND
1200 Hz	2.5 bar	0 ND

The largest portion of the strain data of Van der Spuy *et al.* (2012) was collected at a rotation speed of 2880 rpm (48 Hz) and a mass flow rate of approximately 2.55 kg/s. The compressor was therefore set to the same rotation speed and mass flow rate for the measurement of the velocity profiles. The velocity at 11 radial stations was measured for each setting. The radial stations were spaced 5 mm apart from a radius of 155 mm to a radius of 205 mm. The velocity was sampled at each radial station for 1 second at a rate of 25 kHz.

The velocity profiles for the settings in table 3.2 were first measured with the vibration excitation system fitted with the 16 hole rotors. The measurements were then repeated with the system fitted with the 32 hole rotors. The velocity profile was also measured, during each set of tests, without the exciter system running. These velocity profiles were required for the boundary conditions of the FSI simulations and are provided in appendix C. They will be referred to as the undisturbed velocity profiles from this point onwards. The ambient temperature and atmospheric pressure, for the duration of the velocity profile measurements, were 25 °C and 97.7 kPa, respectively.

3.5 Results

3.5.1 Velocity profiles measured for the 32 hole rotors

The velocity profile, measured 9.5 mm upstream of the first rotor blade row, was found to be almost purely axial. The axial velocity profile in figure 3.8 was

measured with the vibration excitation system set to a frequency of 650 Hz, a supply pressure of 2.5 bar, and the 0 ND mode. The mean axial velocity is plotted relative to the undisturbed profile measured for the 32 hole rotors. The axial velocity perturbations in figure 3.8 represent the component of the axial velocity at 650 Hz. The 650 Hz component of the axial velocity at each radial station was extracted by performing a FFT of the velocity signal measured. The FFT also exhibited harmonics of the excitation frequency at 1300 Hz and 1950 Hz. These harmonics were also observed by Raubenheimer (2011) during the measurement of the velocity perturbations induced by the prototype excitation system. As mentioned in section 1.2, the FSI model needs to only be capable of simulating the component of the blade motion occurring at the excitation frequency. Only this component of the axial velocity perturbations was therefore focused on.

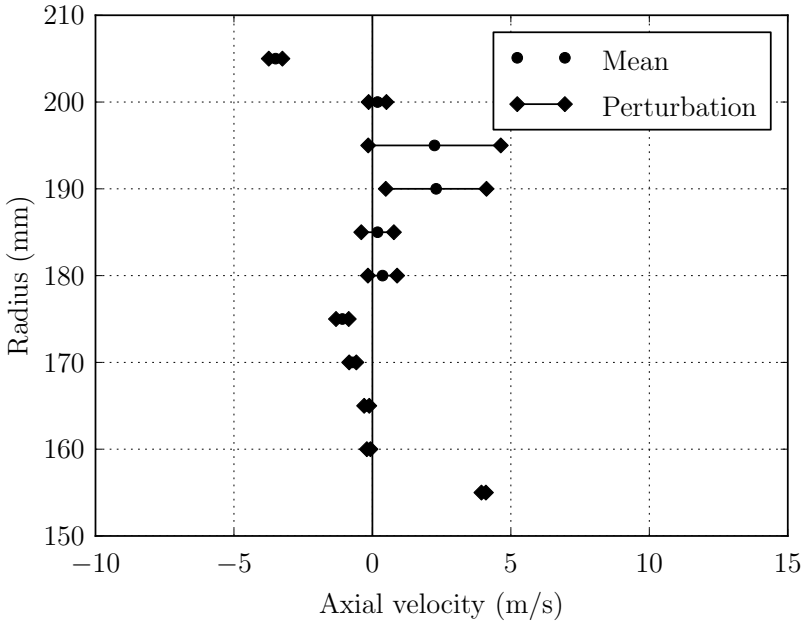

Figure 3.8: Axial velocity profile measured with the excitation system fitted with the 32 hole rotors, and set to the 0 ND mode, 650 Hz, and 2.5 bar.

The largest axial velocity perturbation in figure 3.8 is 4.8 m/s and occurs at a radius of 195 mm. The axial velocity perturbations are focused at approximately a third of the span from the blade tip. This was also the case for the velocity profiles measured for the +1 ND, +2 ND, and +3 ND modes. This suggests that the characteristics of each exciter nozzle jet remain similar regardless of the ND mode that the system is operating in. The velocity profiles also revealed that decreasing the excitation frequency from 650 Hz to 60 Hz increases the amplitude of the perturbations. Conversely, increasing the excitation frequency to 1200 Hz decreases the amplitude of the velocity perturbations. Decreasing the supply pressure also decreases the amplitude of the perturbations.

3.5.2 Velocity profiles measured for the 16 hole rotors

As was observed for the 32 hole rotors, the velocity profile measured 9.5 mm upstream of the first rotor blade row was almost entirely axial. Figure 3.9 shows the axial velocity profile measured with the vibration excitation system running at 650 Hz, 2.5 bar, and in the 0 ND mode. In this case, the mean axial velocity is plotted relative to the undisturbed velocity profile measured for the 16 hole rotors. As with the 32 hole rotors, the FFT of the axial velocity not only exhibited a component at 650 Hz, but also the harmonics of this component at 1300 Hz and 1950 Hz. The axial velocity perturbations in figure 3.9 are concentrated to the outer half of the spans of the blades. The maximum velocity perturbation of 5 m/s occurs at a radius of 190 mm. The profile in figure 3.9 also shows a sudden increase in axial velocity at a radius of 205 mm. A similar increase in axial velocity near the shroud was observed in the undisturbed velocity profile. As explained in appendix C, a possible cause for this is that the upstream exciter nozzle may have been protruding slightly into the compressor flow path.

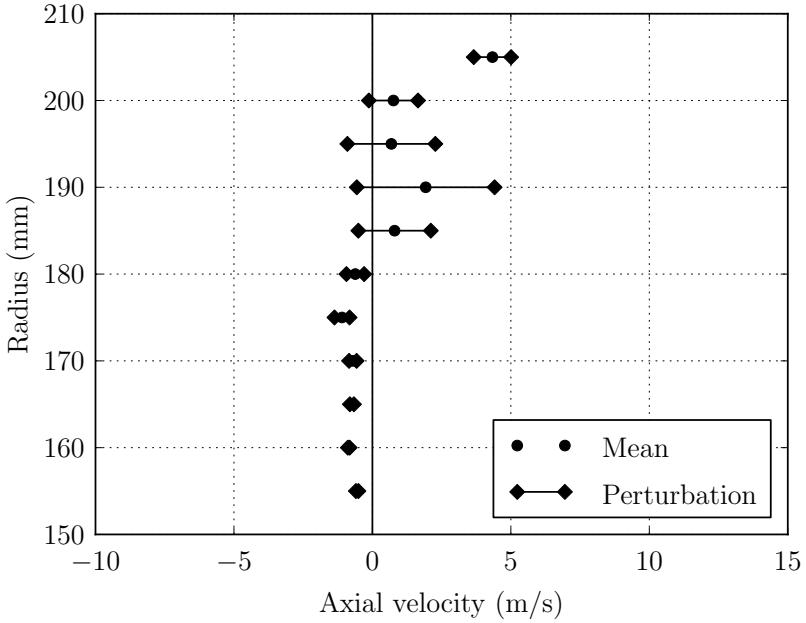

Figure 3.9: Axial velocity profile measured with the excitation system fitted with the 16 hole rotors, and set to the 0 ND mode, 650 Hz, and 2.5 bar.

The velocity profiles measured for the +1 ND, +2 ND, and +3 ND modes also showed velocity perturbations concentrated to the outer half of the spans of the blades. This again suggests that, as observed for the 32 hole rotors, the characteristics of the nozzle jets are not significantly affected by the selected ND mode. The velocity profiles also showed that reducing the excitation frequency from 650 Hz to 60 Hz does not have a large effect on the magnitude of the velocity perturbations. However, it does cause the velocity perturbations to become concentrated at a radius of 195 mm. Increasing the excitation frequency from 650 Hz

to 1200 Hz decreases the amplitude of axial velocity perturbations. Decreasing the supply pressure from 2.5 bar to 1.5 bar also decreased the amplitude of the velocity perturbations.

Chapter 4

FE analysis of the rotor blades

The creation of the FE model of the first rotor blade row is covered in this chapter. The chapter begins with a description of the geometry, material properties, mesh, and displacement boundary conditions of the FE model of a single rotor blade. The modal, static, and transient analyses, that were conducted to verify the FE model, are then discussed. Two versions of the FE model were constructed for the simulation of the 0 ND and +2 ND excitation modes of the vibration excitation system. The chapter ends with the creation of the 0 ND FE model and the +2 ND FE model.

4.1 Geometry and material properties

The hub of the compressor is a hollow cylinder with a wall thickness of 10 mm. Each rotor blade is connected to the hub by the threaded section at its root. The threaded section fits through a hole in the hub wall. The rotor blade is secured to the hub using a nut on the inside of the cylinder wall. The diameter of the threaded section is 24 mm. Each rotor blade is therefore free along the first and last 3 mm of its root chord. The hub of the compressor has a significantly higher stiffness than the rotor blades. The vibrations transmitted between neighbouring blades through the compressor hub were therefore assumed to be negligible when compared to the vibrations induced by the aerodynamic forces acting on the rotor blades. This meant that only a FE model of a single blade needed to be created. Multiple copies of this single blade FE model could then be combined to form a FE model containing the desired number of blades.

The rotor blades of the compressor are manufactured from aluminium alloy. The material of the blades was therefore modelled as linear isotropic. The material properties used for the FE model are summarised in table 4.1. As will be explained in section 4.3.1, these material properties were modified from those obtained for aluminium from Budynas *et al.* (2003).

Table 4.1: Material properties selected (modified from Budynas *et al.* (2003)).

Density	2712 kg/m^3
Young's modulus	71.1 GPa
Poisson's ratio	0.33

4.2 Mesh and constraint boundary conditions

The mesh of a single rotor blade was created using the solid shell 190 elements of Ansys Mechanical. The solid shell 190 elements are 8 node hexahedral elements that have been specifically designed for use in thin solid bodies (Ansys Mechanical APDL Element Reference, 2012*b*). The solid shell elements differ from regular hexahedral elements in that they use incompatible shape functions to overcome shear locking (Ansys Mechanical APDL Element Reference, 2012*b*). Shear locking is prevalent in regular hexahedral elements that are too thin. This causes regular hexahedral elements to be overly stiff when subjected to bending (Cook, 1995).

The solid shell mesher requires that the solid being meshed has two roughly parallel faces that are separated by its thickness. The leading and trailing edge radii of the blade were removed so that the pressure and suction sides formed these two distinct surfaces. This reduced the chord of the blade by less than 1 %. Since this was only a slight change to the blade geometry, the effect of this on the structural properties of the blade was assumed to be negligible. In each FSI model in chapter 6, the reduction in chord also caused a slight difference between the wetted surfaces in the CFD model and the wetted surfaces in the FE model. However, this discrepancy in the wetted surface was found to have a negligible effect on the interpolation of loads and displacements during the FSI simulations.

Coarse, medium, and fine versions of the single blade mesh were created so that a mesh refinement study could be performed. The details of the three meshes are provided in table 4.2. The meshes differed in the number of elements along the chord and span of the blade. Modal, static, and transient analyses were conducted using all three of the meshes. Details of the mesh refinement study are provided in appendix D.

Table 4.2: Details of the meshes for the single blade FE model.

	Elements	Nodes	Chord	Span
Coarse	300	676	12	25
Medium	1200	2550	24	50
Fine	5000	10302	50	100

The mesh refinement study revealed that the solutions obtained using each of the three meshes were all mesh independent. This was the case for the modal, static, and transient analyses. The transient analysis revealed that the computation

time required to solve the FE model, for any of the three meshes, was much less than the computation time required to solve the CFD model. The contribution of the FE model to the computation time of the FSI model should therefore be negligible, compared to that of the CFD model, irrespective of the mesh used. The fine mesh was therefore selected for the 0 ND FE model as it provided the highest resolution of the blade deformation and stress fields, and the aerodynamic forces acting on the wetted surface. This will be explained further in section 4.6. Only the results obtained using the fine mesh are therefore presented in the rest of this chapter.

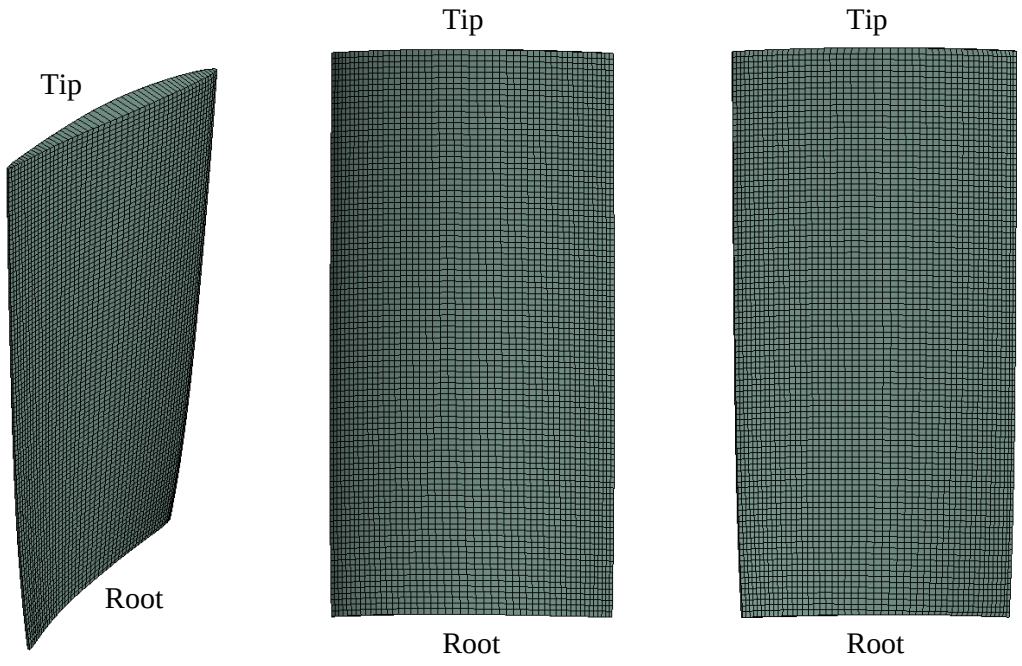

(a) Isometric view (b) Suction side (c) Pressure side

Figure 4.1: The fine mesh created for the single blade FE model.

The threaded connection between the blade and the hub acts like the fully fixed constraint of a cantilever beam. The fully fixed constraint was implemented by setting all three translational degrees of freedom of the nodes along the blade root equal to zero. Initially, the nodes along the first and last 3 mm of the root chord were left unconstrained to more accurately represent the connection between the blade and the hub. However, it was found that constraining the blade in this manner caused stability problems when running the FSI model. The FE model of the blade was therefore instead constrained along its entire root. It was found that constraining the FE model in this manner had a negligible effect on the results.

4.3 Verification of FE model

4.3.1 First bending mode

A modal analysis was conducted to verify that the FE model can accurately predict the natural frequency of the first bending mode of a rotor blade. The vibration excitation system is designed to make the blades vibrate in the first bending mode. This means that the first bending mode is likely to be the dominant mode present in the motion of each blade during the FSI simulations. It is therefore particularly important that the first bending mode be modelled accurately. No experimental data was available for the higher order modes of the blade. The FE modal was therefore also used to determine the mode shapes and natural frequencies of the next five modes after the first bending mode.

A Young's modulus of 71.7 GPa was initially used for the blade material instead of the value reported in table 4.2. This is the value of the Young's modulus quoted for aluminium alloy by Budynas *et al.* (2003). This yielded a natural frequency for the first bending mode of 651 Hz. This was only 0.5 % lower and 0.3 % higher than the natural frequencies measured by Raubenheimer (2011) for blade 3 and blade 25, respectively. The results therefore confirmed that the FE model is capable of accurately predicting the natural frequency of the first bending mode when using material properties that are typical for aluminium.

The Young's modulus from Budynas *et al.* (2003) is merely a typical value observed for aluminium. This means that the Young's modulus from Budynas *et al.* (2003) is not necessarily an exact representation of the stiffness of the material of each rotor blade. The Young's modulus was therefore decreased to 71.1 GPa so that the natural frequency of the first bending mode matched that of blade 25 more closely. A Young's modulus of 71.1 GPa is less than 1 % lower than the original value of 71.7 GPa. It is therefore also a plausible value for the Young's modulus of aluminium.

The natural frequencies obtained for the first six modes are summarised in table 4.3. The mode shapes of the first four modes are illustrated in figure 4.2. The contours shown are of the displacement perpendicular to the blade root. Each mode shape was scaled so that the maximum magnitude of the deflection perpendicular to the blade root was 1 m. The contour lines obtained for mode 1 are roughly parallel to the root of the blade. Mode 1 also only has a single vibration node at the blade root. This confirms that mode 1 is the first bending mode. The contour lines for mode 2 are roughly parallel to the span of the blade. In addition, mode 2 has a node along the centre of the chord of the blade. Mode 2 is therefore the first torsional mode of the blade.

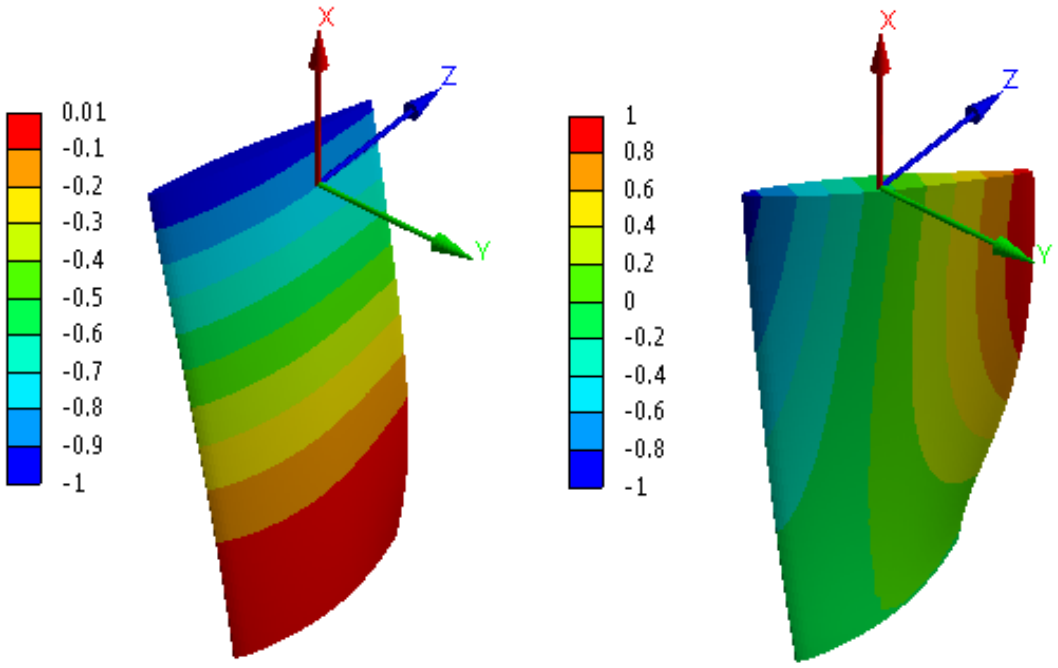

(a) Mode 1

(b) Mode 2

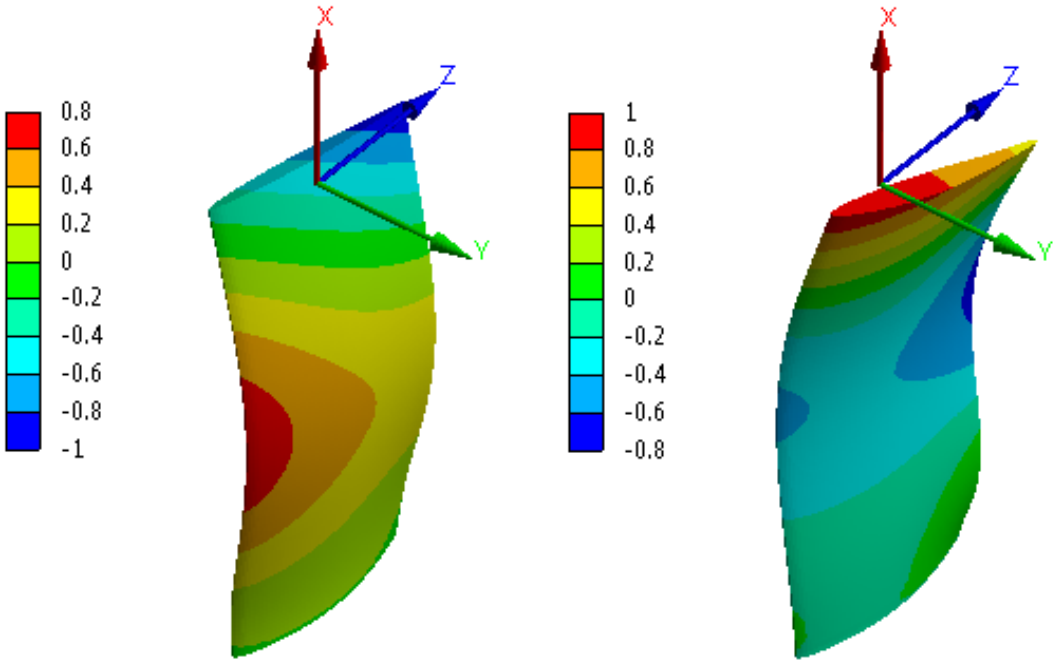

(c) Mode 3

(d) Mode 4

Figure 4.2: Mode shapes of the first four modes.

Table 4.3: Natural frequencies calculated for the first six modes.

Mode No.	Frequency (Hz)
1	649.35
2	2886.6
3	3512.1
4	5548.4
5	8597.5
6	10047

4.3.2 Static load case

A nonlinear static analysis was performed to confirm that the FE model responds in the same manner as an actual rotor blade when subjected to a specific load case. This was done by using the FE model to replicate the results of an experiment conducted by Raubenheimer (2011). The particular experiment simulated was already described in section 3.3.2. The experiment involved applying a concentrated tip load to the blade. The tip load was applied in the direction perpendicular to the blade root. The resulting tip deflection perpendicular to the blade root was then measured by Raubenheimer (2011). Raubenheimer (2011) also recorded the voltage output of the strain gauge assembly. This was done for several tip loads. The FE model was only used to recreate the version of the experiment conducted for blade 25.

The tip displacements measured by Raubenheimer (2011) are plotted in figure 4.3 as a function of tip load, together with the tip displacements predicted by the FE model. Also shown is the linear curve fitted by Raubenheimer (2011) to the measured tip displacements. The FE model predicts a similar linear relationship between the applied load and the tip displacement as that indicated by the curve fit. The gradient of the trend predicted by the FE model is 0.02462 mm/N. This is 9 % higher than the gradient of the linear curve fit.

The tip displacements perpendicular to the root calculated for the 7.747 N and 32.51 N loads are both within 9 % of the values measured by Raubenheimer (2011). The difference between the FE model and the experimental data is larger for the 11.65 N and 27.09 N loads. However, the tip displacement measured for these two load cases also deviate from the curve fit of Raubenheimer (2011). This suggests that the experimental values reported for these two load cases may be incorrect.

Equation (3.3.3) was used to calculate the bending strain, detected by the strain gauge on the pressure side of the blade, from the bridge voltages measured by Raubenheimer (2011). The bending strains obtained in this manner are plotted in figure 4.4 as a function of tip load. Also shown in figure 4.3 is the bending strain predicted by the FE model at the location corresponding to the centre of the pressure side gauge. The bending strain from the FE model agrees well with the experimental results for the 7.747 N and 32.51 N loads. As with the tip dis-

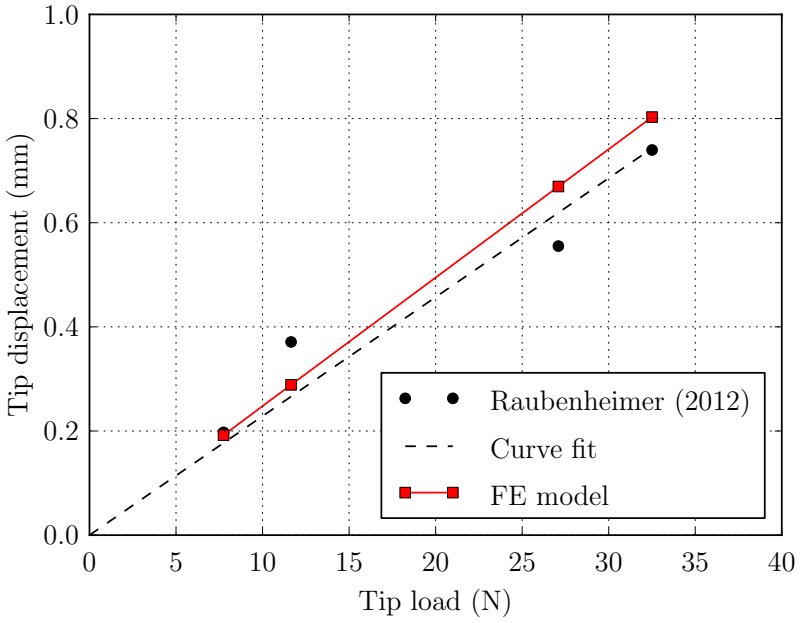

Figure 4.3: Tip displacement perpendicular to the root plotted as a function of tip load.

placements, the differences between the bending strain from the FE model and the measured bending strain are noticeably larger for the 11.65 N and 27.09 N load cases.

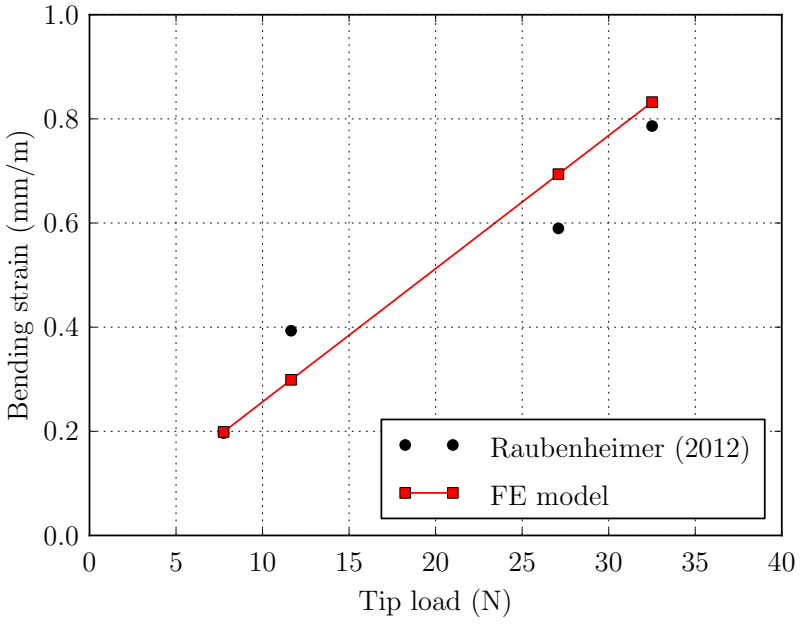

Figure 4.4: Bending strain plotted as a function of tip load.

4.4 Effect of centrifugal loads

The rotation of the rotor subjects each rotor blade to a centrifugal load. This centrifugal load creates a tensile stress state within each blade which increases its stiffness. This, in turn, causes the natural frequencies of the blade to increase. An FE analysis was conducted to investigate the effect of the centrifugal load on the natural frequency of the first bending mode.

A static analysis was first performed to determine the tensile stress field caused by the centrifugal load. A rotational velocity load, centered about the rotation axis of the rotor, was specified throughout the blade. The magnitude of the rotational velocity was set to 301.6 rad/s (2880 rpm). This is the same compressor rotation speed at which the velocity profiles in chapter 3 were measured. It is also the rotation speed at which the experiments of Van der Spuy *et al.* (2012) were performed.

Once the static analysis had been completed, a modal analysis was conducted. The solution to the static analysis was specified as the pre-stressed state for the modal analysis. The natural frequencies calculated during the pre-stressed modal analysis are summarised in table 4.4. Also shown are the original natural frequencies calculated in section 4.3.1 for the case of the blade being stationary.

Table 4.4: Natural frequencies calculated for the blade when stationary, and when rotating at 2880 rpm.

Mode No.	Frequency (Hz)	
	Stationary	2880 rpm
1	649.35	657.76
2	2886.6	2889.5
3	3512.1	3519.3
4	5548.4	5550.5
5	8597.5	8601.2
6	10047	10056

The results of FE model predict that the natural frequency of mode 1, which is the first bending mode, will increase from 649 Hz to 658 Hz due to the centrifugal load. The data of Van der Spuy *et al.* (2012) (refer to appendix B) shows the natural frequency of the first bending mode increases to approximately 653 Hz when the rotor is rotating. The FE model therefore predicts a larger increase in the stiffness of the blade than is indicated by the experimental data. However, the natural frequency of the first bending mode predicted by the FE model is only 0.8 % larger than that observed from the experimental data. The correlation between the FE model and the experimental data was therefore still deemed to be acceptable.

4.5 Sensitivity to time step size

In addition to the modal and static analyses in section 4.3, a transient analysis was also carried out using the FE model. The purpose of this analysis was to investigate the sensitivity of the FE model to changes in time step size. The FE model was used to simulate the situation where the blade tip is initially deflected in the direction perpendicular to the root. The tip is then released and the blade is allowed to vibrate freely without damping. The magnitude of the initial tip displacement perpendicular to the root was 0.5 mm.

The staggered approach selected for the FSI model requires that the same time step size be used by the CFD model and FE model. Raubenheimer (2011) showed that a time step of 5.5555×10^{-5} s was adequate for the CFD simulations of the prototype vibration excitation system. It therefore seemed logical to select a similar time step size for the simulations of the complete vibration excitation system. Ansys Mechanical makes use of an implicit time integration scheme (Ansys Mechanical APDL and Mechanical Appplications Theory Reference, 2012*a*). The solution of the transient FE model should therefore remain stable regardless of the time step size selected. However, the time step size chosen must still be small enough to adequately resolve the motion of the blade. The Ansys Mechanical Application User's Guide (2012*c*) suggests that the time step should be selected so that it satisfies the condition expressed by equation (4.5.1). The variable $f_{\max}$ is the frequency of the highest order mode present in the motion of the blade. Selecting the time step according to equation (4.5.1) guarantees that there are at least 20 time steps per period of the highest order mode.

$$\Delta t < \frac{1}{20 f_{max}} \tag{4.5.1}$$

The initial deflected shape of the blade resembles the first bending mode. The blade is therefore likely to vibrate almost entirely in the mode shape and at the natural frequency of the first bending mode. The natural frequency of the first bending mode is approximately 650 Hz. A time step size of 5.4945×10^{-5} s was therefore selected resulting in 28 time steps per period of vibration. The motion of the blade was simulated for 0.021678 s which corresponds to 400 time steps. The simulation was also repeated, for the same duration, using time steps of 1.0989×10^{-4} s and 2.74725×10^{-5} s. These time steps are double and half the duration of 5.4945×10^{-5} s, respectively.

The tip deflection perpendicular to the blade root is plotted as a function of time in figure 4.5. The amplitude of the tip displacement is 0.5 mm for all three time step sizes. The curves obtained for time steps of 2.74725×10^{-5} s and 5.4945×10^{-5} s are almost coincident for the entire duration of the simulation. This suggests that reducing the time step size beyond 5.4945×10^{-5} s has no significant effect on the solution obtained. The solution to the FE model is therefore independent of time step size when using time steps smaller than or equal to 5.4945×10^{-5} s. There is visible difference between the solution obtained

for a time step of 1.0989×10^{-4} s and the solutions obtained for time steps of 5.4945×10^{-5} s and 2.74725×10^{-5} s. As time increases, the curve obtained for a time step of 1.0989×10^{-4} s begins to lag behind the curves obtained for the other two time step sizes. This indicates that the frequency of vibration predicted is slightly lower when using a time step of 1.0989×10^{-4} s than when time steps of 5.4945×10^{-5} s or 2.74725×10^{-5} s are used. This observation is understandable as, unlike the time step sizes of 5.4945×10^{-5} s or 2.74725×10^{-5} s, a time step size of 1.0989×10^{-4} s violates equation (4.5.1).

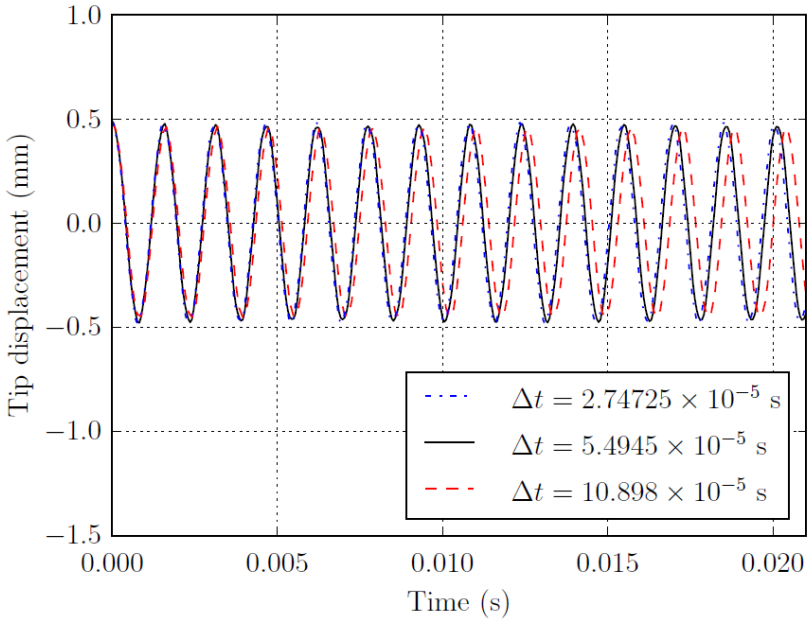

Figure 4.5: Tip displacement perpendicular to the root plotted as a function of time for each time step size.

4.6 Modifications to FE model for the FSI simulations

As will be discussed in chapter 5, a CFD model containing three rotor blades was created for the FSI simulations of the 0 ND mode. This CFD model is named the 0 ND CFD model in chapter 5. A corresponding FE model containing three blades was therefore created so that it could be coupled to the 0 ND CFD model. This FE model will be referred as the 0 ND FE model from this point onwards. The 0 ND FE model was created using three copies of the fine mesh of the single blade FE model. The resulting mesh is illustrated in figure 4.6a. The coupling of the 0 ND FE model and the 0 ND CFD model to form the 0 ND FSI model will be further discussed in chapter 6.

During the mesh refinement study in appendix D, the vibration of a single rotor blade was simulated using the coarse, medium, and fine meshes. The computation time in each case was approximately 0.5 s, 1.7 s, and 5.5 s per time step, respectively. Since the 0 ND FE model contains three blades, it was assumed that the computation time required to solve the 0 ND FE model would be roughly three times as long. The computation time required to solve the 0 ND FE model would therefore be 1.5 s, 5.1 s and 16.5 s per time step for the coarse, medium, and fine meshes, respectively. The computation time required to solve the 0 ND CFD model, during the transient CFD simulations in chapter 5, was approximately 500 s per time step. The contribution of the 0 ND FE model to the computation time of the 0 ND FSI model should therefore be negligible when compared to the contribution of 0 ND CFD model. This is the case regardless of whether the 0 ND FE model is constructed from the coarse, medium, or fine meshes. The fine mesh was therefore simply selected for the 0 ND FE model as it provided the highest resolution of the deformation of blade, and the aerodynamic loads acting on the blade surface.

A CFD model containing 21 blades was used for the simulation of the +2 ND mode. This CFD model is referred to in chapter 5 as the +2 ND CFD model. A corresponding FE model containing 21 blades was therefore created to be coupled with the +2 ND CFD model. This FE model will be referred to as the +2 ND FE model from this point onwards. The resulting FSI model is called the the +2 ND FSI model in chapter 6. Unlike the 0 ND FSI model, the contribution of the +2 ND FE model to the computation time of the +2 ND FSI model was no longer negligible when the +2 ND FE model was constructed using the fine mesh. Three copies of the medium mesh were therefore used to construct the +2 ND FE model instead. The mesh of +2 ND FE model is shown in figure 4.6b.

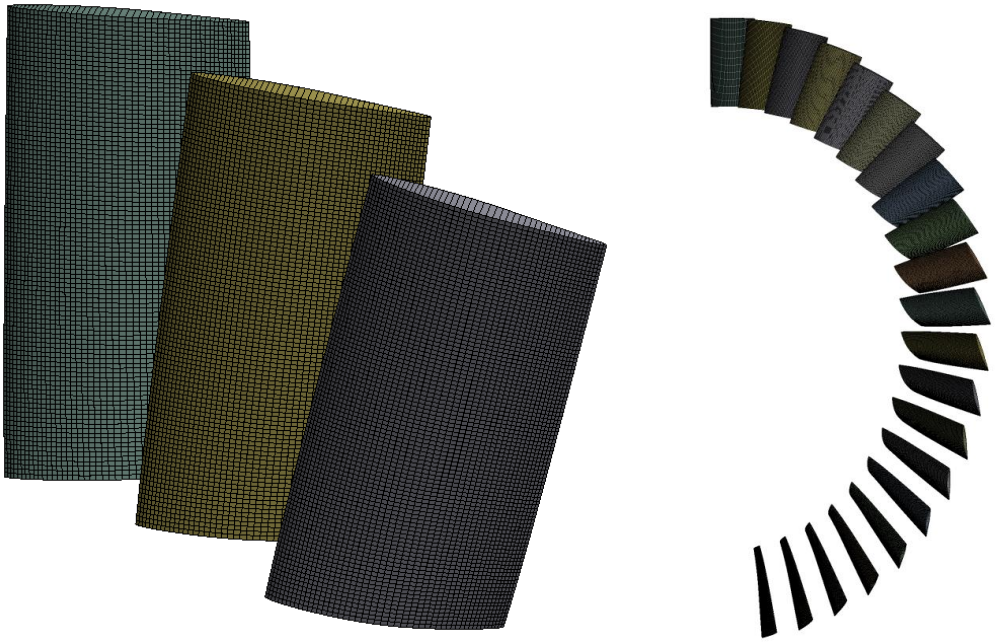

(a) The 0 ND FE model (b) The +2 ND FE model

Figure 4.6: Meshes of the FE models created of the first rotor blade row.

Chapter 5

CFD analysis of the rotor blades

This chapter covers the construction and verification of the CFD model of the rotor blade row and the vibration excitation system. Two different versions of the CFD model were created for the simulation of the 0 ND and +2 ND excitation modes. The two versions will respectively be referred to as the 0 ND CFD model and the +2 ND CFD model in this chapter and in the chapters that follow. The chapter begins by describing the computational domain, mesh, settings, and boundary conditions of the 0 ND CFD model. An overview is also given of the preliminary analyses performed to verify the 0 ND CFD model. This is followed by the derivation of the boundary conditions representing the exciter nozzle jets. The creation of the +2 ND CFD model from the 0 ND CFD model is then discussed. The chapter concludes with the transient CFD simulations, conducted using the 0 ND CFD model and the +2 ND CFD model, of the vibration excitation system and the first rotor blade row.

5.1 Computational domain and mesh

The staggered approach selected for the FSI simulations may require that the 0 ND CFD model be solved several times per time step. It is therefore desirable to keep the number of cells in the mesh of the 0 ND CFD model to a minimum in order to decrease the computation time required. As mentioned in section 1.1, Raubenheimer (2011) performed CFD simulations of a vibration excitation system consisting of 15 prototype exciters. When the vibration excitation system is operating in the 0 ND mode, the flow field downstream of each exciter is rotationally periodic. This allowed Raubenheimer (2011) to use periodic boundaries to reduce the size of the CFD model. Raubenheimer (2011) reduced the size of the CFD model so that it included only a single exciter, and three blades of the first rotor blade row.

Periodic boundaries require that the number of exciters and the number of rotor blades in the CFD model have the same periodicity. The complete vibration excitation system contains 15 exciters in total. If the CFD model is to include

only a single exciter, the number of blades in the CFD model therefore has to be selected so that it also has a periodicity of 15. However, this is not possible as the first rotor blade row has 43 blades which is a prime number. Raubenheimer (2011) solved this problem by setting up the CFD model as though the system consisted of only 14 exciters, and the first rotor blade row was made up of 42 blades. The single exciter and the three rotor blades in the CFD model therefore both had a periodicity of 14. Since this approach was already successfully utilised by Raubenheimer (2011), it was also employed for the 0 ND CFD model.

The computational domain used for the 0 ND CFD model is illustrated in figure 5.1. The blades in figure 5.1a have been labeled 1, 2, and 3. These numbers will be used to refer to individual blades in the CFD model from this point onward. The numbering scheme in figure 5.1a is independent of the numbers of the blades in the actual compressor. The axial dimensions shown in figure 5.1b are identical to those used by Raubenheimer (2011). The interface, that divides the domain into two blocks, is located 9.5 mm upstream of the rotor blade row. The interface is therefore positioned at the same axial location at which the velocity profiles in chapter 3 were measured.

The exciter nozzle jet was modelled by a square patch on the inlet boundary. A uniform velocity boundary condition was specified on the patch. The magnitude of the velocity at the patch boundary was specified to be a sinusoidal function of time. This same method was used by Raubenheimer (2011) to model the exciter nozzle jets of the prototype excitation system. The dimensions of the patch boundary in figure 5.1a are 6 mm $\times$ 6 mm. The dimensions of the patch were initially set to 4.5 mm $\times$ 4.5 mm which are similar to the patch dimensions used by Raubenheimer (2011). The dimensions were subsequently changed to 6 mm $\times$ 6 mm as the results obtained with this patch correlated better with the experimental velocity profiles in chapter 3.

Three meshes of varying densities were generated so that a mesh refinement study could be conducted. The meshes were created in Ansys Turbogrid. The three meshes will be referred to in this chapter as coarse, medium, and fine. The meshes differed in the amount of cells in the inlet and outlet regions, the tip gaps of the blades, the blade passages, and along the blade span. The meshes also differed in fineness near the hub, shroud, and blade surfaces. Details of each of the meshes are presented in table 5.1. A cross-section of the medium mesh is shown in figure 5.2. The cross-section was taken at a radius of 190 mm.

Table 5.1: Details of the coarse, medium, and fine meshes.

	Cells	Nodes	Number of cells			
			Inlet	Outlet	Tip gap	Blade span
Coarse	504918	532800	20	14	9	50
Medium	1299408	1376316	40	26	11	66
Fine	2654406	2737596	60	40	13	80

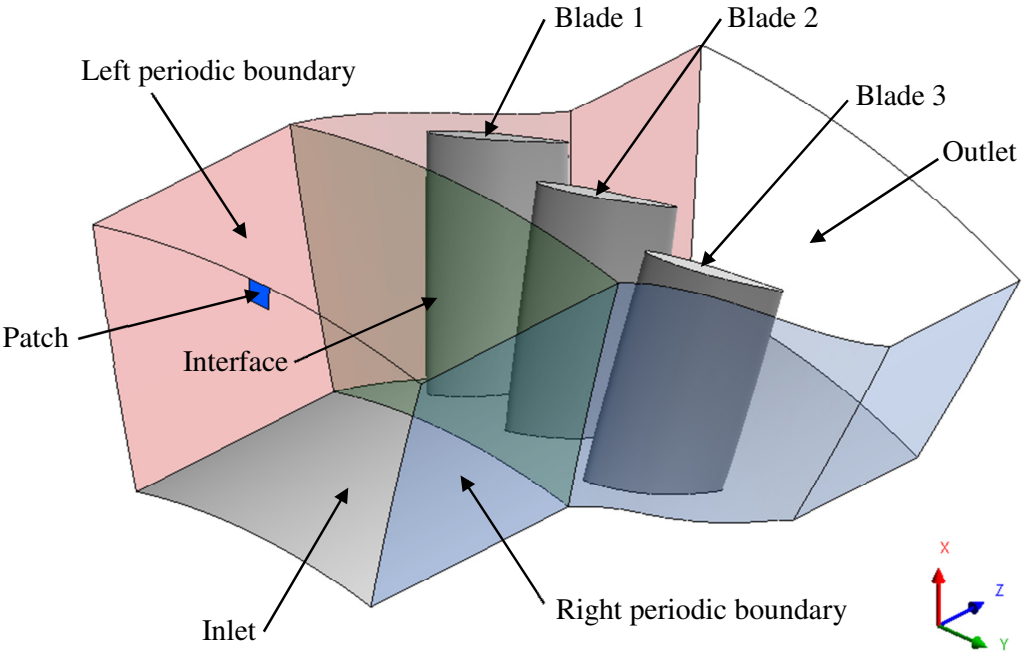

(a) Three dimensional view.

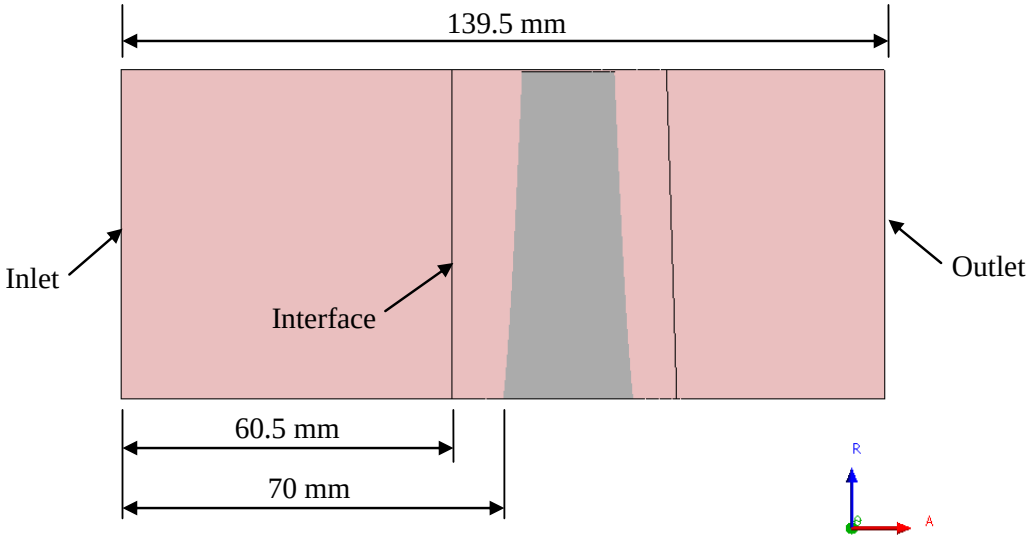

(b) Axial dimensions.

Figure 5.1: Computational domain of the 0 ND CFD model.

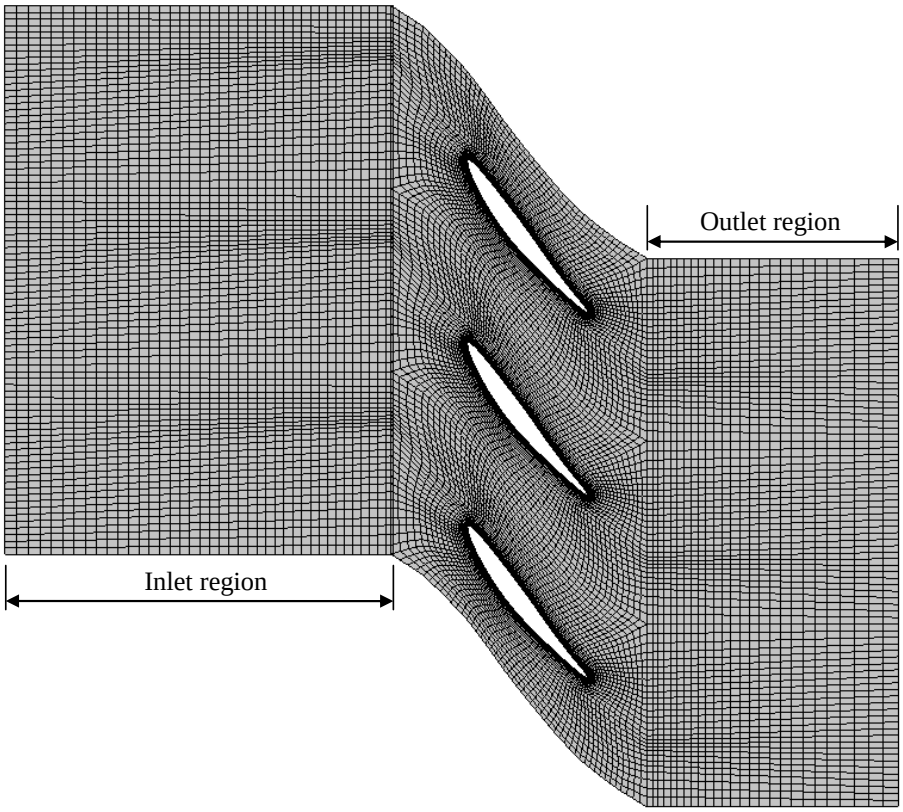

Figure 5.2: Section through the medium mesh at a radius of 190 mm.

The quality metrics displayed by the CFX solver for each of the meshes are provided in table 5.2. All of the cells in all three meshes have aspect ratios that fall within the good range defined by the CFX solver. The minimum orthogonality angle and the maximum expansion factor of each of the meshes are in the acceptable range specified by the CFX solver. However, the cells with expansion factors and orthogonality angles within the acceptable range made up less than 1 % of each of the meshes. The remaining 99 % of the cells of each mesh all had orthogonality angles and expansion factors that were in the good range.

Table 5.2: Quality metrics for each of the meshes.

	Required		Values obtained		
	Acceptable	Good	Coarse	Medium	Fine
Max aspect ratio	$< 100\ 000$	$< 10\ 000$	187	356	835
Min orthogonality	$> 20°$	$> 50°$	33.8°	33.3°	32.3°
Max mesh expansion	< 20	< 5	14	10	15

5.2 Settings and boundary conditions

This section describes the settings and boundary conditions selected for the 0 ND CFD model. These settings were used for all simulations performed using the 0 ND CFD model unless otherwise stated. The settings and boundary conditions were set up in Ansys CFX-Pre. The fluid properties of the air flowing through the domain was set to an ideal gas with its dynamic viscosity governed by Sutherland's law. The total energy equation was specified as the heat transfer model. The reference pressure for the domain was set to 98000 Pa which is a typical value for the atmospheric pressure in the laboratory where the Rofanco compressor test bench is located.

The Spalart-Almaras model, together with a low Reynolds number near wall treatment, was used by both Gill (2012) and Raubenheimer (2011) for their simulations of the Rofanco compressor. However, Ansys CFX 14.0 does not officially support the Spalart-Almaras model. The Ansys CFX Reference Guide (2012*a*) suggests that the $k-\omega$ SST model instead be used when simulating gas compressors. The $k-\omega$ SST model, together with an automatic near wall treatment, was therefore selected as the turbulence model. Depending on the y^+ value at the wall, the automatic wall treatment switches between a low Reynolds number near wall treatment and scalable wall functions.

The reference frame of the mesh block upstream of the interface was set as stationary. The reference frame of the downstream mesh blocks was specified as rotating at 2880 rpm. This is the compressor rotation speed at which the velocity profiles in chapter 3 were measured. It is also the rotation speed at which the strain data of Van der Spuy *et al.* (2012) was collected. The shroud boundary were set to a stationary adiabatic no slip wall boundary condition. A stationary adiabatic no slip wall was also specified for the hub boundary in the mesh block upstream of the interface. The hub in the downstream mesh block was set to an adiabatic no slip wall that is rotating at 2880 rpm.

A frame change model had to be specified at the interface in order to connect the stationary and rotating reference frames. The frame change model selected for the steady state simulations was the stage model. This model circumferentially averages the velocity of the fluid flowing through the interface. The transient rotor-stator model was specified as the frame change model for the transient simulations. In the transient rotor-stator model, data from the upstream side of the interface is interpolated directly on to the downstream side, and vice versa. No averaging of the fluid velocity therefore takes place.

A radial equilibrium boundary condition was specified at the outlet boundary of the domain. The relative static pressure at a radius of 180 mm was set to -676 Pa. This is the relative static pressure measured at a radius of 180 mm by Gill (2012) with the compressor set a mass flow rate of 2.51 kg/s and a rotation speed of 2900 rpm. A rotation speed of 2900 rpm and a mass flow rate of 2.51 kg/s are close to the rotation speed and mass flow rate at which the velocity profiles in chapter 3 were measured.

The axial velocity components at the inlet boundary were set equal to the appropriate undisturbed axial velocity profile in appendix C. The undisturbed profile selected depended on whether the scenario being simulated involved the vibration excitation system being fitted with the 32 hole rotors or the 16 hole rotors. The radial and tangential velocity components at the inlet boundary were set equal to zero. The total temperature at the inlet boundary was set to 298 K. The turbulence viscosity ratio and turbulence intensity at the inlet boundary were specified to be 100 and 10 %, respectively. These are the values suggested for the turbulence parameters in CFX-Pre for the case of highly turbulent flow. The experimental measurements of Gill (2012) revealed that the turbulence intensity throughout the majority of the flow field of the Rofanco compressor is between 10 % and 20 %. The turbulence parameters suggested for highly turbulent flow by CFX-Pre were therefore selected as the turbulence intensity corresponding to this setting was similar to the turbulence intensities measured by Gill (2012).

A steady state analysis was first conducted before each transient analysis. The purpose of the steady state analysis was to obtain a solution that could be used as the initial conditions of the transient analysis. Separate steady state solutions were calculated for the 32 hole rotors and the 16 hole rotors. For these steady state analyses, the axial velocity components on the patch boundary were set equal to the same undisturbed axial velocity profile used at the inlet boundary. The radial and tangential velocity components at the patch boundary were set equal to zero. Once the initial conditions had been obtained, the appropriate set of sinusoidal velocity components, representing each exciter nozzle jet, were assigned to the patch boundary for the transient analyses. The total temperature at the patch boundary was set to 298 K for both the transient and steady state analyses. The turbulence intensity and viscosity ratio were also respectively set to 10 % and 100 for both the steady state and transient analyses.

5.3 Verification of the 0 ND CFD model

Preliminary steady state and transient analyses were conducted to verify the accuracy of the 0 ND CFD model. The preliminary analyses were also used to determine the mesh density required to obtain a solution that is mesh independent.

5.3.1 Results of steady state analysis

The steady state analysis involved using the 0 ND CFD model to replicate the experiments performed by Gill (2012) on the Rofanco compressor test bench. The objective of the steady state analysis was to confirm that the 0 ND CFD model can accurately replicate the operation of the first rotor blade row before the additional complexity of the nozzle jets is introduced. The flow through the

first rotor blade row was simulated for a near design, higher than design, and stall mass flow rate. Only a summary of the results of the steady state analysis is provided here, but further details are available in appendix E.

The 0 ND CFD model was used to calculate the ratio between the static pressure downstream and upstream of the first rotor blade row. The static-to-static pressure ratio correlated sufficiently well with the measurements of Gill (2012) for the near design and higher than design mass flow rates. This was also true for the axial and tangential velocity profiles downstream of the rotor blade row. However, the static-to-static pressure ratio and the downstream velocity profile differed significantly from the experimental measurements of Gill (2012) for the stall flow rate. A possible explanation for this is that the compressor flow field is highly transient at this mass flow rate. It is therefore unlikely that accurate results could be obtained for the stall mass flow rate by conducting a steady state analysis. The overall agreement between the CFD model and the experiments of Gill (2012) was therefore still deemed to be acceptable. In addition, the pressure ratios and the velocity profiles obtained using the coarse, medium, and fine meshes were almost identical for each flow rate. All three meshes therefore produced steady state solutions that were mesh independent.

5.3.2 Results of transient analysis

Once the steady state analysis had been completed, the 0 ND CFD model was used to simulate a more complex transient case that included the exciter nozzle jets. The 0 ND CFD model was used to repeat transient simulations conducted by Raubenheimer (2011) of the prototype excitation system. As with the steady state analysis, only a short description of the results is given here. Further details about the transient analysis are available in appendix F.

The force acting on each blade, in the direction perpendicular to root, was calculated as a function of time for the coarse, medium, and fine meshes. The force perpendicular to the root predicted by the medium mesh and the force perpendicular to the root obtained using the fine mesh were found to be almost identical in the time domain. However, the amplitude obtained using the coarse mesh was found to be somewhat larger than that predicted using the medium and fine meshes. A FFT was calculated from the force perpendicular to the root acting on blade 2. As with the force perpendicular to the root in the time domain, the FFTs calculated for the medium and fine meshes were almost identical. The FFT computed for the coarse mesh showed larger values for the amplitudes of the prominent components than the FFT obtained using the medium mesh and the FFT obtained using the fine mesh.

The correlation between the magnitude of the FFT calculated for the coarse, medium and fine meshes and the results of Raubenheimer (2011) was deemed to be acceptable. The results also showed that the transient solutions obtained using the medium and fine meshes are mesh independent. However, the solution

obtained using the coarse mesh was not completely mesh independent. This conclusion is different from that reached in section 5.3.1 where the steady state solutions obtained using each of the three meshes were all the same. The medium mesh was therefore the mesh with the least number of cells that provided both steady state and transient solutions that were mesh independent. The medium mesh was therefore selected for the 0 ND CFD model.

5.4 Derivation of nozzle boundary conditions

This section discusses the derivation of the sinusoidal velocity components for the patch boundary. The sinusoidal velocity components were used to represent the nozzle jets of the complete vibration excitation system. The velocity components were derived for the scenario where the system is operating at an excitation frequency of 650 Hz, a supply pressure of 2.5 bar, and in the 0 ND mode. This is the excitation frequency and supply pressure at which the majority of the axial velocity profiles presented in chapter 3 were measured. The experimental profiles revealed that the amplitude of the velocity perturbations induced depend on whether the system is fitted with either the 32 hole rotors or the 16 hole rotors. Separate sets of velocity components were therefore derived for each variant of rotor disk.

5.4.1 Procedure for deriving the velocity components

A method was devised for estimating the force acting on each blade, in the direction perpendicular to the root, at the excitation frequency. The method estimates the component at the excitation frequency from the strain data of Van der Spuy *et al.* (2012). The data of Van der Spuy *et al.* (2012) was collected with the vibration excitation system set to an excitation frequency of 660 Hz, a supply pressure of 2.5 bar, and the 0 ND mode. The axial velocity profiles were measured with the system set to the same supply pressure and ND mode, but an excitation frequency that is 10 Hz lower (650 Hz). However, it was assumed that the difference in excitation frequency was small enough that the estimated amplitude of the component at 660 Hz was also valid for an excitation frequency of 650 Hz. Further details regarding the derivation of the method, and how it was used to estimate the blade force are provided in appendix G.

The procedure used for the derivation of each set of velocity components was as follows:

1. Apply a candidate set of axial and radial velocity components to the patch boundary. Set the tangential velocity components at the patch boundary equal to zero.

2. Perform a transient analysis.

3. Compare the axial velocity profile computed using the 0 ND CFD model, at 9.5 mm upstream of the first rotor blade row, to the appropriate axial velocity profile measured for the 0 ND mode.

4. Compare the component of the force perpendicular to the root, existing at the excitation frequency, to the estimated value in appendix G.

The procedure was repeated for different combinations of velocity components and patch boundary dimensions. This was done until the best correlation was achieved between the computed and measured axial velocity profiles, and the computed and estimated amplitude of the component of the blade force at the excitation frequency. The axial velocity profile from the 0 ND CFD model was compared to the profile in figure 3.8 for the derivation of the velocity components for the 32 hole rotors. The profile from the 0 ND CFD model was compared to figure 3.9 instead for the derivation of the velocity components for the 16 hole rotors.

The time step size selected for each transient analysis was 5.4945×10^{-5} s. The number of iterations per time step was set equal to 5 iterations. The motivations for selecting this time step size and number of sub iterations will be explained in section 5.5 and section 5.6, respectively. Each transient analysis was run for a duration of 200 time steps which is equivalent to approximately half of a rotation of the compressor rotor. Once it appeared that the appropriate set of velocity components had been identified, the duration of the simulation was extended by a further 3600 time steps. The total duration of the simulation was therefore 3800 time steps which corresponds to approximately 10 rotations of the rotor. The duration of the simulation was extended to better resolve the components in the frequency domain that make up the axial velocity and the blade force.

5.4.2 Results

It was found that the best correlation, between the axial velocity profile computed by the 0 ND CFD model and the corresponding profile measured for the 0 ND mode, was obtained when using a 6 mm $\times$ 6 mm patch. A 6 mm $\times$ 6 mm patch also yielded an amplitude for the component of the force perpendicular to the root, occuring at the excitation frequency, for each blade that fell within the range of values estimated in appendix G. The velocity components, selected to represent the nozzle jets produced by the 32 hole rotors, are expressed by equations (5.4.1a) and (5.4.1b). Equations (5.4.2a) and (5.4.2b) express the velocity components selected to represent the nozzle jets generated by the 16 hole rotors.

$$V_r = -55.82 - 19.94\sin(2\pi 650t) \tag{5.4.1a}$$

$$V_z = 128.4 + 45.85\sin(2\pi 650t) \tag{5.4.1b}$$

$$V_r = -59.17 - 29.58\sin(2\pi 650t) \tag{5.4.2a}$$

$$V_z = 126.9 + 63.44\sin(2\pi 650t) \tag{5.4.2b}$$

As stated in section 5.4.1, the 0 ND CFD model was used to calculate the axial velocity profile 9.5 mm upstream of the first rotor blade row. The mean axial velocity and the axial velocity perturbations, computed using the 0 ND CFD model for the 32 hole rotors, are plotted as a function of radius in figure 5.3 and figure 5.4, respectively. The axial velocity perturbations in figure 5.4 represent the component of the axial velocity occurring at a frequency of 650 Hz. This component was extracted by computing a FFT of the axial velocity predicted at each radius by the 0 ND CFD model. Also plotted in figure 5.3 is the mean axial velocity from the profile in figure 3.8. The axial velocity perturbations from figure 3.8 are plotted in figure 5.4.

The axial velocity perturbations from the experimental data, plotted in figure 5.4, are concentrated to the other third of the span of each blade. Figure 5.4 shows that, when equations (5.4.1a) and (5.4.1b) are applied to the patch boundary, the 0 ND CFD model also predicts that the axial velocity perturbations are concentrated to the outer third of the blade span. The root mean square (RMS) of the difference between the profiles of mean axial velocity in figure 5.3 is 2.07 m/s. The RMS of the difference between the profiles of axial velocity perturbation in figure 5.4 is 0.402 m/s.

The mean axial velocity, calculated by the 0 ND CFD model for the 16 hole rotors, is plotted as a function of radius in figure 5.5. The axial velocity perturbations occurring at 650 Hz, obtained using the 0 ND CFD model for the 16 hole rotors, are plotted in figure 5.6. Also plotted in figure 5.5 and figure 5.6 are the mean axial velocity and the axial velocity perturbations from figure 3.9, respectively. The profile in figure 5.6 shows that the largest axial velocity perturbations occur along the outer half of the span of each blade. This was also the case for the experimental axial velocity profile in figure 3.9. The RMS of the difference between the profiles of mean axial velocity in figure 5.5 is 3.17 m/s. The RMS of the difference between the profiles of axial velocity perturbation in figure 5.6 is 0.498 m/s.

Each nozzle jet predicted by the 0 ND CFD model, for either the 32 hole rotors or the 16 hole rotors, is only wide enough to strike one rotor blade at a time. This causes some of the rotor blades to be hit by several consecutive pulses of each nozzle jet. Other rotor blades are completely missed by nozzle jets for several consecutive pulses. As a result, the force acting on the blades in the 0 ND CFD model are all different during the early stages of the simulation. However, as the duration of the simulation is extended, all of the blades should eventually get a turn to be positioned downstream of one of the nozzle jets. All of the rotor blades will therefore be impacted by the pulsating nozzle jets an approximately equal number of times after a sufficient amount of time has lapsed. The magnitudes of the forces acting on each of the blades in the 0 ND CFD model should therefore become increasingly similar as the duration of the simulation is increased.

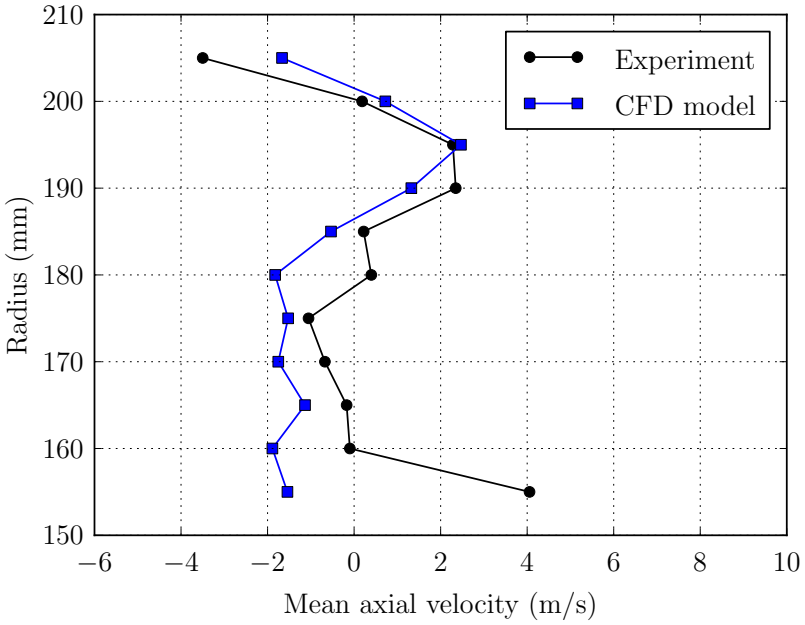

Figure 5.3: Mean axial velocity computed by the 0 ND CFD model for the 32 hole rotors and an excitation frequency of 650 Hz.

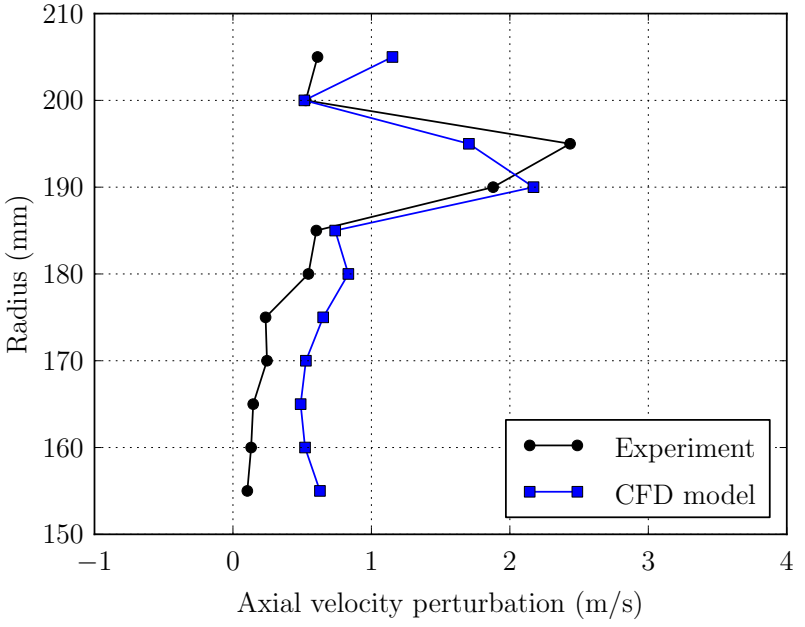

Figure 5.4: Axial velocity perturbations computed by the 0 ND CFD model for the 32 hole rotors and an excitation frequency of 650 Hz.

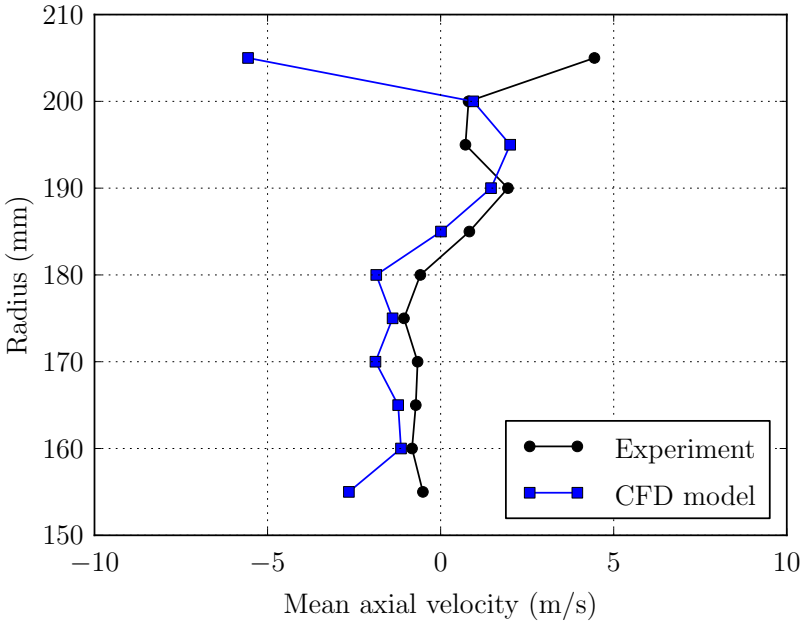

Figure 5.5: Mean axial velocity computed by the 0 ND CFD model for the 16 hole rotors and an excitation frequency of 650 Hz.

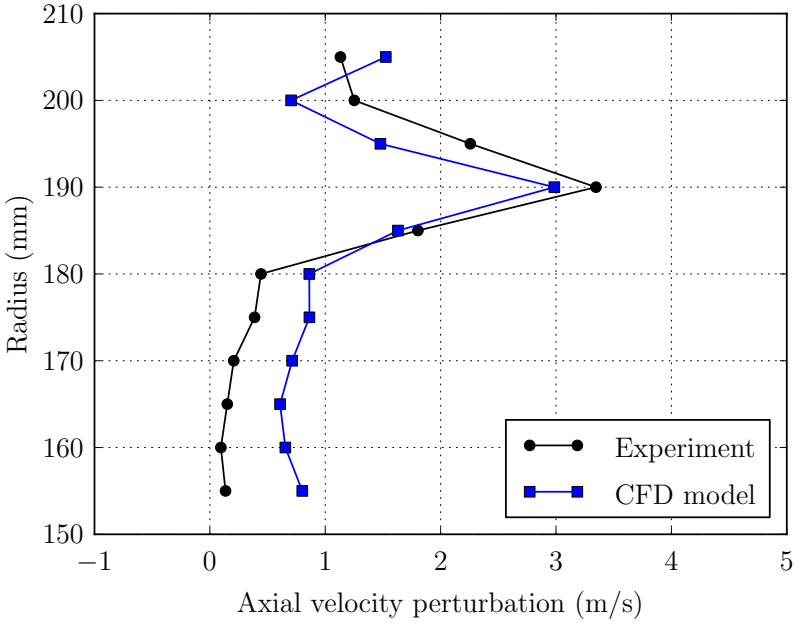

Figure 5.6: Axial velocity perturbations computed by the 0 ND CFD model for the 16 hole rotors and an excitation frequency of 650 Hz.

A FFT was calculated from the force perpendicular to the root acting on each blade in the 0 ND CFD model. This was done for both the blade forces predicted for the 32 hole rotors and the blade forces predicted for the 16 hole rotors. The FFTs confirmed that the magnitudes of the forces acting on the blades indeed become similar as the duration of the simulation is extended. Table 5.3 contains the magnitude of the 650 Hz component of the force perpendicular to root acting on each blade.

The magnitudes of the 650 Hz components of the three blades, calculated for either the 32 hole rotors or the 16 hole rotors, are not equal in value. In either case, the simulation has therefore not been run long enough for each of the blades to be struck an approximately equal number of times by the nozzle jets. However, for both the 32 hole rotors and the 16 hole rotors, the amplitudes of the 650 Hz components of blade 2 and blade 3 are within 18 % of the amplitude of the 650 Hz component of blade 1. The magnitudes of the 650 Hz components, obtained for either the 32 hole rotors or the 16 hole rotors, are therefore all close enough in value that further extending the duration of the simulation should not have a significant effect on the magnitudes of these components.

Table 5.3: Magnitudes of the 650 Hz components of the force perpendicular to the root calculated by the 0 ND CFD model for each of the blades.

	Blade 1	Blade 2	Blade 3
32 hole rotors	0.175 N	0.152 N	0.145 N
16 hole rotors	0.233 N	0.211 N	0.202 N

The amplitude of the 650 Hz component of the force perpendicular to the root, estimated from the data of Van der Spuy *et al.* (2012), is expressed by equation (5.4.3) (refer to appendix G). The amplitudes presented in table 5.3 for the 650 Hz components of the three blades, calculated for the 32 hole rotors, all fall within the range of values specified by equation (5.4.3). Unfortunately, no strain data was available to estimate the 650 Hz component of the force perpendicular to the root for the 16 hole rotors.

$$0.0359 \text{ N} < \hat{r}_{\text{perp}} < 0.239 \text{ N} \tag{5.4.3}$$

5.5 Sensitivity to time step size

The transient analysis in section 5.4.2 was repeated for different time step sizes. This was done to determine the effect of time step size on the solution of the 0 ND CFD model. The number of iterations per time step were kept equal to 20 iterations for each of the transient simulations. Ansys CFX uses an implicit time integration scheme (Ansys CFX-Solver Theory Guide, 2012*c*). The solution of

the 0 ND CFD model should therefore be stable irrespective of the time step size used. It is desirable to keep the time step size as large as possible in order to save computation time. However, the time step size still needs to be small enough to resolve the transient behavior of the flow field.

The staggered FSI approach requires that the FE and CFD models both use time steps of the same size. As already suggested in section 4.5, it seemed logical to select a time step size similar to that used by Raubenheimer (2011) for the simulations of the prototype excitation system. The time step size used by Raubenheimer (2011) was 5.5555×10^{-5} s. A time step of 5.4945×10^{-5} s, which is close in value to 5.5555×10^{-5} s, was selected for the transient FE model in section 4.5. The same time step size was therefore also chosen for the 0 ND CFD model in section 5.4.2. If the excitation frequency is 650 Hz, a time step size of 5.4945×10^{-5} s results in there being 28 time steps per period of vibration at the excitation frequency.

The analysis in section 5.4.2 was repeated using time steps of 2.74725×10^{-5} s and 10.989×10^{-5} s. These time steps are half the duration and twice the duration of 5.4945×10^{-5} s, respectively. The simulation was run for 200 time steps for a time step of 10.989×10^{-5} s. The simulation was run for 800 time steps for a time step of 2.74725×10^{-5} s. This corresponds to approximately one rotation of the compressor rotor. The duration of the simulation was selected to be just long enough to evaluate the effect of the time step size on the solution. Only the analysis performed for the 32 hole rotors in section 5.4.2 was repeated.

The force perpendicular to the root, acting on blade 2, is plotted as a function of time in figure 5.7 for all three time step sizes. The curves obtained when using time step sizes of 2.74725×10^{-5} s and 5.4945×10^{-5} s are coincident in the time domain. When using a time step size of 10.989×10^{-5} s, the amplitude of the force perpendicular to the root predicted by the 0 ND CFD model is smaller than the amplitude obtained for time step sizes of 2.74725×10^{-5} s and 5.4945×10^{-5} s. The force perpendicular to the root calculated using a time step size of 10.989×10^{-5} s also does not resolve all of the crests and troughs present in the curves obtained for the other two time step sizes.

Based on the results in figure 5.7, a time step of 5.4945×10^{-5} s was selected for the 0 ND CFD model. This is the largest of the three time step sizes considered that is small enough to resolve the transient oscillations in the flow field. Furthermore, reducing the time step size to 2.74725×10^{-5} s has a negligible effect on the solution. In addition, increasing the time step size above 5.4945×10^{-5} seconds causes the 0 ND CFD model to under predict the amplitude of the blade force.

5.6 Sensitivity to iterations per time step

The transient analysis in section 5.4.2 was repeated in order to determine the effect of the number of iterations per time step on the solution of the 0 ND CFD

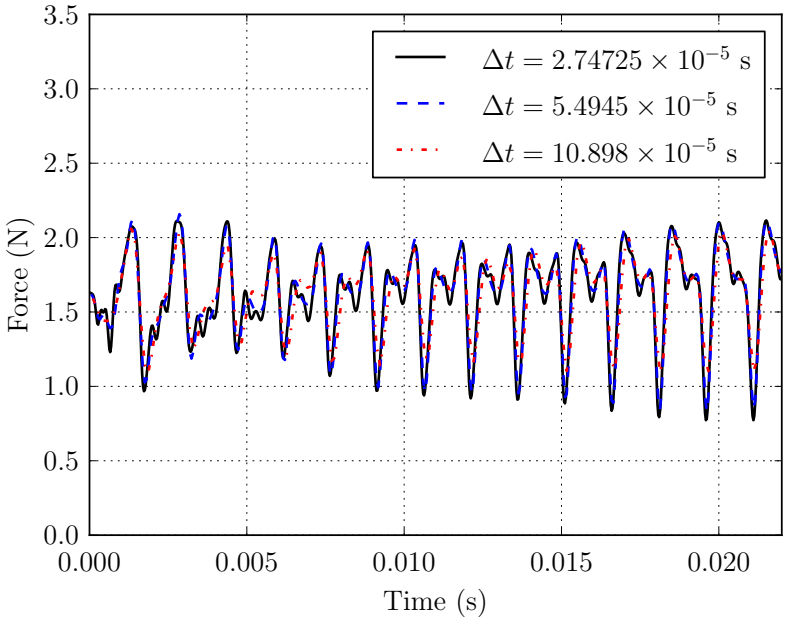

Figure 5.7: Force perpendicular to the root plotted as a function of time for different time step sizes.

model. Only the analysis conducted for the 32 hole rotors in section 5.4.2 was repeated. The number of iterations per time step needs to be large enough to ensure that the solution is converged at the end of each time step. However, at the same time, it is desirable to keep the number of iterations per time step as low as possible to save computation time.

The number of iterations per time step was set to 5 iterations for the transient analysis in section 5.4. This analysis was repeated for 10 iterations and 20 iterations per time step. The time step size used for all three simulations was 5.4945×10^{-5} s. The simulation was run for 400 time steps in each case. The duration of each simulation was set just long enough to evaluate the effect of the number of iterations per time step on the solution.

The force acting on blade 2, in the direction perpendicular to the root, is plotted in figure 5.8 as a function of time for 5 iterations, 10 iterations, and 20 iterations per time step. The curves of the force perpendicular to the root obtained for the three cases are all identical. This indicates that executing more than 5 iterations per time step has no effect on the solution to the 0 ND CFD model. Using 5 iterations per time step is therefore sufficient to obtain a converged solution at the end of each time step.

5.7 Creation of the +2 ND CFD model

This section describes the creation of the +2 ND CFD model. This model was created for the simulation of the +2 ND excitation mode of the vibration ex-

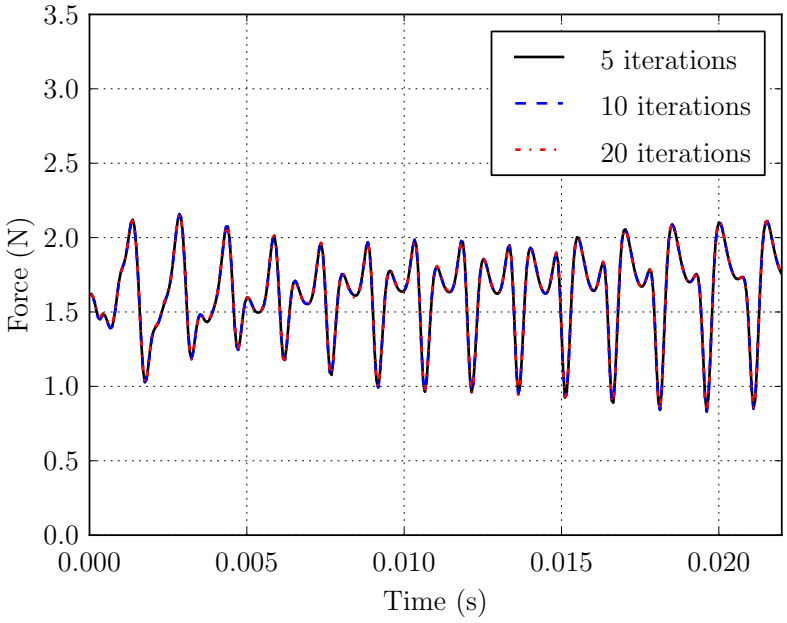

Figure 5.8: Force perpendicular to the root plotted as a function of time for different numbers of iterations per time step.

citation system. When the rotor blades are vibrating in the +2 ND mode, the resulting travelling wave has a period equal to half of the circumference of the rotor blade row. The +2 ND CFD model must therefore contain at least half of the rotor blades and exciter nozzle jets.

The +2 ND CFD model was created by connecting seven copies of the 0 ND CFD model side-by-side at the periodic boundaries. The computational domain of the +2 ND CFD model is shown in figure 5.9. As with the 0 ND CFD model, the blades have been numbered 1 through 21 in the clockwise direction. These numbers are again independent of the blade numbering used in the actual compressor. Since there are multiple patch boundaries, the patches have also been numbered 1 through 7 in the clockwise direction.

As stated in section 5.3.2, the medium mesh was selected for the 0 ND CFD model. Combining seven copies of the medium mesh would result in a mesh for the +2 ND CFD model consisting of 9095856 cells. Running such a large mesh was found to be infeasible due to the large amount of computation time that would be required. In order to reduce the number of cells, a new mesh was therefore created that was a hybrid of the coarse and medium meshes. Seven copies of this hybrid mesh were used to create the mesh for the +2 ND CFD model.

The hybrid mesh had the same number of cells in the inlet region, outlet region, the boundary layer, and the along span of each blade as the medium mesh. However, it had the same mesh density in the blade passages as the coarse mesh. The hybrid mesh contained 685422 cells and 719304 nodes. Combining seven copies of the hybrid mesh resulted in the mesh for the +2 ND CFD model that

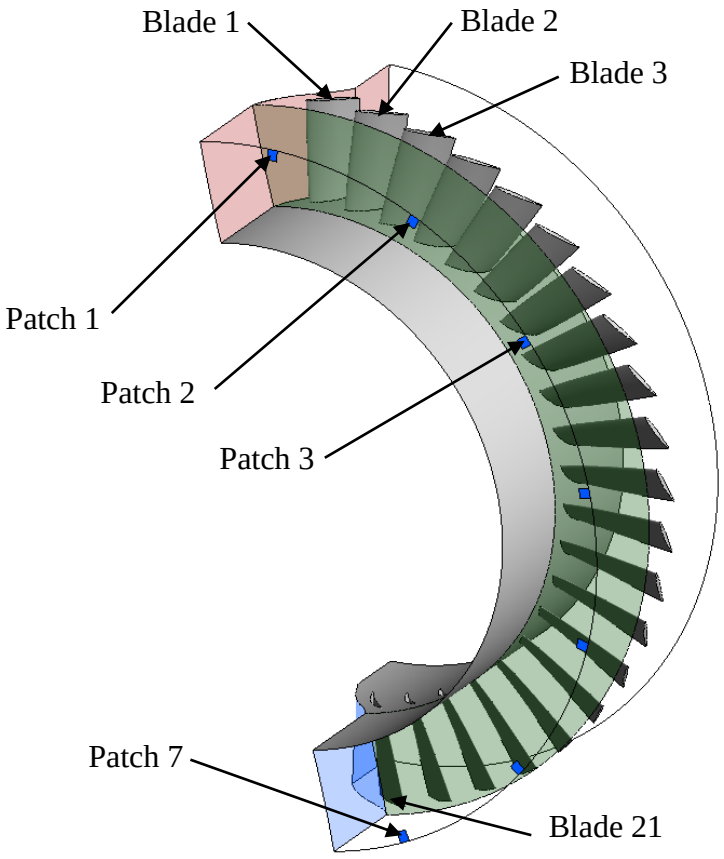

Figure 5.9: Computational domain of the +2 ND CFD model.

contained 4797954 cells and 4993944 nodes.

5.8 Velocity components for the +2 ND mode

As will be discussed in section 5.9.2, the +2 ND CFD model was used to simulate the scenario where the vibration excitation system has been fitted with 32 hole rotors, and is operating at an excitation frequency of 660 Hz and in the +2 ND mode. The experimental velocity profiles presented in chapter 3 indicated that the characteristics of the nozzle jets are not significantly affected by the selected ND mode. The velocity components expressed by equations (5.4.1a) and (5.4.1b), derived for the 0 ND CFD model, were therefore simply modified to represent the nozzle jets of the +2 ND CFD model. The radial and axial velocity components applied to each patch boundary in the +2 ND CFD model are summarized by equations (5.8.1a) and (5.8.1b), respectively. The tangential velocity components at each patch boundary were set equal to zero.

$$V_r = -55.82 - 19.94 \sin\left(2\pi 756t + \frac{2(8 - N_{\text{pb}})\pi}{7}\right) \tag{5.8.1a}$$

$$V_z = 128.4 + 45.85 \sin\left(2\pi 756t + \frac{2(8 - N_{\text{pb}})\pi}{7}\right) \tag{5.8.1b}$$

The variable N_{pb} is the number of the patch to which the velocity components are being applied. In order to obtain the velocity components for the +2 ND CFD model, two modifications were applied to equations (5.4.1a) and (5.4.1b). According to equation (3.2.1a), the pulsation frequency of the nozzle jets must be 756 Hz in order to excite the rotor blades at 660 Hz in the +2 ND mode. The first modification made was therefore that the frequency of the sine function in each velocity component was changed to 756 Hz. The second modification consisted of setting the phase angle of each velocity component to the appropriate value. In order to exciter the +2 ND mode, the pulsation of each nozzle jet must lead the pulsation of the nozzle jet adjacent to it in the same direction that the rotor is rotating in. Equation (3.2.1b) states that the difference in phase angle between adjacent nozzle jets must be 51.4°.

5.9 Simulations for comparison with FSI model

This section contains the transient CFD simulations performed of the vibration excitation experiments of Van der Spuy *et al.* (2012). These simulations were conducted for comparison with the FSI simulations in chapter 6. Two scenarios were simulated. The first scenario simulated was where the vibration excitation system is operating at excitation frequency of 660 Hz, a supply pressure of 2.5 bar, and in the 0 ND mode. This scenario was simulated for both the case where the system has been fitted with the 32 hole rotors, and the case where the system has been fitted with the 16 hole rotors. The second scenario is where the system is operating at the same excitation frequency and supply pressure, but in the +2 ND mode instead. The second scenario was only simulated for the case where the system has been fitted with the 32 hole rotors

5.9.1 Results for the 0 ND mode

The velocity components, representing the nozzle jets for the 0 ND mode of the vibration excitation system, were derived for an excitation frequency of 650 Hz. An excitation frequency of 660 Hz is 10 Hz higher than this value. It was assumed that this difference in excitation frequency was small enough to have a negligible effect on the characteristics of the exciter nozzle jets. The appropriate set of axial and radial velocity components in section 5.4.2, derived to represent either the 32 hole rotors or the 16 hole rotors for the 0 ND, was therefore again specified at the patch boundary. However, this time the frequency of the sine function in each velocity component was changed to 660 Hz. The tangential velocity components at the patch were again set equal to zero.

The time step size selected was 5.4112×10^{-5} s. This is close in value to the time step size of 5.4945×10^{-5} s chosen for an excitation frequency of 650 Hz. A

time step size of 5.4112×10^{-5} s results in there being 28 time steps per period of vibration at 660 Hz. Each transient simulation was conducted for a duration of 4200 time steps. This is equivalent to approximately 10 rotations of the compressor rotor. The number of iterations per time step was set to 5 iterations.

The force perpendicular to the root, acting on blade 2 in the 0 ND CFD model, is plotted in figure 5.10 as a function of time for the 32 hole rotors. The force perpendicular to the root settles into a periodic steady state pattern after 0.025 s. At least two periods of the steady state pattern are visible after this point in time. The blade force predicted using the 0 ND CFD model for the 16 hole rotors was also observed to settle into a steady state pattern after 0.025 s.

The FFT of the force perpendicular to the blade root, acting on blade 2 in the 0 ND CFD model, is plotted in figure 5.11 for both the 32 hole rotors and the 16 hole rotors. Each FFT was computed from the last 3080 samples from the time domain. The samples used to compute each FFT were therefore taken from the portion of the time domain after the force perpendicular to the root had settled into a steady state pattern. A time step size of 5.4112×10^{-5} s means that the samples in the time domain occur at a frequency of 18480 Hz. The resulting FFT therefore has samples in the frequency domain that are spaced at 6 Hz intervals from 0 Hz to 9240 Hz.

It was anticipated that the force perpendicular to root would exhibit components at 660 Hz and 672 Hz, as well as the harmonics of these two components. In order to minimise spectral leakage, the number of samples from the time domain used to calculate each FFT was selected so that the duration of the window of the FFT contained a whole number of periods of each of these components. Spectral leakage arises when the duration of the window of the FFT of a signal does not contain a whole number of periods of all of the components making up the signal. This causes the FFT to exhibit additional spurious components that are not present in the signal.

Both the FFT calculated for the 32 hole rotors and the FFT calculated for the 16 hole rotors, plotted in figure 5.11, exhibit clusters of peaks near 670 Hz, 1340 Hz, 2010 Hz, and 2680 Hz. Figure 5.12 shows that the cluster of peaks near 670 Hz consists of two prominent components at 660 Hz and 672 Hz, and two minor peaks at 648 Hz and 684 Hz. The 660 Hz component is the force at the excitation frequency induced by the pulsating nozzle jets. The 672 Hz component is the component at the nozzle bypass frequency. As already mentioned in section 1.1, the component at the nozzle bypass frequency is caused by the motion of the rotor blades through each of the 14 nozzle jets as the rotor rotates ($672 \text{ Hz} = 14 \times 48 \text{ Hz}$). The component of the force perpendicular to the root at the nozzle bypass frequency is the most prominent component. This was also observed by Raubenheimer (2011) during the CFD simulations of the prototype excitation system. The clusters of peaks at 1340 Hz, 2010 Hz, and 2680 Hz are the harmonics of the components at 660 Hz and 672 Hz. The cause of the minor components at 648 Hz and 684 Hz is unclear.

The magnitudes of the forces acting on the three blades, calculated for the 32 hole

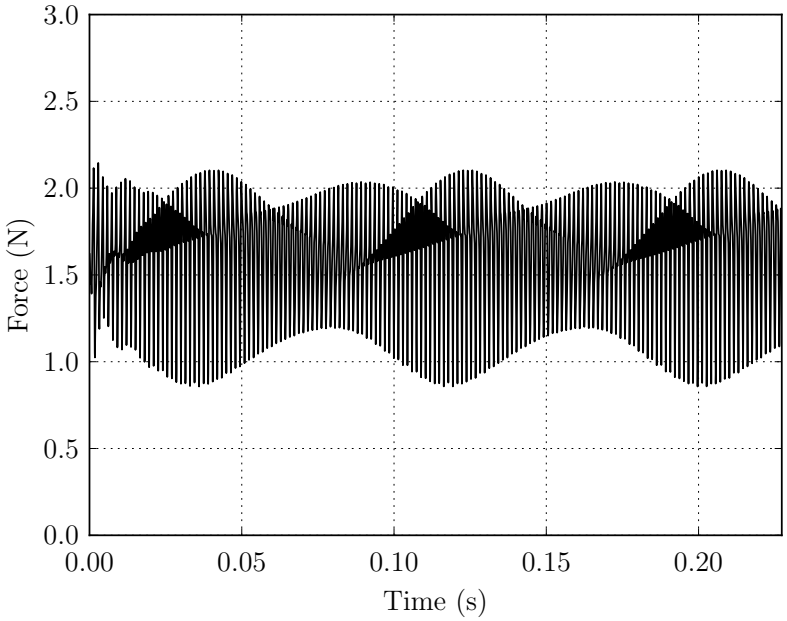

Figure 5.10: Force perpendicular to the root calculated by the 0 ND CFD model for blade 2 for the 32 hole rotors and an excitation frequency of 660 Hz.

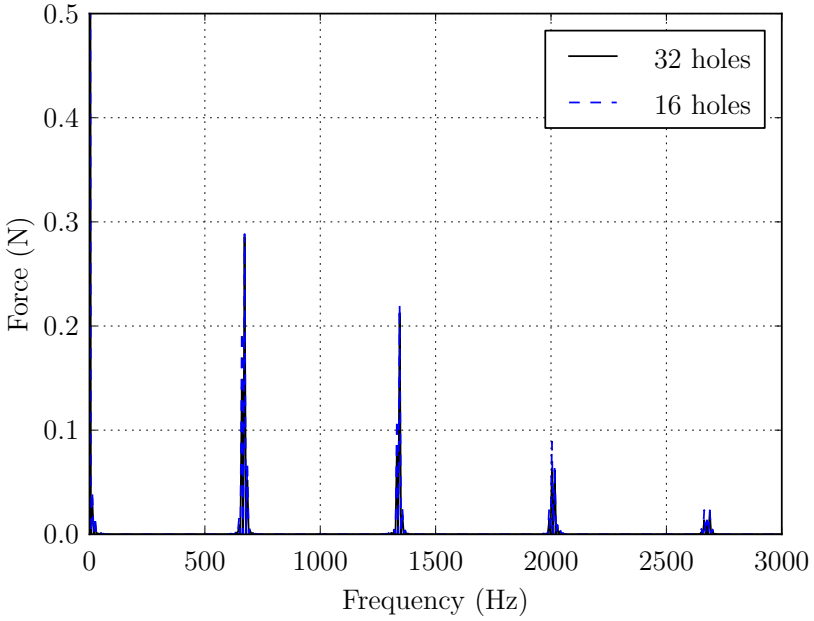

Figure 5.11: FFT of the force perpendicular to the root calculated by the 0 ND CFD model for blade 2 for an excitation frequency of 660 Hz.

rotors, were all identical. This was also the case for the forces computed for the 16 hole rotors. The magnitude of the 660 Hz component of the force perpendicular to the root, calculated for each blade, was 0.142 N for the 32 hole rotors and 0.195 N for the 16 hole rotors. The magnitude of the 650 Hz component calculated for the 16 hole rotors is thus 37 % larger than the component obtained for the 32 hole rotors. This was expected as the amplitude of the axial velocity perturbations measured for the 16 hole rotors in chapter 3 were larger than those measured for the 32 hole rotors.

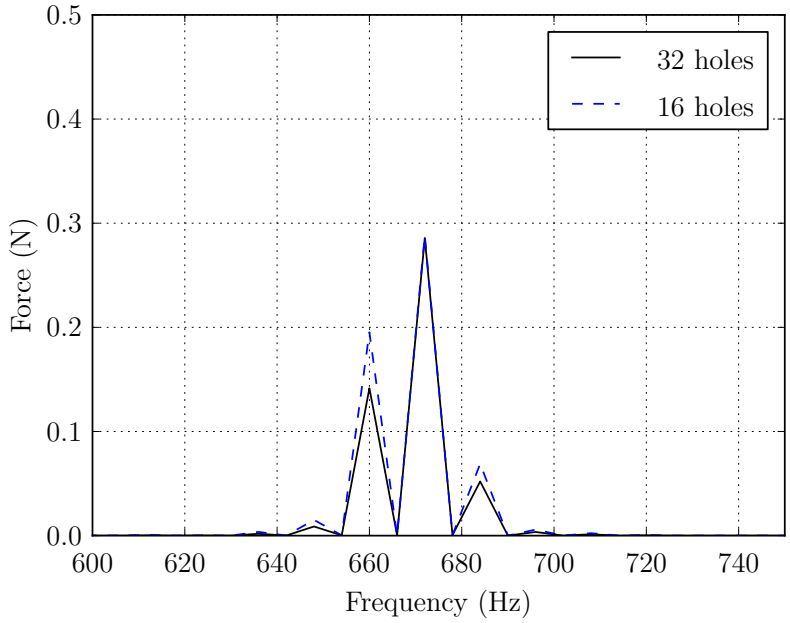

Figure 5.12: Zoomed in view of the FFT of the force perpendicular to the root calculated by the 0 ND CFD model for an excitation frequency of 660 Hz.

Table 5.4 contains the phase angles of the 660 Hz components of the force perpendicular to the root calculated for blade 2 and blade 3 in the 0 ND CFD model. The phase angles in table 5.4 are reported relative to the phase angle of the 660 Hz component of blade 1. Also shown are the values that the phase angle of the 660 Hz component of each blade must have, according to equation (2.1.1), in order to excite the blades in the 0 ND mode. In order to excite the 0 ND mode, the phase angle of the 660 Hz of the component of the force perpendicular to the root must have a value of zero relative to the phase angle of blade 1. The phase angles of the 660 Hz components of both blade 2 and blade 3, relative to blade 1, are within 1° of zero. This is the case for both the 32 hole rotors and the 16 hole rotors. The results from the 0 ND CFD model therefore suggest that the vibration excitation system should be able exert the required force on each of the blade to excite the 0 ND mode of the first rotor blade row. According to the 0 ND CFD model, the vibration excitation system should be capable of achieving this irrespective of whether it is fitted with the 32 hole rotors or the 16 hole rotors.

Table 5.4: Phase angles of the 660 Hz components of the force perpendicular to the root calculated for the blades of the 0 ND CFD model.

	32 hole rotors		16 hole rotors	
	Blade 2	Blade 3	Blade 2	Blade 3
Ideal	0°	0°	0°	0°
CFD model	0.1°	0.2°	0°	0.8°

5.9.2 Results for the +2 ND mode

The radial and axial velocity components at each patch boundary were set equal to equation (5.8.1a) and equation (5.8.1b), respectively. The tangential velocity components at each patch boundary were set equal to zero. The time step size selected for simulation of the +2 ND mode was 5.4112×10^{-5} s. The transient simulation was conducted for a duration of 3600 time steps. The number of iterations per time step was set to 5 iterations.

The force perpendicular to the root, acting on blade 14 in the +2 ND CFD model, is plotted as a function of time in figure 5.13. As was observed for the simulation of the 0 ND mode, the force perpendicular to the root acting on blade 14 settled into a periodic steady state pattern after 0.025 s. Two periods of the steady state pattern are visible in figure 5.13 after this point in time. The forces acting on the other blades in the +2 ND CFD model also settled into a periodic steady state pattern after 0.025 s.

The FFT of the force perpendicular to the root is provided in figure 5.13 for blade 3 and blade 14 in the +2 ND CFD model. Each FFT was calculated using the last 3080 samples from the time domain. The samples were therefore taken from the region of the time domain after the force perpendicular to the root had settled into a steady state trend. In order to minimise spectral leakage, the number of samples used to calculated each FFT was selected so that the window of the FFT contained a whole number of periods of the components at 660 Hz and 672 Hz, as well as the harmonics of these two components. The resulting FFT had samples in the frequency domain that were spaced 6 Hz apart from 0 Hz to 9240 Hz.

The FFT of force perpendicular to the root, acting on blade 3, and the FFT of the force, acting on blade 14, are both plotted in figure 5.14. Each FFT shows groups of peaks near 670 Hz, 1340 Hz, 2010 Hz, and 2680 Hz. The same groups of peaks were also observed for the blade force predicted for the 0 ND mode in section 5.9.1. The zoomed in view in figure 5.15 shows that the group of peaks near 670 Hz again consists of two major peaks at 660 Hz and 672 Hz, and two minor peaks at 648 Hz and 684 Hz. As stated in section 5.9.1, the components at 660 Hz and 672 Hz are the components at the excitation frequency and nozzle bypass frequency, respectively. It is again unclear what the components at 648 Hz and 684 Hz represent. As illustrated in figure 5.15, the FFT obtained for blade 3 and the FFT of blade 14 are identical. This was also the case for the rest of the

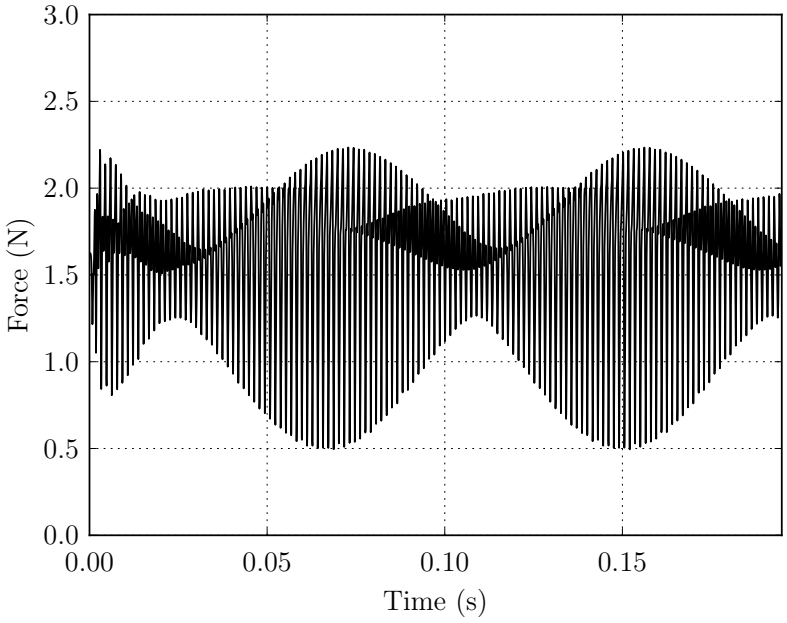

Figure 5.13: Force perpendicular to the root calculated by the +2 ND CFD model for blade 14 for an excitation frequency of 660 Hz.

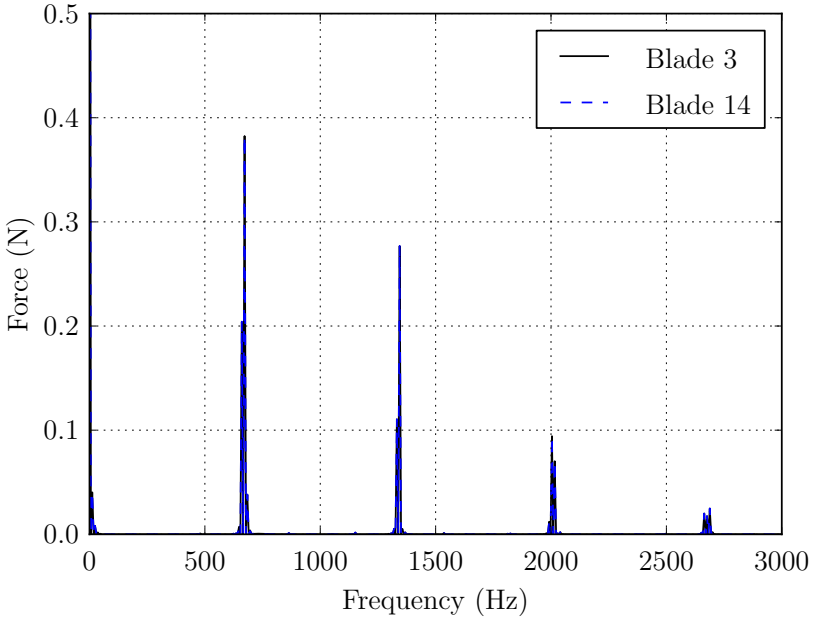

Figure 5.14: FFT of the force perpendicular to the root calculated by the +2 ND CFD model for blade 3 and blade 14 for an excitation frequency of 660 Hz.

blades in the +2 ND CFD model.

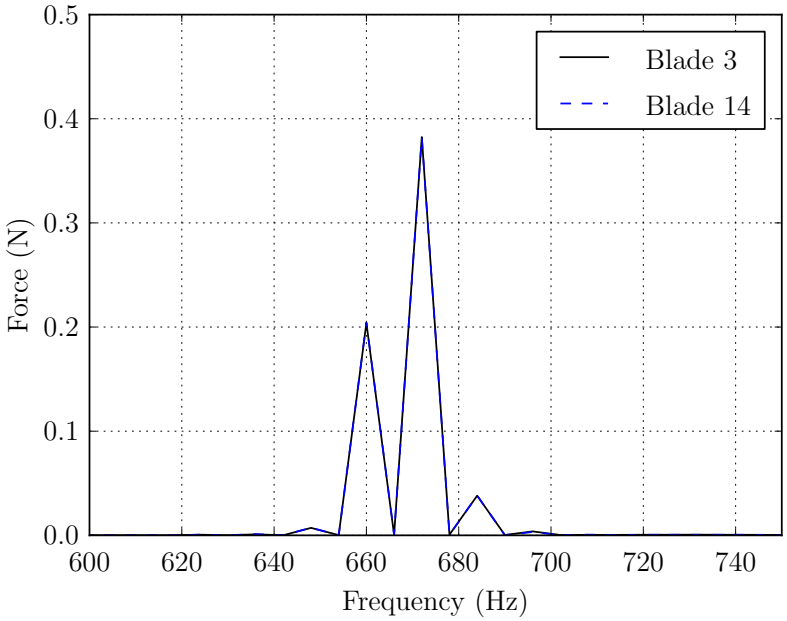

Figure 5.15: Zoomed in view of the FFT of the force perpendicular to the root calculated by the +2 ND CFD model for blade 3 and blade 14 for an excitation frequency of 660 Hz.

The phase angles the 660 Hz components of blade 2, blade 3, blade 8, and blade 14 in the +2 ND CFD model are summarised in table 5.5. The values of the phase angles indicated in table 5.5 are relative to the phase angle of the 660 Hz component of blade 1. Also shown is the value that the 660 Hz component of each blade must have, according to equation (2.1.1), in order to excite the +2 ND mode. The phase angle of the 660 Hz component of each blade was within 0.1° of the value required for the excitation of the +2 ND mode. The results of the +2 ND CFD model therefore indicate that the vibration excitation system should be able to induce the blade forces required to excite the +2 ND mode of the first rotor blade row.

Table 5.5: Phase angles of the 660 Hz components of the force perpendicular to the root calculated for the blades of the +2 ND CFD model.

	Blade 2	Blade 3	Blade 8	Blade 14
Ideal	17.1°	34.3°	120°	223°
CFD model	17.0°	34.4°	120°	223°

Chapter 6

FSI analysis of the rotor blades

This chapter covers the FSI simulations conducted of the vibration excitation system and the first rotor blade row. The simulations involved using the FSI model to recreate the experiments of Van der Spuy *et al.* (2012). Two different experiments were simulated. The first experiment was conducted with the vibration excitation system operating at an excitation frequency of 660 Hz, a supply pressure of 2.5 bar, and in the 0 ND mode. The second experiment was carried out with the system functioning at the same excitation frequency and supply pressure, and in the +2 ND mode. The simulations were performed in order to demonstrate that the FSI model could replicate the operation of the vibration excitation system at or near an excitation frequency of 650 Hz. The 0 ND mode was simulated for both the scenario where the vibration excitation system has been fitted with the 32 hole rotors, and the scenario where system has been fitted the 16 hole rotors. The +2 ND mode was only simulated for the case where the system has been fitted with the 32 hole rotors.

6.1 Settings, boundary conditions, and initial conditions

Two different versions of the FSI model were used for the simulation of the 0 ND and +2 ND modes. The 0 ND CFD model and the 0 ND FE model were coupled together to form the 0 ND FSI model. Similarly, the +2 ND CFD model was coupled to the +2 ND FE model to create the +2 ND FSI model. This sections describes the settings, boundary conditions, and initial conditions selected for both versions of the FSI model. These settings, boundary conditions, and initial conditions were used for all FSI simulations unless otherwise stated.

Coupling the CFD and FE models requires that the wetted surfaces be defined at which the fluid domain and the structural domain meet. During each specific time step, the displacements at the wetted surface, predicted by the FE model, are transferred to the mesh of the CFD model. The aerodynamic forces acting on

the wetted surface are transferred from the CFD model to the FE model during that same time step. The wetted surface consists of the pressure side, suction side, and tip surface of each blade. The wetted surfaces, in both the 0 ND FSI model and the +2 ND FSI model, were defined as a fluid solid interface in both Ansys Mechanical and Ansys CFX-Pre.

The deformation of the mesh, during each time step, causes the cells of the mesh to become distorted. This cell distortion can be severe enough so that the volumes of the cells become negative. This is referred to in the Ansys CFX Reference Guide (2012*a*) as mesh folding. Mesh folding can be reduced by adjusting the stiffness of certain regions of the mesh. The cells in the regions with greater stiffness will then have a higher resistance to deformation.

The cells near the surfaces of each blade are designed to resolve the boundary layer and therefore have small volumes. This means that the cells near the surfaces of each blade cannot tolerate a large amount of mesh deformation before mesh folding occurs. It is therefore desirable to have the majority of the mesh deformation absorbed by the larger cells that are further away from the blade surfaces. The stiffness of the mesh of each CFD model was set in CFX-Pre according to a user defined expression. This created a region of stiffer cells surrounding each blade. The regions of stiffer elements are illustrated in figure 6.1 for the 0 ND CFD model. The user defined expression sets the cells within each region to be 100 times stiffer than the cells lying outside of each region. The mesh deformation was therefore absorbed predominantly by the cells lying outside of each region.

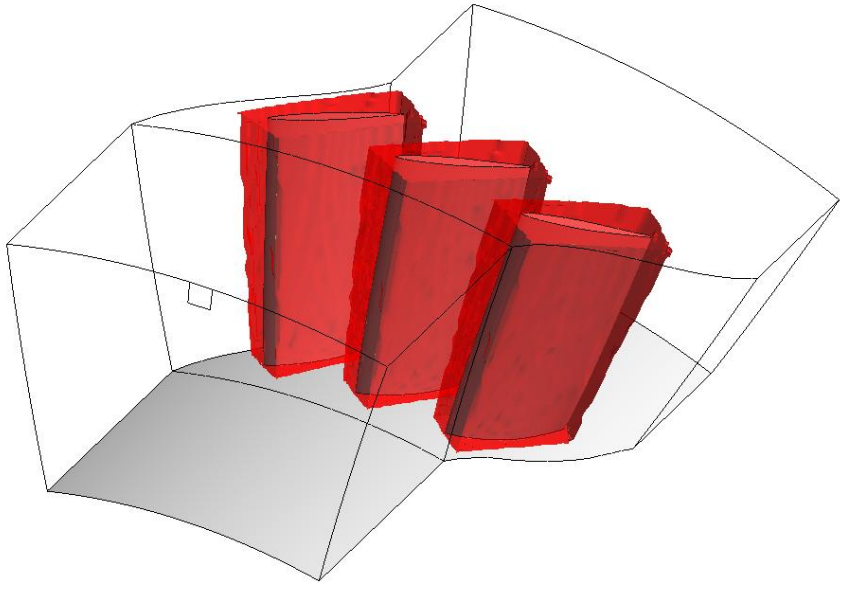

Figure 6.1: Regions of stiffer elements specified for the 0 ND CFD model.

A constant rotational velocity load was applied to the blades in both the 0 ND FE

model and the +2 ND FE model in Ansys Mechanical. The constant rotational load represents the centrifugal load acting on each of the rotor blades. The speed for the constant rotational load was set to 301.6 rad/s (2880 rpm). Damping was deactivated for both of the FE models. The remaining settings and boundary conditions selected for both the 0 ND CFD model and the +2 ND CFD model were the same as those used for the transient CFD simulations in section 5.9.

Initial conditions had to be specified for both the FE model and the CFD model that make up each FSI model. The initial conditions of the CFD model and the FE model together form the initial conditions of the FSI model. The initial conditions of each CFD model was at first set equal to the same steady state solution used as the initial conditions for that CFD model during the transient CFD simulations in section 5.4.2. Correspondingly, the initial conditions for each FE model were defined so that the blades were initially undeformed and at rest. However, specifying the initial conditions of each FSI model in this manner caused each blade to experience spurious vibrations at the natural frequency of the first bending mode. A more appropriate set of initial conditions was therefore derived for each of the FSI models.

The new set of initial conditions were obtained by conducting an FSI simulation of the compressor flow field with the vibration excitation system switched off. During these simulations, the structural damping in each FE model was set to a relatively large value in order to damp out the spurious vibrations. Details of these simulations are provided in appendix H. Once the spurious vibrations had decayed away, structural damping was deactivated for the simulations of the 0 ND and +2 ND modes. Separate sets of initial conditions were obtained for the 0 ND FSI model for the 32 hole rotors and 16 hole rotors. A set of initial conditions was also calculated for the +2 ND FSI model for the 32 hole rotors.

The FE analysis in section 4.5 revealed that a time step size of 5.4112×10^{-5} s is small enough to resolve the motions of the blades. The CFD analysis section 5.5 showed that this time step size is also sufficiently small to resolve the transient behaviour of the flow field. Both Ansys CFX and Ansys Mechanical utilise an implicit time integration scheme. As already discussed in section 2.4, coupling the FE model and the CFD model may cause the time integration scheme of the resulting FSI model to behave like an explicit scheme. A time step size of 5.4112×10^{-5} s may therefore not be small enough to resolve the transient behaviour in each FSI model. However, due to time constraints, it was not possible to investigate the effect of using of a smaller time step size. As will be discussed is section 6.3 and section 6.4, a time step size of 5.4112×10^{-5} s produced results that correlated sufficiently well with the data of Van der Spuy *et al.* (2012). A time step size of 5.4112×10^{-5} s was therefore still selected for each FSI model. A time step size of 5.4112×10^{-5} s means that there are 28 time steps per cycle of vibration at the excitation frequency of 660 Hz. The duration of each FSI simulation was set to 4400 time steps. This is equivalent to approximately 12 rotations of the compressor rotor.

A FSI analysis was performed in order to determine the effect of the number of

stagger iterations per time step on the solution. Further details of this analysis are provided in appendix I. It is desirable to keep the number of stagger iterations as low as possible in order to save computation time. However, the number of stagger iterations must be large enough to ensure that the solutions to the FE model and the CFD model are sufficiently synchronized at the end of each time step. The analysis was conducted for 1 iteration, 2 iterations, and 6 iterations per time step. The solutions to the FSI model were almost identical for each case. The results of the FSI model were therefore not significantly dependent on whether a strong staggered coupling or weak staggered coupling is adopted. The number of stagger iterations per time step was therefore set equal to 1 iteration which corresponds to a weak staggered coupling.

6.2 Prediction of blade forces

This section provides a brief discussion of the blade forces predicted by the 0 ND FSI model and the +2 ND FSI model. A more detailed discussion of the blade forces is presented in appendix J. The blade forces obtained using each FSI model were compared to the corresponding transient CFD simulations covered in section 5.9. The blade forces calculated using the 0 ND FSI model were compared to the results of the 0 ND CFD model from section 5.9.1. Similarly, the blade forces calculated using the +2 ND FSI model were compared to the results of the +2 ND FSI model in section 5.9.2.

A FFT was computed of the force perpendicular to the root obtained from the results of the 0 ND FSI model. The magnitude of each FFT revealed clusters of peaks near 670 Hz, 1340 Hz, 2010 Hz, and 2680 Hz in the frequency domain. The same clusters of peaks were also present in the FFT computed of the blade force from the transient CFD simulations in section 5.9.1. As was observed during the transient CFD simulations, the cluster of components near 670 Hz again contained two prominent peaks at 660 Hz and 672 Hz. The cluster of peaks near 670 Hz also again exhibited two minor components at 648 Hz and 684 Hz.

The peaks at 660 Hz and 672 Hz were the components at the excitation frequency and the nozzle bypass frequency, respectively. It has already been stated in section 5.9.1 that it is unclear what the components at 648 Hz and 684 Hz represent. The remaining clusters of peaks are the harmonics of the 660 Hz and 672 Hz components. The 660 Hz component of the force perpendicular to the root, obtained using the 0 ND FSI model for the 16 hole rotors, was larger than that obtained for the 32 hole rotors. This was also observed from the results of the transient CFD simulations of the 0 ND mode. The magnitude of the 660 Hz component of each blade in the 0 ND FSI model was 5 % lower than the magnitude of the 660 Hz component for the same blade during the transient CFD simulations. This was the case for both the 32 hole rotors and the 16 hole rotors.

A FFT was also calculated from the force perpendicular to the root acting on each blade in the +2 ND FSI model. As was observed from the results of the 0 ND FSI model, and the transient CFD simulation of the +2 ND mode in section 5.9.2, the FFT again showed groups of peaks near 670 Hz, 1340 Hz, 2010 Hz, and 2680 Hz. The group of peaks near 670 Hz was again composed of components at the excitation frequency of 660 Hz and the nozzle bypass frequency of 672 Hz, as well as components at 648 Hz and 684 Hz. The amplitude of the 660 Hz component for each blade in the +2 ND FSI model was 7 % lower than the amplitude calculated for the same blade during the transient CFD simulation of the +2 ND mode.

The transient CFD simulations in section 5.9 neglect the influence of the vibrations of the blades on the blade force. However, the blade forces calculated during the FSI simulations do take the motions of the blades into account. The fact that the blade forces predicted by the FSI simulations and the transient CFD simulations are similar therefore indicates that the vibrations of the blades have a negligible effect on the blade force. This suggests that a transient CFD model is sufficient for accurately predicting the force acting on each blade. It also suggests that it should be possible to adequately model the motions of the blades using a one-way staggered FSI model. In a one-way staggered FSI model, the blade deflections are not transferred from the FE model to the CFD model. This eliminates the problem of mesh folding as the mesh of the CFD model is not deformed during each time step.

6.3 Displacements and strains from the 0 ND FSI model

6.3.1 Tip displacement

The tip displacement perpendicular to the root, computed using the 0 ND FSI model for blade 2, is plotted as a function of time in figure 6.2 for the 32 hole rotors. As mentioned in section 6.2, the force acting on each blade settled into a periodic pattern steady after approximately 0.025 s. No such periodic steady state pattern is discernible from the tip displacement in figure 6.2.

A FFT was computed from the tip displacement perpendicular to the root obtained for blade 2 using the 0 ND FSI model. The FFT of the tip displacement perpendicular to the root is plotted in figure 6.3 for both the 32 hole rotors and 16 hole rotors. Each FFT was computed from the last 3080 samples in the time domain. This resulted in an FFT with samples in the frequency domain that are spaced 6 Hz apart from 0 Hz to 9240 Hz. In section 6.2 it was stated that the force acting on each blade in the 0 ND FSI model, in the direction perpendicular to the root, contained prominent components at 660 Hz and 672 Hz, as well as the harmonics of these two components. It was therefore anticipated

that the tip displacement of each blade, in the direction perpendicular to the root, would also feature these components. The number of samples from the time domain used to calculated each FFT was selected so that the window of the FFT contained a whole number of periods of the 660 Hz component, the 672 Hz component, and the harmonics of these two components.

Figure 6.3 shows two prominent components at 660 Hz and 672 Hz, as well as two minor components at 648 Hz and 684 Hz. The components at 660 Hz and 672 Hz are the components at the excitation frequency and the nozzle bypass frequency, respectively. The minor components at 648 Hz and 684 Hz were also exhibited by the blade forces from the transient CFD analyses in section 5.9.1 and the 0 ND FSI model in section 6.2. As was stated in section 5.9.1 and section 6.2, the cause of the components at 648 Hz and 684 Hz is unclear and requires further investigation.

The blade forces from the transient CFD simulations in section 5.9.1, and the 0 ND FSI model in section 6.2 also exhibited clusters of peaks near 1340 Hz, 2010 Hz, and 2680 Hz. These clusters of peaks are not present in the FFT of the tip displacement calculated for either the 32 hole rotors or the 16 hole rotors. According to equation (2.2.13), the influence of a specific force component on the blade response decreases the further the frequency of the component is from the natural frequencies of the blade. The components near 1340 Hz, 2010 Hz, and 2680 Hz may therefore not be visible in the tip displacement as the frequencies of these components are not close enough to the natural frequency of the first bending mode.

The duration of the window of each FFT contains a whole number of periods of the components at 648 Hz, 660 Hz, 672 Hz and 684 Hz. The FFT should therefore not exhibit any spectral leakage if the tip displacement only consists of these four components and the component at 0 Hz. All of the samples in the frequency domain should therefore have a magnitude of zero except for the samples at 0 Hz, 648 Hz, 660 Hz, 672 Hz and 684 Hz. However, the sample occurring at 654 Hz is non-zero. This indicates that the FFT must contain another component between 654 Hz and 660 Hz. According to equation 2.2.15, the response of a mechanical system, induced by an excitation force, includes a component of vibration at the natural frequency. The FE analysis in section 4.4 showed that the natural frequency of the first bending mode of each blade increases from 649 Hz to 658 Hz due to the centrifugal loads acting on the rotor blade row. The component lying between 654 Hz and 660 Hz must therefore be the response at the natural frequency of the first bending mode.

It is desirable to compute the FFT of the tip displacement using samples from the region of the time domain after the tip displacement has settled into a periodic steady state trend. As already mentioned, no periodic steady state pattern is apparent in figure 6.2. However, it is still possible that the tip displacement has settled into a periodic steady state pattern, and that the selected duration of the simulation is simply not long enough for the steady state trend to be visible. The period of the tip displacement is equal to the period of the shortest segment

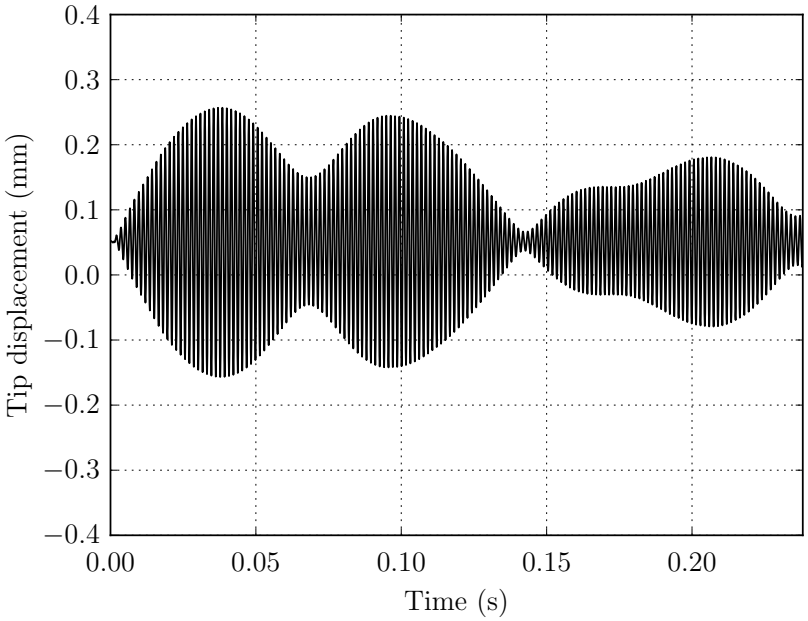

Figure 6.2: Tip displacement perpendicular to the root calculated by the 0 ND FSI model for blade 2 for the 32 hole rotors and an excitation frequency of 660 Hz.

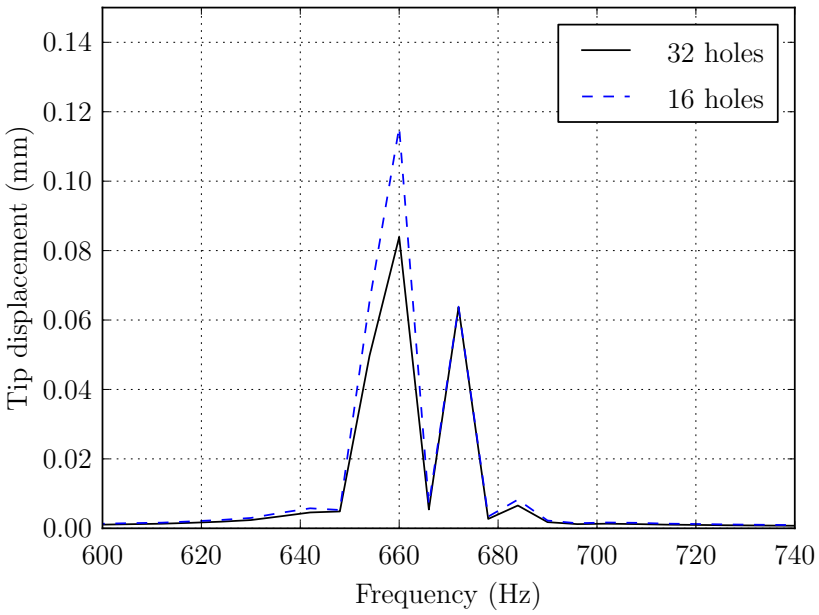

Figure 6.3: FFT of the tip displacement perpendicular to the root calculated by the 0 ND FSI model for blade 2 for an excitation frequency of 660 Hz.

of time that contains a whole number of periods of all of the components which make up the tip displacement.

The shortest segment of time that contains a whole number of periods of the components at 648 Hz, 658 Hz, 660 Hz, 672 Hz and 684 Hz is 0.5 s. This segment of time is equivalent to 9240 time steps. Running each FSI simulation for 9240 time steps was not feasible due to the computation time that would be required. A different criteria for establishing whether the tip displacement had settled into a periodic steady state pattern was therefore devised.

It was observed that the FFT of the tip displacement computed for the three blades all become increasingly similar as the duration of the simulation is extended. This means that if the duration of the simulation is set long enough, the FFTs of the three blades will all eventually be identical and constant with respect to time. The same behaviour was also observed in section 5.9.1 and section 6.2 from the force acting on each blade. As already explained in section 5.9.1, a signal has settled into a periodic steady state pattern when the amplitudes of all of the components making up the signal are constant with respect to time. This means that when the tip displacement of each blade has settled into a periodic steady state pattern, the magnitudes of the FFTs computed for the three blades will be the same.

The tip displacement perpendicular to the root was deemed to have settled into a periodic steady state pattern when the magnitudes of the 660 Hz components of blade 2 and blade 3 were both within 10 % of the magnitude of the 660 Hz component of blade 1. The duration of each FSI simulation was therefore extended until the FFT of the tip displacement of each blade satisfied this condition. This condition was found to be satisfied when the duration of the simulation was set equal to 4400 time steps. The last 3080 samples in the time domain were used to compute each FFT.

Van der Spuy *et al.* (2012) used equation (3.3.2b) to estimate the tip displacement of each rotor blade, in the direction perpendicular to the root, from the bridge voltage of the strain gauge assembly attached to blade 25. The bridge voltage was recorded by Van der Spuy *et al.* (2012) with the vibration excitation system fitted with the 32 hole rotors, and functioning at an excitation frequency of 660 Hz, a supply pressure of 2.5 bar, and in the 0 ND mode. As reported in appendix B, the magnitude of 660 Hz component of the tip displacement perpendicular to root, when the system is operating under these settings, was estimated by Van der Spuy *et al.* (2012) to be 0.089 mm for each blade. The magnitude of the 660 Hz component of each blade, predicted using the 0 ND FSI model for the 32 hole rotors, was found to be within 6 % of the value estimated by Van der Spuy *et al.* (2012) from the bridge voltage.

The correlation between the magnitude of the 660 Hz component estimated by Van der Spuy *et al.* (2012) and the results of the 0 ND FSI model was deemed to be satisfactory for the 32 hole rotors. Unfortunately, no vibration data was available to estimate the magnitude of 660 Hz component of the tip displacement perpendicular to the root for the 16 hole rotors. The magnitude of the 660 Hz

component computed for each blade, using the 0 ND FSI model for the 16 hole rotors, was approximately 30 % larger than the magnitude of the 660 Hz component calculated for the same blade for the 32 hole rotors. This result was expected as the magnitude of the 660 Hz component of the blade force calculated using the 0 ND FSI model for the 16 hole rotors was larger than the magnitude of the 660 Hz component calculated for the 32 hole rotors.

Table 6.1 summarises the phase angles of the 660 Hz components of the tip displacements of blade 2 and blade 3 in the 0 ND FSI model. Also shown in table 6.1 are the ideal values that 660 Hz components of the tip displacement of the blades must have, according to equation (2.1.1), for the first rotor blade row to be vibrating in the 0 ND mode. The values of the phase angles are all reported relative to the phase angle of the 660 Hz component of blade 1. In order for the first rotor blade row to be excited in the 0 ND mode, equation (2.1.1) states that the phase angles of the 660 Hz components of blade 2 and blade 3 should both be zero relative to blade 1. The phase angles of 660 Hz components of blade 2 and blade 3, computed for both 32 hole rotors and 16 hole rotors, are all within 5° of zero. The agreement between the phase angles from the 0 ND FSI model and ideal phase angles, for both the 32 hole rotors and the 16 hole rotors, was considered close enough to deem that the blades are vibrating at 660 Hz in the 0 ND. The results of the 0 ND FSI model therefore indicate that the vibration excitation system should be able to excite the 0 ND mode, at or near a frequency of 660 Hz, regardless of whether the system is fitted with the 32 hole rotors or the 16 hole rotors.

Table 6.1: Phase angles of the 660 Hz components of the tip displacement perpendicular to the root calculated for the blades of the 0 ND FSI model.

	32 hole rotors		16 hole rotors	
	Blade 2	Blade 3	Blade 2	Blade 3
Ideal	0°	0°	0°	0°
FSI model	−2°	4°	−3°	3°

6.3.2 Visualisation of the vibration of each blade

A segment of the time domain showing the motion of each of the three blades, predicted by the 0 ND FSI model for the 32 hole rotors, is presented in figure 6.4. Also indicated in figure 6.4 are six instants in time that have been labelled a) through f). The six moments in time correspond to the snapshots in figure 6.5. In each snapshot, fourteen copies of the results from the 0 ND FSI model have been plotted side by side to give an impression of the vibration of the entire blade row. The numbers assigned to the blades in each of the snapshots are the same blade numbers defined in figure 5.1.

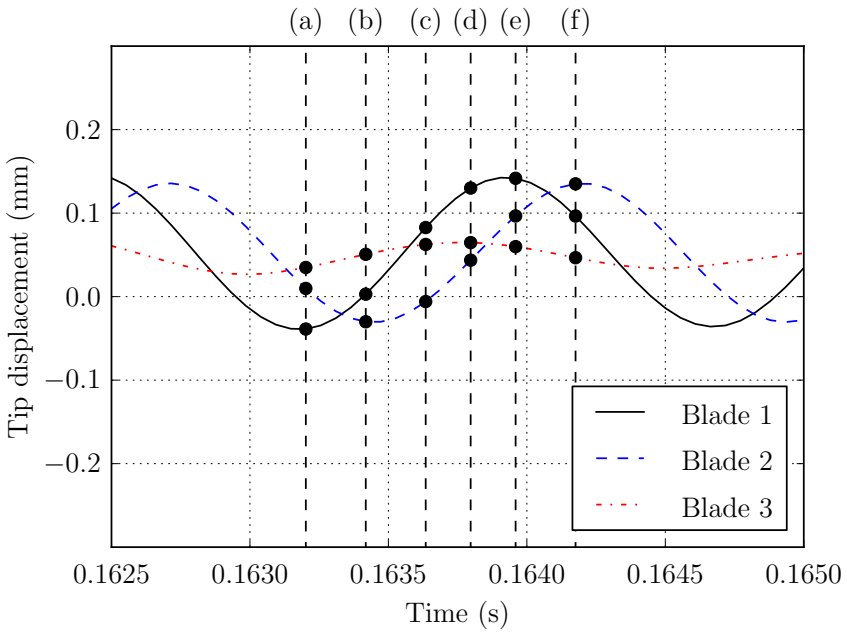

Figure 6.4: Section of the time domain showing the motions of each of the blades in the 0 ND FSI model.

At $t = 0.163202$ s (figure 6.5a), the tip deflection of blade 1 has just reach its minimum value. At the same moment of time, the deflection of blade 2 is close to zero. The tip deflection of blade 1 has increased to zero by $t = 0.163421$ s (figure 6.5b). The tip deflection of blade 2 has now decreased to its minimum value. At $t = 0.163634$ s (figure 6.5c), the tip deflection of blade 1 is approaching its maximum value. The tip deflection of blade 2 has increased back to zero. Blade 1 has reached its maximum tip deflection at $t = 0.163960$ s (figure 6.5e). At this instant, blade 2 is still approaching its maximum value. The tip deflection of blade 1 is decreasing again by $t = 0.164176$ s (figure 6.5f). The tip deflection of blade 2 has now reached its maximum value. As shown in figure 6.4, the amplitude of the tip deflection of blade 3 is significantly smaller than the amplitudes of the other two blades. The contours of total mesh displacement for blade 3 therefore show almost no change from one snapshot to the next.

In section 6.3.1, it was concluded that the blades in the 0 ND FSI model were vibrating at 660 Hz in the 0 ND mode. The 660 Hz components of the tip displacement of the three blades were therefore all in phase. However, figure 6.4 and figure 6.5 show that this does not guarantee that the overall motions of the blades are also in phase. In section 6.3.1, it was found that the 660 Hz components of the three blades were all similar in amplitude. Despite this fact, figure 6.4 and figure 6.5 show that the amplitudes of the overall motions of the blades are all different. The differences in phase and amplitude, observed between the 660 Hz component of the tip displacement and the overall tip displacement, are the result of the additional components at 648 Hz, 658 Hz, 672 Hz and 684 Hz.

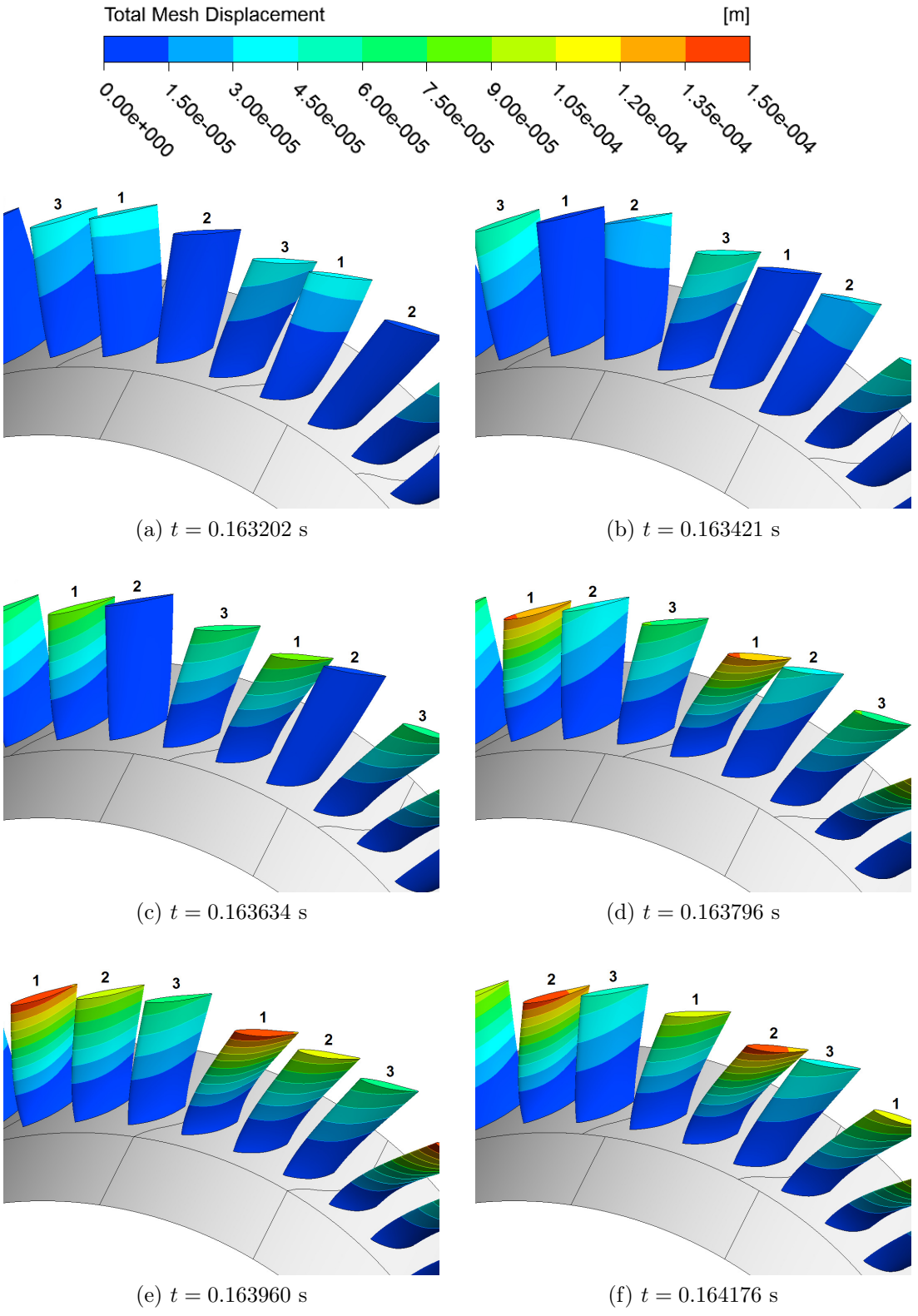

(a) $t = 0.163202$ s

(b) $t = 0.163421$ s

(c) $t = 0.163634$ s

(d) $t = 0.163796$ s

(e) $t = 0.163960$ s

(f) $t = 0.164176$ s

Figure 6.5: Deformation of the blades in the 0 ND FSI model at six snapshots in time.

6.3.3 Bending strain

As stated in section 3.3.2, equation (3.3.2b) was used by Van der Spuy *et al.* (2012) to estimate the tip displacement. The tip displacement estimated by Van der Spuy *et al.* (2012) was then compared to the results of the 0 ND FSI model. However, equation (3.3.2b) is based on the assumption that the shape of the blade during vibration resembles the shape that the blade deforms into when it is subjected to a concentrated tip load. The bending strain predicted by the 0 ND FSI model was therefore also compared to the bending strain measured by the strain gauge assembly, attached to blade 25 in the actual compressor, during the experiments of Van der Spuy *et al.* (2012). The bending strain is related to the bridge voltage of the strain gauge assembly by equation (3.3.3). Equation (3.3.3) is derived from the physical characteristics of the strain gauge assembly and does not rely on any assumptions regarding the deformation of the blade. The bending strain is therefore a better quantity for verifying the FSI model as it is directly detected by the strain gauge assembly.

A FFT of the bending strain, computed by the 0 ND FSI model for blade 2, is provided in figure 6.6. The bending strain plotted in figure 6.6 for each blade is the bending strain calculated by the 0 ND FSI model at the point on the blade surface corresponding to the center of the pressure side strain gauge. The last 3080 samples from the time domain were used to compute the FFT of the bending strain. As was observed from the tip displacement in section 6.3.1, the FFT of the bending strain exhibited peaks at 648 Hz, 660 Hz, 672 Hz and 684 Hz. The peaks at 660 Hz and 672 Hz are the components at the excitation frequency and the nozzle bypass frequency, respectively. The non-zero sample at 654 Hz again indicates that the FFT contains a component at 658 Hz. This component must again be the natural frequency of the first bending mode.

The magnitude of 660 Hz component of the bending strain, computed using equation (3.3.3) from the bridge voltage measured by Van der Spuy *et al.* (2012), was 0.093 mm/m. This value is also reported in appendix B. The magnitude of the 660 Hz components of the blades, calculated using the 0 ND FSI model for the 32 hole rotors, are all between 10 % and 20 % lower than the value calculated from the data of Van der Spuy *et al.* (2012). The correlation between the bending strain from the 0 ND FSI model and the data of Van der Spuy *et al.* (2012) was therefore worse than the correlation obtained for the tip displacement. However, the superior correlation observed for the tip displacement may simply be due to the error in the tip displacement estimated by Van der Spuy *et al.* (2012). Despite this fact, the correlation between the 660 Hz component of the bending strain, computed using the 0 ND FSI model for the 32 hole rotors, and bending strain from the data of Van der Spuy *et al.* (2012) was still deemed to be acceptable. The magnitude of the 660 Hz component of each blade, computed using the 0 ND FSI model for the 16 hole rotors, was approximately 30 % larger than the magnitude of the 660 Hz component calculated for that same blade for the 32 hole rotors.

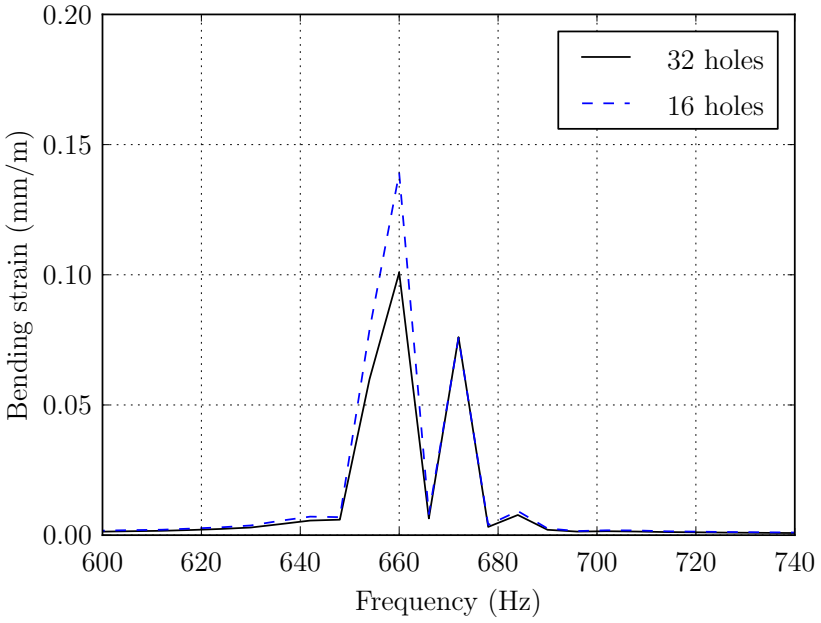

Figure 6.6: FFT of the bending strain calculated by the 0 ND FSI model for blade 2 for an excitation frequency of 660 Hz.

6.4 Displacements and strains from the +2 ND FSI model

6.4.1 Tip displacement

The tip displacement perpendicular to the root, computed for blade 14 by the +2 ND FSI model, is plotted as a function of time in figure 6.7. The FFT of the tip displacement perpendicular to the root, computed using the +2 ND FSI model, is plotted in figure 6.8 for blade 3 and blade 14. The tip displacement was considered to have settled into a steady state pattern once the magnitudes of the 660 Hz components of blades 2 through 21 were all within 10 % of the magnitude of the 660 Hz component of blade 1. It was found that this condition was met when the duration of the simulation was set to 4400 time steps. The window used for the calculation of each FFT consisted of the last 3080 samples in the time domain. This resulted in an FFT with the samples in the frequency domain spaced at intervals of 6 Hz between 0 Hz and 9240 Hz. The number of samples from the time domain used to calculated each FFT was selected so that the window of the FFT contained a whole number of periods of the components at 660 Hz and 672 Hz, as well as the harmonics of these two components. This was again done to minimise spectral leakage.

Each FFT in figure 6.8 exhibits peaks at 648 Hz, 660 Hz, 672 Hz and 684 Hz. The same peaks were present in the FFT of the tip displacement calculated for the 0 ND mode in section 6.4.1. The peaks at 660 Hz and 672 Hz again represent the components at the excitation frequency and the nozzle bypass frequency,

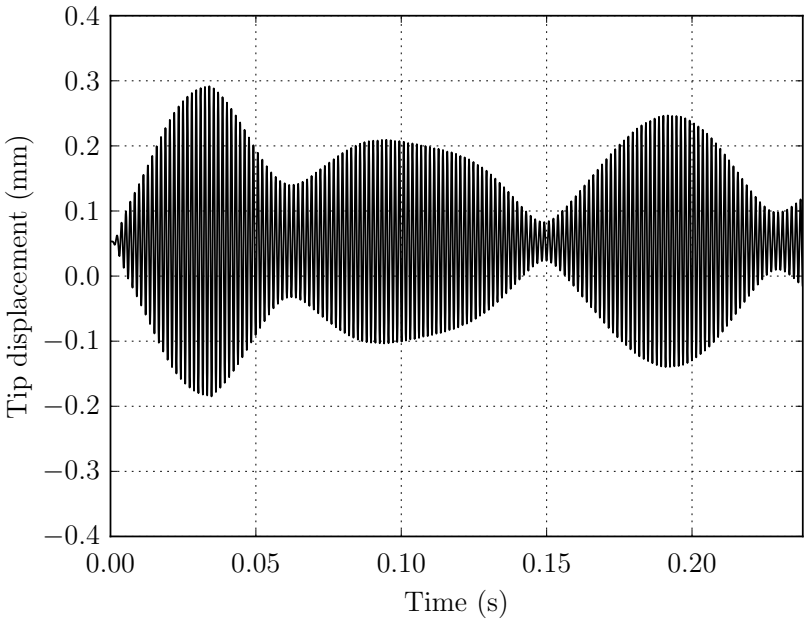

Figure 6.7: Tip displacement perpendicular to the root calculated by the +2 ND FSI model for blade 14 for an excitation frequency of 660 Hz.

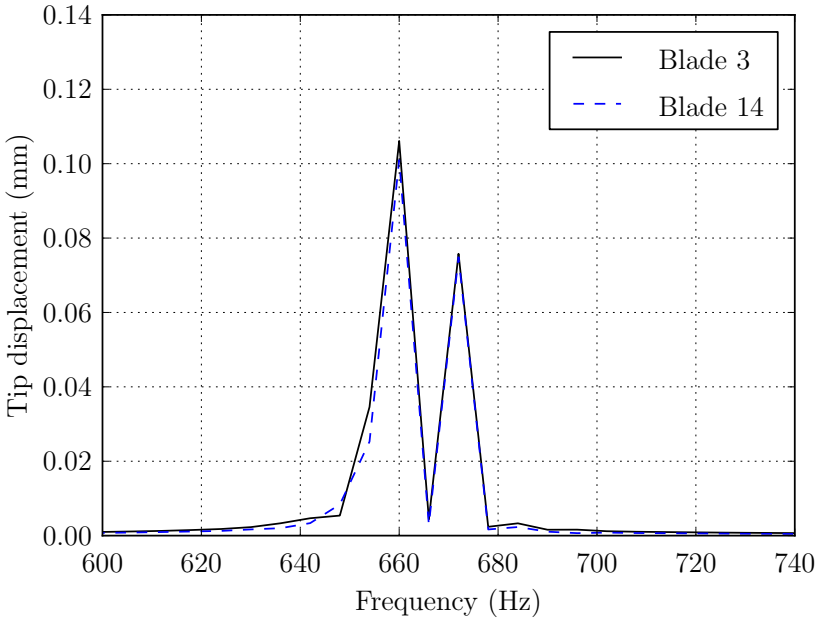

Figure 6.8: FFT of the tip displacement perpendicular to the root calculated by the +2 ND FSI model for blade 3 and blade 14 for an excitation frequency of 660 Hz.

respectively. As stated in section 6.4.1, it is unclear what the cause is of the components at 648 Hz and 684 Hz. The non-zero sample at 654 Hz again indicates that the tip displacement must contain a component at the natural frequency of the first bending mode of 658 Hz.

Using equation (3.3.2b), Van der Spuy *et al.* (2012) estimated the magnitude of 660 Hz component of the tip displacement, in the direction perpendicular to root, of blade 25 in the actual compressor to be 0.105 mm for the +2 ND mode. This value is also reported in appendix B. The estimate is based on the bridge voltage measured by Van der Spuy *et al.* (2012) with the vibration excitation system fitted with the 32 hole rotors, and operating at an excitation frequency of 660 Hz, a supply pressure of 2.5 bar, and in the +2 ND mode. The magnitudes of the 660 Hz component of each of the blades were all within 6 % of the value estimated by Van der Spuy *et al.* (2012). This is approximately the same discrepancy found between the tip displacement from the 0 ND FSI model and the value by Van der Spuy *et al.* (2012) for the 0 ND mode.

The phase angles for the 660 Hz components of the tip displacement perpendicular to root are presented in table 6.2 for blade 2, blade 3, blade 8, and blade 14 in the +2 ND FSI model. The values of the phase angles in table 6.2 are all reported relative to the phase angle of the 660 Hz component of blade 1. Also shown in table 6.2 is the ideal value that the phase angle of each blade must have, according to equation (2.1.1), in order to excite the +2 ND mode. The phase angles of the 660 Hz components of the blades are all within 3° of the ideal values. The correlation between the phase angles from the +2 ND FSI model and the ideal phase angles was deemed sufficient to conclude that the blades in the +2 ND FSI model are vibrating at 660 Hz in the +2 ND mode. The results of the +2 ND FSI model therefore indicate that the vibration excitation system should be able to excite the +2 ND mode at or near a frequency of 660 Hz.

Table 6.2: Phase angles of the 660 Hz components of the tip displacement perpendicular to the root calculated for the blades of the +2 ND FSI model.

	Blade 2	Blade 3	Blade 8	Blade 14
Ideal	17.1°	34.3°	120°	223°
FSI model	18.8°	31.3°	118°	222°

6.4.2 Bending strain

The FFT of the bending strain, calculated using the +2 ND FSI model for blade 3 and blade 14, is plotted in figure 6.9. The bending strain reported in figure 6.9 was the bending strain predicted for each blade at the location on the blade surface corresponding to the center of the pressure side strain gauge. The FFT of the bending strain of each blade contains peaks at 648 Hz, 660 Hz, 672 Hz and 684 Hz. The peaks at 660 Hz and 672 Hz are the components at the excitation

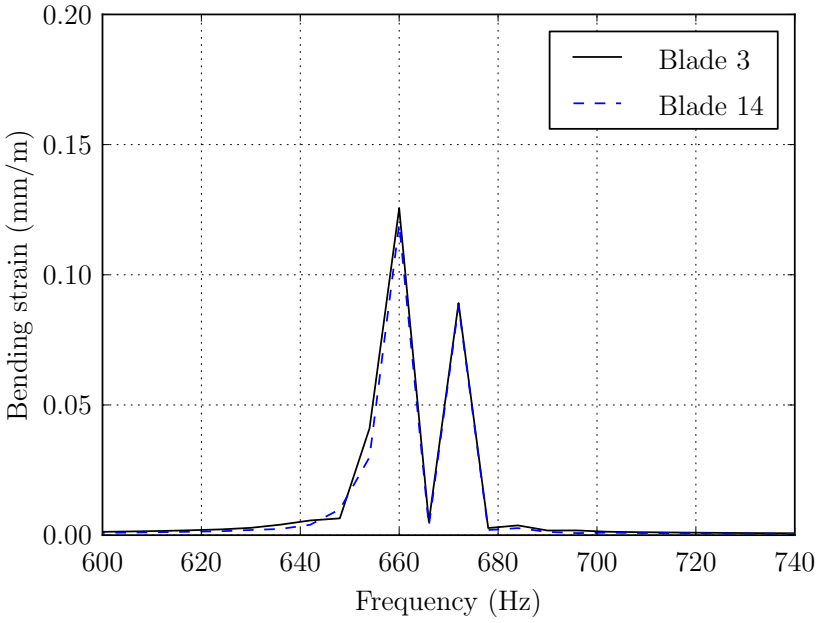

Figure 6.9: FFT of the bending strain calculated by the +2 ND FSI model for blade 3 and blade 14 for an excitation frequency of 660 Hz.

frequency and the nozzle bypass frequency, respectively. The non-zero sample at 654 Hz indicates that the FFT must contain a component at the natural frequency of the first bending mode. These same components were also observed in the tip displacement of each blade in section 6.4.1.

The magnitude of the 660 Hz component of the bending strain, of blade 25 in the actual compressor, was calculated using equation (3.3.3) from the bridge voltage measured by Van der Spuy *et al.* (2012) to be 0.109 mm/m. This value is also presented in appendix B. The magnitudes of the 660 Hz components of the bending strain of the blades in the +2 ND FSI model are therefore all between 10 % and 20 % larger than the magnitude of the 660 Hz computed from the data of Van der Spuy *et al.* (2012). The level of agreement between the bending strain from the +2 ND FSI model and the bending strain from the data of Van der Spuy *et al.* (2012) was considered to be satisfactory.

Chapter 7

Conclusions and recommendations

The goal of the project was to create a FSI model capable of simulating the vibrations of the rotor blades, of the Rofanco compressor, excited by the vibration excitation system. In order to achieve this goal, the objectives listed in section 1.2 had to be attained. All of the objectives of the project were met. The goal of the project was therefore achieved. The chapter begins by summarising the results and conclusions reached in attaining each of the objectives. Recommendations are then provided for future work.

7.1 Quantification of the axial velocity perturbations

Experiments were conducted to quantify the magnitude of the axial velocity perturbations, in the compressor flow field, induced by the vibration excitation system. The transient axial velocity profile, 9.5 mm upstream of the first rotor blade row was measured for a series of different settings of the vibration excitation system. The majority of the axial velocity profiles were measured at an excitation frequency of 650 Hz and a supply pressure of 2.5 bar.

It was observed that, at an excitation frequency of 650 Hz and a supply pressure of 2.5 bar, the axial velocity perturbations are concentrated to the outer third of the span of each blade when the vibration excitation system is fitted with the 32 hole rotors. When the system was fitted with the 16 hole rotors, the axial velocity perturbations were concentrated to the outer half of the blade span. The magnitude of the axial velocity perturbations measured for the 16 hole rotors were larger than the axial velocity perturbations detected for the 32 hole rotors. In both cases, the magnitude of the axial velocity perturbations was not strongly dependent on the ND mode setting applied to the vibration excitation system.

7.2 FE model of the rotor blades

A structural FE model was created of a single rotor blade. The mesh dependence of the single blade FE model was investigated by doing a modal, static, and transient analysis. The modal and static analyses were also used to verify the accuracy of the single blade FE model. The results of the modal analysis were also used to verify that the natural frequency of the first bending mode of the FE model was sufficiently close to the natural frequency of an actual rotor blade. The results of the static analysis confirmed that the FE model reacts to a specific load case in the same manner as an actual rotor blade. The transient analysis was used to determine the time step size required to resolve the motion of the blades.

A pre-stressed modal analysis was performed in order to investigate the increase in stiffness caused by the centrifugal load acting on each rotor blade. The natural frequency of the first bending mode was measured to be 649 Hz when the rotor blade is stationary. The results of the pre-stressed modal analysis revealed that, when the rotor is rotating at 2880 rpm, the resulting centrifugal load causes the natural frequency of the first bending mode to increase to 658 Hz. A similar increase was also observed in the natural frequencies of the higher order modes of the blade.

The 0 ND FE model was created from 3 copies of the single blade FE model. The +2 ND FE model was created from 21 copies of the single blade FE model. The 0 ND FE model and the +2 ND FE model were constructed from the single blade FE model after the mesh refinement study had been completed, and the accuracy of the single blade FE model had been verified.

7.3 CFD model of the rotor blades

The 0 ND CFD model was constructed for the simulation of the 0 ND mode of the vibration excitation system. The 0 ND CFD model contained three blades of the first rotor blade row and a single exciter of the vibration excitation system. Preliminary static and transient analyses were conducted to verify the accuracy of the 0 ND CFD model. A mesh refinement study was also performed during the preliminary analyses.

A transient analysis was performed to derive the sinsoidal velocity components that adequately represent the pulsating nozzle jets in the 0 ND CFD model. Separate sets of velocity components were derived for the scenario where the vibration excitation system has been fitted with the 32 hole rotors and the scenario where the system has been fitted with the 16 hole rotors. The sensitivity of the solution to time step size and the number of iterations per time step was also investigated. Seven copies of the 0 ND CFD model were then used to create the +2 ND CFD model for the simulation of +2 ND mode of the vibration exci-

tation system. The +2 ND CFD model therefore contained 21 blades of the first rotor blade row, and seven of the exciters of the vibration excitation system.

A transient analysis was performed, using the 0 ND CFD model, of the vibration excitation system operating at an excitation frequency of 660 Hz and a supply pressure of 2.5 bar, and in the 0 ND mode. A transient analysis was also performed, using the +2 ND CFD model, of the system functioning at the same excitation frequency and supply pressure, and in the +2 ND mode. The transient analyses were conducted for comparison with the results of the FSI simulations. In both cases, the force perpendicular to the root, acting on each blade in the CFD model, was examined. A FFT was calculated of the force acting on each blade as predicted by the CFD model.

Each FFT of the blade force exhibited two prominent components at the excitation frequency of 660 Hz and the nozzle bypass frequency of 672 Hz. There were also a number of additional components such as the harmonics of the excitation frequency and the nozzle bypass frequency. The magnitudes of the components making up the force perpendicular to the root, calculated by the 0 ND CFD model, were larger for the 16 hole rotors than the 32 hole rotors. This is consistent with the measured axial velocity profiles which showed larger axial velocity perturbations for the 16 hole rotors than the 32 hole rotors. The phase angles of the 660 Hz components of the blades in the 0 ND CFD model, for both the 32 hole rotors and the 16 hole rotors, had the appropriate values required to excite the 0 ND mode. The 660 Hz components of the force perpendicular to the root acting on each of the blades, calculated by the +2 ND CFD model, also had the appropriate phase angles required to excite the +2 ND mode.

7.4 FSI simulations of the rotor blades

The 0 ND FSI model was constructed by coupling the 0 ND CFD model and the 0 FE model. The +2 ND CFD model was coupled to the +2 ND FE model to form the +2 ND FSI model. An analysis was performed using the 0 ND FSI model to determine the effect of the number of stagger iterations per time step on the solution. The results of the analysis showed that the difference between the solution computed using a weak staggered coupling and the solution obtained using a strong staggered coupling was negligible. However, the analysis also revealed that the computation time saved, by using a weak staggered coupling instead of a strong staggered coupling, was significant. A weak staggered coupling was therefore selected for both the 0 ND FSI model and the +2 ND FSI model. FSI simulations were then conducted, using the 0 ND FSI model and the +2 ND FSI model, of the vibration excitation system operating at an excitation frequency of 660 Hz and a supply pressure of 2.5 bar.

7.4.1 Blade forces

A FFT was calculated of the force perpendicular to the root, acting on each blade in the first rotor blade row, predicted by the 0 ND FSI model and the +2 ND FSI model. As observed from the results of the transient CFD simulations, the force acting on each blade exhibited a component at the excitation frequency, as well as a number of additional components. The additional components included the nozzle bypass frequency, and the harmonics of the components at the excitation frequency and the nozzle bypass frequency. The magnitude of the 660 Hz component of the blade force predicted by each FSI model was close to the value predicted by the corresponding CFD model during the transient CFD simulations. The magnitude of the 660 Hz component calculated by the 0 ND FSI model was approximately 5 % smaller than the magnitude of the 660 Hz component obtained from the 0 ND CFD model during the transient CFD analysis. The magnitude of the 660 Hz component calculated by the +2 ND FSI model was only 7 % smaller than 660 Hz component obtained from the +2 ND CFD model during the transient CFD analysis.

The close correlation between the blade forces predicted by each FSI model and the corresponding CFD model suggests that the amplitude of the motions of the blades have a negligible effect on the force acting on each blade. A transient CFD analysis of the vibration excitation system should therefore be sufficient for predicting the force acting on each blade. It should also be possible to accurately compute the motions of the blades using a one-way FSI model.

7.4.2 Displacements and strains

A FFT was calculated of the tip displacement of each blade, in the direction perpendicular to the root, predicted by the 0 ND FSI model. A FFT was also computed of the tip displacement perpendicular to the root obtained for each blade using the +2 ND FSI model. Each FFT showed two prominent components at the excitation frequency and the nozzle bypass frequency. The tip displacement also showed evidence of a component at the natural frequency of the first bending mode. However, the FFT of the tip displacement did not show any of the harmonics of the excitation frequency or the nozzle bypass frequency that were exhibited by the blade force. It was concluded that the harmonics were not present in the tip displacement as the frequencies of the harmonics are too far from the natural frequency of the first bending mode. The magnitude of the 660 Hz component, computed using the 0 ND FSI model, was larger for the 16 hole rotors than the 32 hole rotors. This is consistent with the 660 Hz component of the blade force which was also observed to be larger for the 16 hole rotors than the 32 hole rotors.

The magnitudes of the 660 Hz components calculated for the blades by the 0 ND FSI model, for the 32 hole rotors, were all within 6 % of the magnitude of the 660 Hz component estimated by Van der Spuy *et al.* (2012) for the 0 ND

mode. The magnitudes of the 660 Hz component of the blades in the +2 ND FSI model, computed for the 32 hole rotors, were also all within 6 % of the amplitude of the 660 Hz component estimated by Van der Spuy *et al.* (2012) for the +2 ND mode. The phase angles of the 660 Hz components of the tip displacement of the blades in the 0 ND FSI model differed from the values required for the blades to be vibrating in the 0 ND mode by less than 5°. This was the case for both the tip displacement calculated for the 32 hole rotors and the tip displacement calculated for the 16 hole rotors. The phase angles of the 660 Hz component of each of the blades in the +2 ND FSI model were all within 2° of the values required for vibration in the +2 ND mode.

The bending strains predicted by each of the FSI models was also compared to the bending strain calculated from the vibration data of Van der Spuy *et al.* (2012). A FFT was computed from the bending strain predicted for each blade by the 0 ND FSI model and the +2 ND FSI model. The magnitudes of the 660 Hz components of the bending strain of the blades in the 0 ND FSI model were all between 10 % and 20 % larger than the magnitude of the 660 Hz component calculated from the data of Van der Spuy *et al.* (2012) for the 0 ND mode. This was true for both the bending strain calculated for the 32 hole rotors and bending strain calculated for the 16 hole rotors. The 660 Hz component of the blades in the +2 ND FSI model were also all between 10 % and 20 % larger than the 660 Hz component computed from the data of Van der Spuy *et al.* (2012) for the +2 ND mode.

The amplitude of the component of the tip displacement perpendicular to the root at the excitation frequency, predicted for each blade by both the 0 ND FSI model and the +2 ND FSI model, correlated sufficiently well with the data of Van der Spuy *et al.* (2012). The agreement between the amplitude of the component of the bending strain at the excitation frequency, computed for each blade by both the 0 ND FSI model and the +2 ND FSI model, and the data of Van der Spuy *et al.* (2012) was also satisfactory. Both the 0 ND FSI model and the +2 ND FSI model were therefore considered capable of reproducing the operation of the vibration excitation system and the resulting motions of the blades with sufficient accuracy. The goal of the project has therefore been achieved. Furthermore, the results of the FSI models showed that the pulsating nozzle jets of the vibration excitation system should be capable of exciting the first rotor blade row at or near an excitation frequency of 660 Hz, and in either the 0 ND mode or the +2 ND mode.

7.5 Recommendations for future work

It has already been confirmed that the 0 ND FSI model is capable of replicating the operation of the vibration excitation system when set to the 0 ND mode, an excitation frequency of or near 660 Hz, and a supply pressure of 2.5 bar. It was also confirmed that seven copies of the 0 ND FSI model can be combined to

form the +2 ND FSI model which is capable of simulating the behaviour of the system when set to the +2 ND mode, and the same excitation mode and supply pressure. However, the vibration excitation system is also capable of operating in the +1 ND, +3 ND, -1 ND, -2 ND, and -3 ND modes. It should be possible to simulate these additional ND modes by combining multiple copies of the 0 ND FSI model.

In order to simulate the +1 ND mode and the +3 ND mode, the blade pitch of the 0 ND FSI model can be adjusted so that it contains 1 of 15 exciters, and 3 blades of a rotor blade row consisting of 45 blades. Fifteen copies of the 0 ND FSI can then be combined for the simulation of the +1 ND mode. Five copies of the 0 ND FSI model can be combined for the simulation of the +3 ND mode. The same FSI models used to simulate the positive ND modes can also be used to simulate the negative ND modes. The difference in phase in the exciter nozzles must just be set so that the travelling wave propagates around the rotor against the direction of rotation.

The FSI model is only capable of simulating the operation of the vibration excitation system for an excitation frequency at or near 660 Hz and a supply pressure of 2.5 bar. However, the vibration excitation system is designed to excite the blades at a number of different frequencies, and using a number of different supply pressures. Deriving a new set of velocity components each time a different setting of the vibration excitation system is to be simulated is time consuming. A more convenient solution may be to derive a mathematical model from experimental data which can be used to simply calculate the velocity components that adequately represent the nozzle jets for any particular setting.

The results of the 0 ND FSI model and the +2 ND FSI model showed that a two-way staggered FSI model may not be necessary to accurately recreate the operation of the vibration excitation system during future simulations. A transient CFD model should be adequate for calculating the aerodynamic forces acting on each of the blades in the first rotor blade row. The use of a one-way staggered FSI model may also be sufficient for calculating the vibrations of the rotor blades. Both the transient CFD model and the one-way staggered FSI model avoid the problems associated with mesh folding which are present in the two-way staggered FSI model.

Appendix A

Details of strain gauge assemblies

A.1 Technical details

The strain gauges attached to the blades were Vishay Micro Measurements SR-4 General Purpose Strain Gauges (Raubenheimer, 2011). A photograph of one of the strain gauges is provided in figure A.1. The relevant technical details of each strain gauge assembly, as reported by Raubenheimer (2011), are provided below:

- Grid resistance = $120 \pm 0.3\ \Omega$
- Gauge factor at 24 °C = 2.035 ± 0.011
- Temperature coefficient of gauge factor = $1.2 \pm 0.2\ \%/100\ °C$
- Transverse sensitivity = 1.2 ± 0.2
- Bridge excitation voltage = 5 V

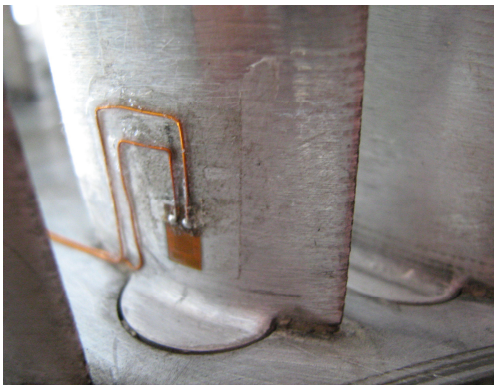

Figure A.1: Photograph of one of the strain gauges (Raubenheimer, 2011).

A.2 Locations on blade surface

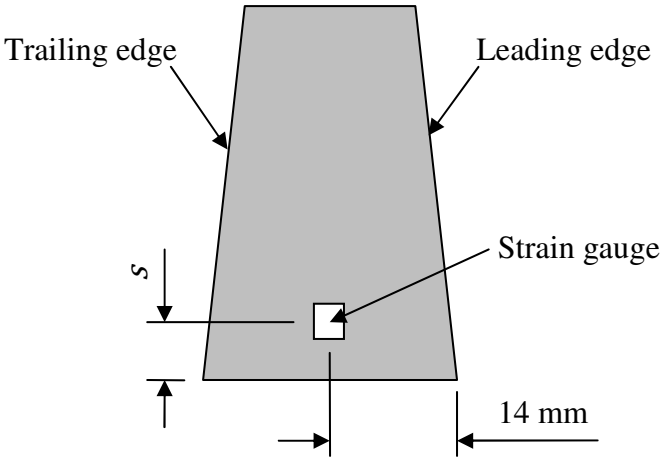

s = 4.5 mm for blade 3
s = 6.1 mm for blade 25

(a) Pressure side

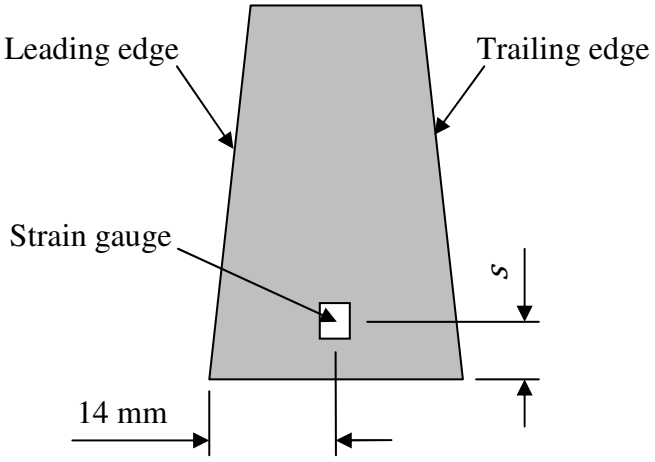

s = 4.5 mm for blade 3
s = 6.1 mm for blade 25

(b) Suction side

Figure A.2: Location of each strain gauge on the blade surface.

Appendix B

Vibration data

This appendix contains a portion of the vibration data collected by Van der Spuy *et al.* (2012), on the Rofanco compressor test bench, with the compressor set to a rotation speed of 2880 rpm. The data presented here was used in the estimation of the blade force in chapter 5. The data was also used to verify the results of the FE simulations in chapter 4, and the FSI simulations in chapter 6. The data collected with the vibration excitation system set to an excitation frequency of 650 Hz, a supply pressure of 2.5 bar, and the 0 ND excitation mode are presented first. This is followed by the data collected at the same excitation frequency and supply pressure, but with the system set to the +2 ND excitation mode instead.

B.1 Data for the 0 ND mode

Van der Spuy *et al.* (2012) used equation (3.3.2b) to estimate the tip displacement perpendicular to the root of blade 25, as a function of time, from the measured bridge voltage. A FFT was calculated from the estimated tip displacement perpendicular to the root and is plotted in figure B.1. The most prominent component in figure B.1 occurs at the excitation frequency of 660 Hz. This component has a magnitude of 0.089 mm. The second most prominent component exists near 720 Hz. This component is the nozzle bypass frequency (15×48 Hz $=$ 720 Hz). The FFT also shows peaks at other multiples of the rotation speed. Finally, the FFT also shows a broad minor peak near 653 Hz. This component is the response at the natural frequency of the first bending mode. The natural frequency of the blade, observed in figure B.1, is slightly higher than the value of 649 Hz measured for blade 25 with the rotor blades stationary. This increase in the natural frequency is caused by the centrifugal loads acting on the rotor blades.

Equation (3.3.3) was used to compute the bending strain, detected by the pressure side strain gauge of blade 25, from the bridge voltages measured. The FFT of the bending strain is plotted in figure B.2. Since both the bending strain

and the tip displacement are determined from the bridge voltage, the FFT in figure B.2 shows the same components that are visible in figure B.1. The magnitude of the 660 Hz component was 0.093 mm/m.

B.2 Data for the +2 ND mode

A FFT was calculated of the tip displacement perpendicular to the root of blade 25, estimated by Van der Spuy *et al.* (2012) from the bridge voltage for the +2 ND mode, and is plotted in figure B.3. The tip displacement was again estimated by Van der Spuy *et al.* (2012) using equation (3.3.2b). The FFT of the tip displacement perpendicular to the root is presented in figure B.3. As with the 0 ND mode, the FFT shows peaks near 653 Hz, 660 Hz, and 672 Hz. These components again occur at the natural frequency of the first bending mode, the excitation frequency, and the nozzle bypass frequency, respectively. It also shows peaks at multiples of the rotation speed other than the nozzle bypass frequency. The magnitude of the 660 Hz component is 0.105 mm.

Equation (3.3.3) was again used to calculate the bending strain, measured by the pressure side strain gauge of blade 25, from the bridge voltage. The FFT of the bending strain obtained for the +2 ND mode is plotted in figure B.4. The FFT of the bending strain in figure B.4 again showed exactly the same peaks that are visible in figure B.3. The magnitude of the component at 660 Hz is 0.109 mm/m.

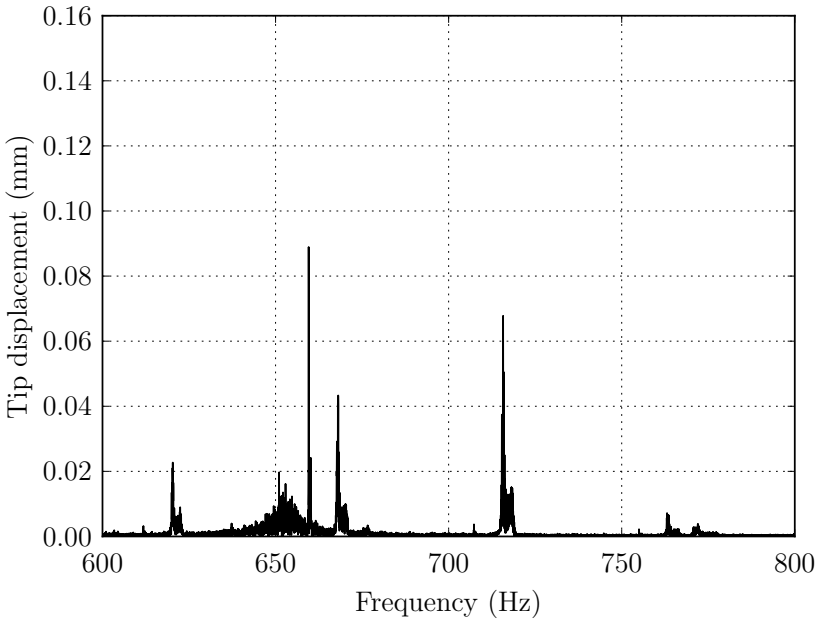

Figure B.1: FFT of the tip displacement perpendicular to the root estimated by Van der Spuy *et al.* (2012) for blade 25 from the bridge voltage measured for the 0 ND mode.

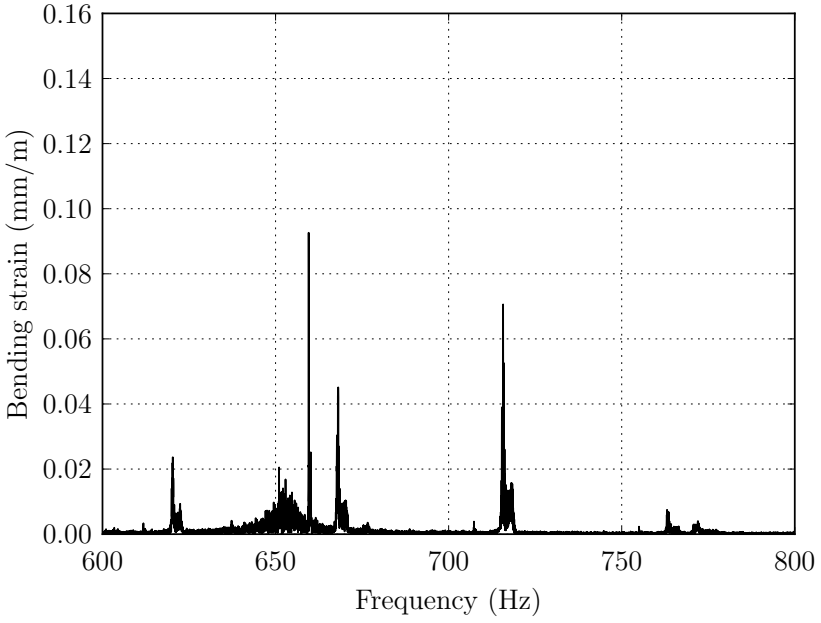

Figure B.2: FFT of the bending strain calculated for blade 25 from the bridge voltage measured by Van der Spuy *et al.* (2012) for the 0 ND mode.

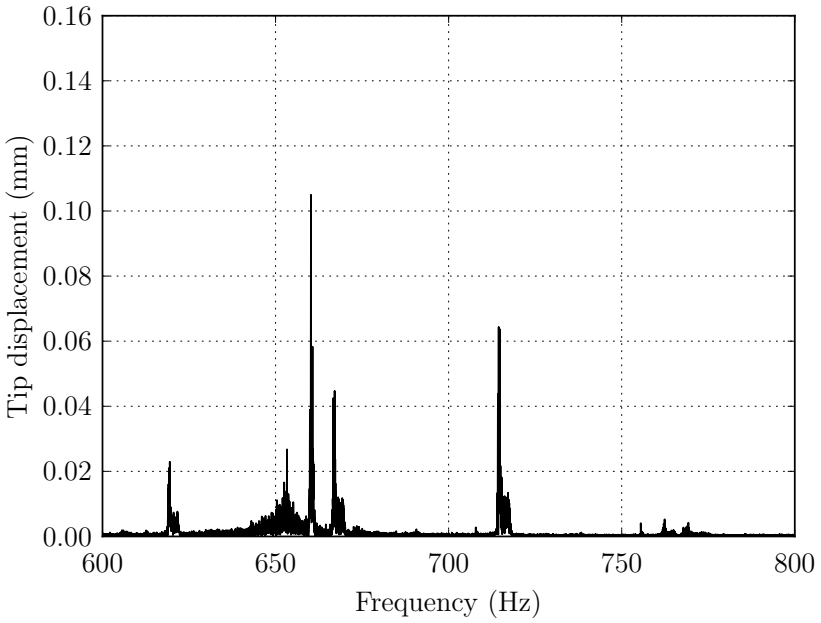

Figure B.3: FFT of the tip displacement perpendicular to the root estimated by Van der Spuy *et al.* (2012) for blade 25 from the bridge voltage measured for the +2 ND mode.

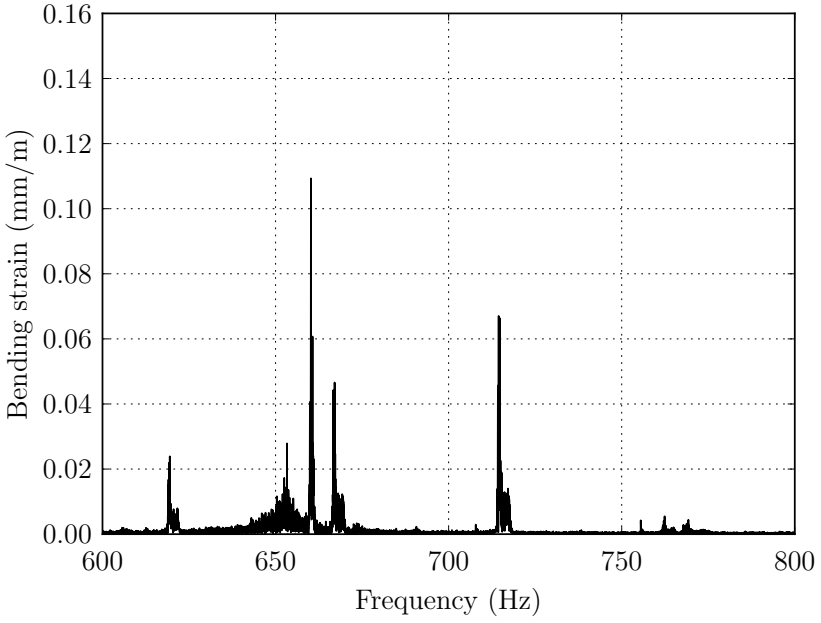

Figure B.4: FFT of the bending strain calculated for blade 25 from the bridge voltage measured by Van der Spuy *et al.* (2012) for the +2 ND mode.

Appendix C

Undisturbed velocity profiles

The undisturbed axial velocity profiles measured are plotted in figure C.1 and figure C.2 for the 32 hole rotors and 16 hole rotors, respectively. The profiles are plotted together with the axial velocity profile measured by Gill (2012) at a similar mass flow rate and compressor rotation speed. The profile of Gill (2012) was measured at a mass flow rate of at 2.51 kg/s and a rotation speed of 2900 rpm. The profile of Gill (2012) shows a dip in the axial velocity near a radius of 180 mm. The velocity profiles obtained for both the 32 hole and 16 hole rotors show the same dip in axial velocity at this radius.

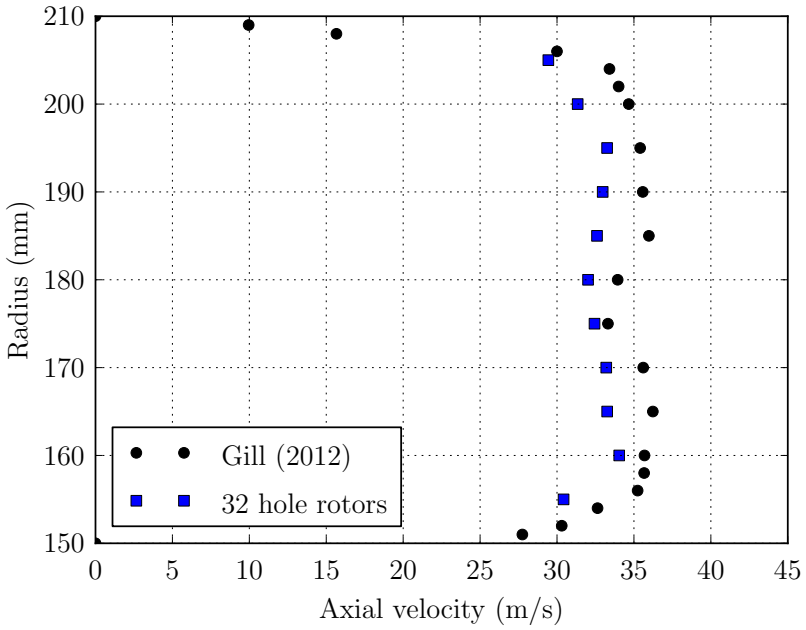

Figure C.1: Undisturbed axial velocity profile measured for the 32 hole rotors.

A significant difference between the 16 hole profile and the profile from Gill (2012) is visible at a radius of 205 mm. The 16 hole profile shows a sudden increase in axial velocity at this radius. It is possible that the nozzle upstream of the x-probe

may have been protruding slightly into the flow path of the compressor. Such a protrusion could produce disturbances downstream of the nozzle that interfere with the axial velocity measurements. Despite this discrepancy, the correlation between the profile of Gill (2012) and the profile measured for the 16 hole rotors was still deemed to be acceptable. The correlation between the profile of Gill (2012) and the axial velocity profile measured for the 32 hole rotors was also considered to be acceptable.

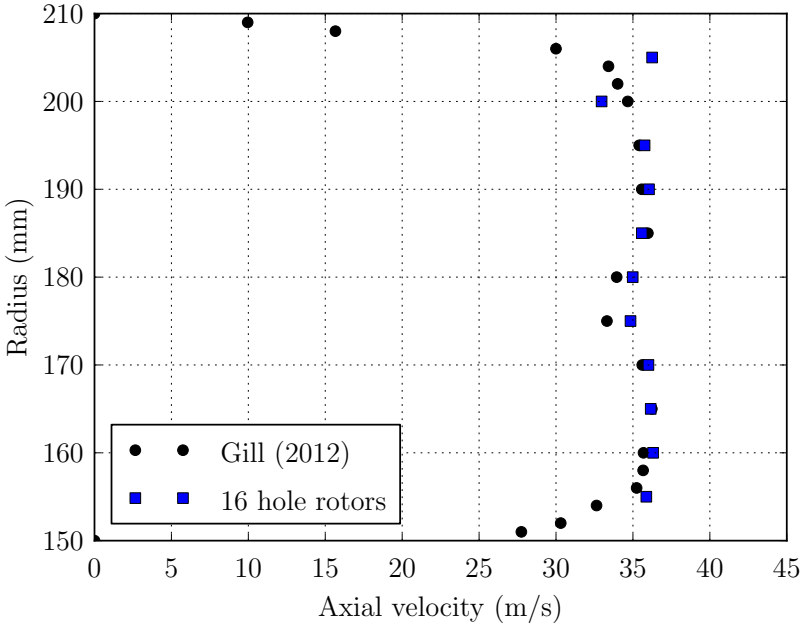

Figure C.2: Undisturbed axial velocity profile measured for the 16 hole rotors.

Appendix D

Mesh refinement study: FE model

D.1 Modal analysis

The modal analysis in section 4.3.1 was repeated for the coarse and medium meshes. The natural frequencies obtained for the first six modes are summarised in table D.1. The coarse mesh and the medium mesh predicted values of 644.32 Hz and 648.29 Hz for the natural frequency of the first bending mode, respectively. These values are only 0.8 % and 0.2 % lower, respectively, than the value of 649.35 Hz obtained using the fine mesh. The natural frequencies predicted by the three meshes for each of the five higher order modes were also all close in value. The first four mode shapes obtained using the fine mesh are presented in figure 4.2. The first four mode shapes obtained using the coarse and medium meshes are not provided here. However, it was found that the mode shapes obtained using the coarse and medium meshes were almost identical to those obtained using the fine mesh. The mode shapes and natural frequencies obtained using each of the three meshes were therefore all deemed mesh independent.

Table D.1: Natural frequencies of the first six modes computed using the coarse, medium and fine meshes.

	Coarse	Medium	Fine
Mode 1	644.32	648.29	649.35
Mode 2	2864.8	2882.5	2886.6
Mode 3	3500.1	3509.3	3512.1
Mode 4	5548.7	5550.3	5548.4
Mode 5	8569.2	8592.7	8597.5
Mode 6	10077	10052	10047

D.2 Static FE analysis

The coarse and medium meshes were used to repeat the nonlinear static analysis in section 4.3.2. The tip displacement calculated using the coarse, medium, and fine meshes is plotted as a function of time in figure D.1. The tip displacement shown in figure D.1 is the component perpendicular to the blade root. All three meshes predict that the tip displacement is linearly proportional to the applied load. The tip displacement predicted by the coarse mesh is approximately 2.5 % larger than the value predicted by the fine mesh for each load case. The tip displacement predicted by the medium mesh, for each load case, is only 0.5 % larger than the corresponding value predicted using the fine mesh. The tip displacements predicted by each of the three meshes are therefore all close in value.

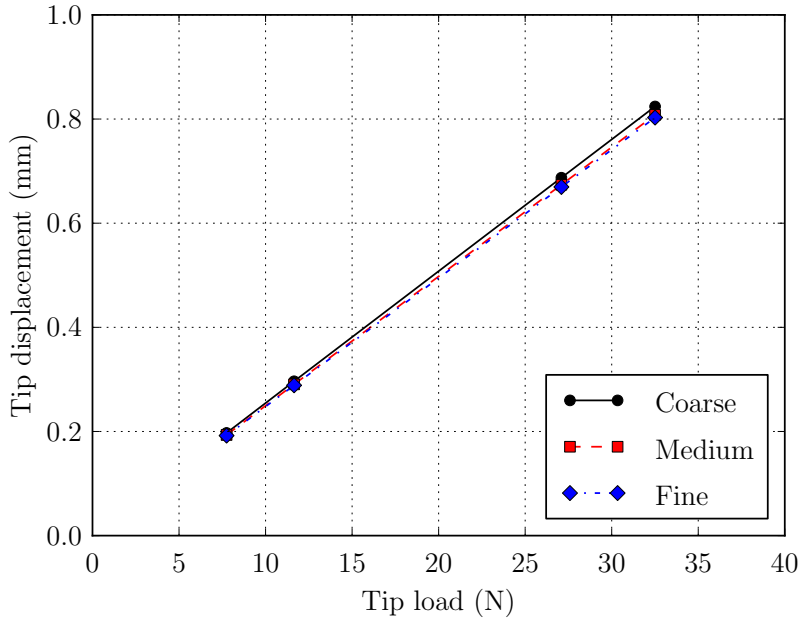

Figure D.1: Tip displacement perpendicular to the root plotted as a function of tip load for the coarse, medium, and fine meshes.

The bending strain computed by the FE model, at the location of the pressure side strain gauge, was plotted as a function of load in figure 4.4 for the fine mesh. The relationship between the bending strain and the applied load predicted using the coarse and medium meshes were both almost identical to that obtained using the fine mesh. Both the displacement fields and the bending strain fields obtained using the three meshes were therefore all concluded to be mesh independent.

D.3 Transient FE analysis

The transient analysis in section 4.5 was carried out again using the coarse and medium meshes. The solver was set to simulate the motion of the blade for 400 time steps. The time step size used in each case was 5.4945×10^{-5} s. The computation time required to simulate the motion of the blade are provided in table D.2 for the coarse, medium, and fine meshes. The computation times are provided here as they are referred to and discussed in section 4.6.

Table D.2: Computation times recorded for the coarse, medium and fine meshes.

	Computation time (s)		
	Coarse	Medium	Fine
Total time	194	677	2189
Per time step	0.485	1.69	5.47

The tip deflection perpendicular to the root of the blade is plotted in figure D.2 as a function of time for the coarse, medium, and fine meshes. All three meshes predict an amplitude of vibration of 0.05 mm. Figure D.2 shows that the curves obtained using the medium and fine meshes are coincident for the entire duration simulated. As time increases, the curve obtained using the coarse mesh begins to lag slightly behind the curves obtained using the medium and the fine meshes. This indicates that the coarse mesh predicts a slightly lower frequency of vibration than the medium, and the fine meshes. However, since this difference in the frequency of vibration was small, the solutions obtained using the coarse, medium and fine meshes were all still deemed mesh independent.

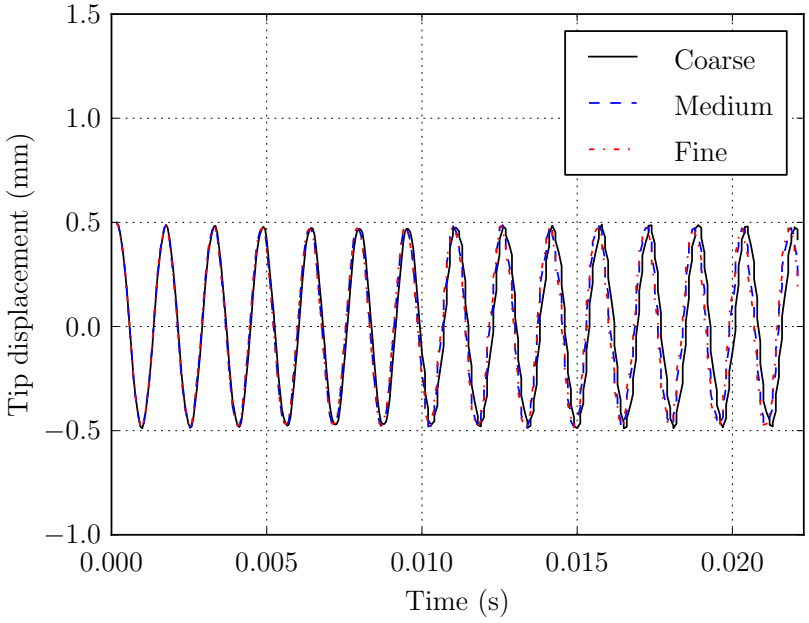

Figure D.2: Tip displacement perpendicular to the root plotted as a function of time for the coarse, medium, and fine meshes.

Appendix E

Preliminary steady state CFD analysis

E.1 Settings and boundary conditions

The rotation speed of the reference frame of the mesh block downstream of the interface was set equal to 2900 rpm. This is the compressor rotation speed used by Gill (2012). The rotation speed of the hub downstream of the interface was also set to 2900 rpm. The reference pressure for the domain was set to 98000 Pa. As mentioned in section 5.2, a pressure of 98000 Pa is a typical value for the atmospheric pressure in the laboratory where the Rofanco compressor is located. The mass flow rates simulated were 1.41 kg/s, 2.86 kg/s, and 2.56 kg/s. At a rotation speed of 2900 rpm, these values correspond to near design, higher than design, and stall mass flow rates, respectively.

Depending on the mass flow rate being simulated, the axial velocity components on the inlet boundary were set equal to the appropriate axial velocity profile measured by Gill (2012). The axial velocity profiles measured by Gill (2012) for each mass flow rate are plotted in figure E.1. The boundary condition at the outlet of the domain was set to radial equilibrium. The relative static pressure at a radius of 180 mm was set equal to the particular value measured by Gill (2012) for the mass flow rate being simulated. This value was -71.5 Pa, -676 Pa, and -1100 Pa for the stall, design, and higher than design mass flow rates, respectively.

The solver was set to run for 600 iterations. The Ansys CFX-Solver Modeling Guide (2012*b*) states that simulations are generally converged when the RMS and maximum residual are below 1×10^{-5} and 1×10^{-4}, respectively. As an additional check for convergence, the net mass flow rate into the domain was also monitored for each iteration. Conservation of mass dictates that the net mass flow rate into the domain should be close to zero when the solution has converged. The solution was deemed to be converged after 600 iterations when two sets of criteria had been met. The first set of criteria was that the RMS and maximum residual had to meet the targets suggested in the Ansys CFX-Solver

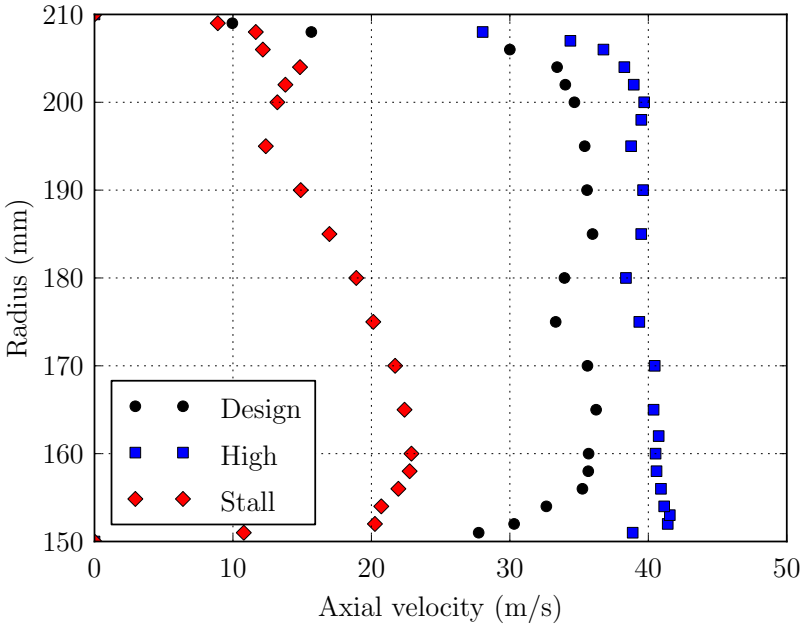

Figure E.1: Axial velocity profiles measured by Gill (2012) for the design, higher than design and stall mass flow rates.

Modeling Guide (2012*b*). The second criteria was that the magnitude of the net mass flow rate into the domain had to be less than 0.0001 kg/s.

E.2 Results

Contours of y^+ are plotted on the blade surfaces in figure E.2 for the coarse mesh and figure E.3 for the fine mesh. Only the contours of y^+ for the coarse and fine meshes are provided here as these featured the highest and lowest y^+ values, respectively. The Ansys CFX-Solver Modeling Guide (2012*b*) recommends a y^+ of approximately 1 for the optimal performance of the $k-\omega$ SST turbulence model. The y^+ values are below or close to this threshold over most of the blade surfaces, the hub and the shroud when using the fine mesh. The average y^+ values obtained on the blade surfaces, hub and shroud were 2 and 5 for the coarse mesh and the medium mesh, respectively. The y^+ values obtained using both the coarse mesh and the medium mesh were therefore larger than the y^+ of 1 recommended by the Ansys CFX-Solver Modeling Guide (2012*b*). However, this had a negligible effect on the results obtained.

The pressure ratios computed for each mass flow rate, using the coarse, medium, and fine meshes, are shown in table E.1. The pressure ratios provided are the ratio between the static pressure downstream and upstream of the first rotor blade row. Also shown in table E.1 are the pressure ratios measured by Gill (2012) for the three mass flow rates. The pressure ratios predicted by the three meshes for the near design mass flow rate were all identical. This was also

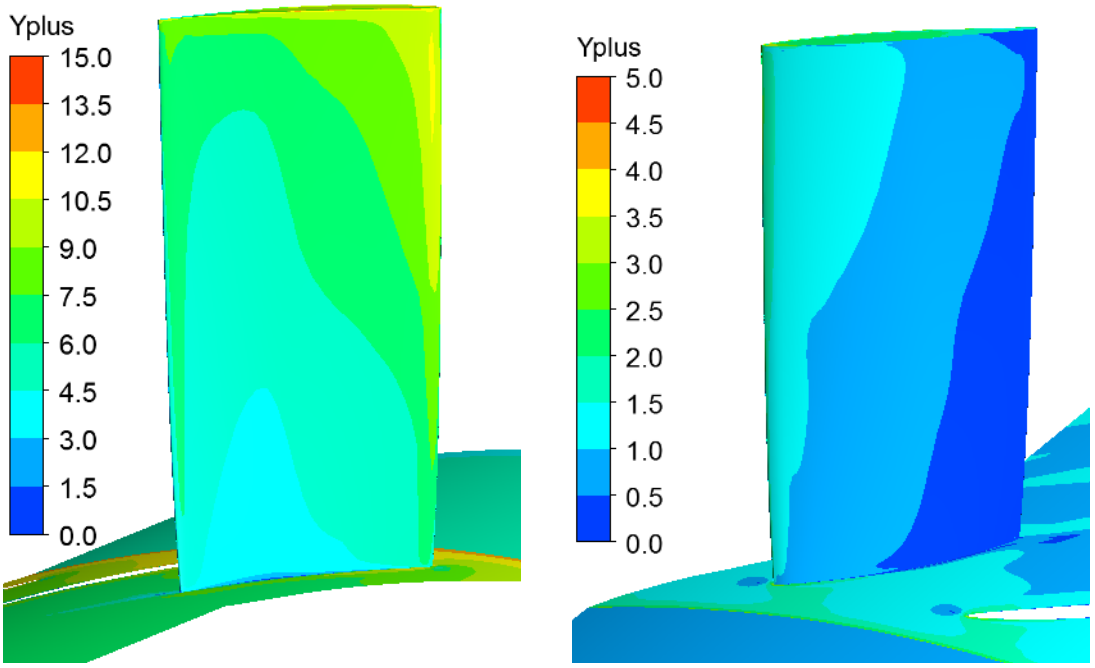

(a) Pressure side (b) Suction side.

Figure E.2: Contours of y^+ obtained using the coarse mesh.

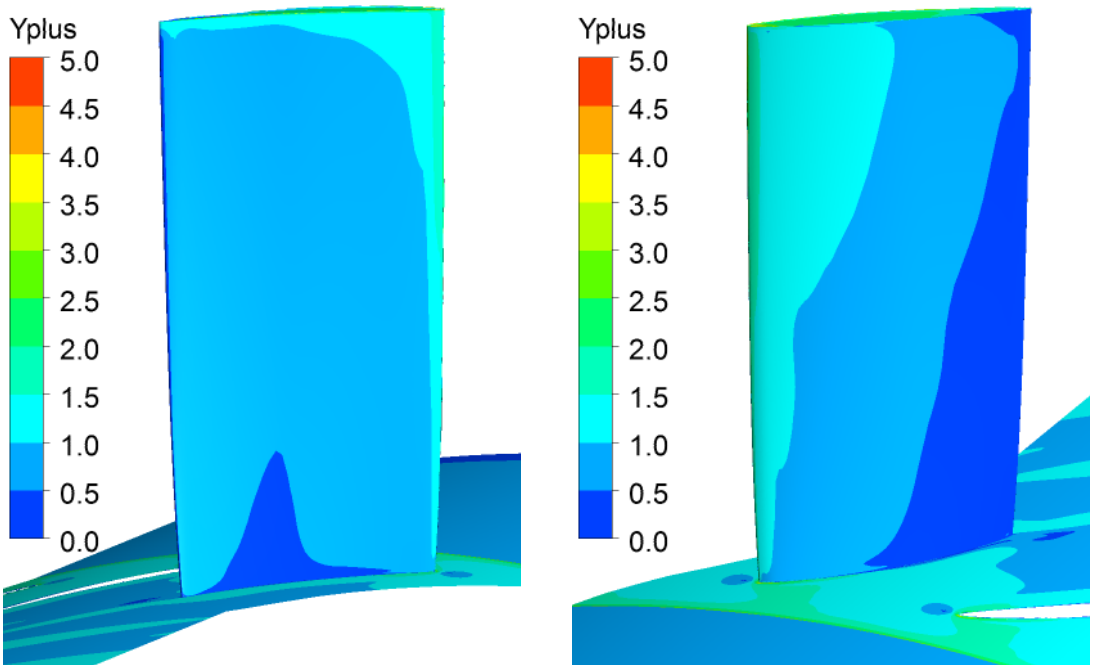

(a) Pressure side (b) Suction side.

Figure E.3: Contours of y^+ obtained using the fine mesh.

the case for the pressure ratios obtained for the higher than design mass flow rate. The pressure ratios calculated for the stall mass flow rate were identical for the medium and fine meshes. The pressure ratio calculated using the coarse mesh for the stall mass flow rate was similar to the pressure ratios computed using the medium and fine meshes. The pressure ratios therefore suggest that all three meshes yield steady state solutions that are mesh independent. The mesh independence of the solutions was confirmed when the velocity profiles at the outlet boundary of the domain was examined. As with the pressure ratios, the velocity profiles obtained using the three meshes for a specific mass flow rate were all almost identical.

For the near design mass flow rate, the pressure ratios predicted by the three meshes were all close to the pressure ratio measured by Gill (2012). The difference between the computed pressure ratios and the measured pressure ratio was somewhat larger for the higher than design mass flow rate. However, the correlation between the pressure ratio predicted by each mesh for the higher than design mass flow rate and the pressure ratio measured by Gill (2012) was still deemed acceptable. The velocity profiles at the outlet boundary, obtained for both the near design and the higher than design mass flow rates, also agreed sufficiently well with the velocity profiles measured by Gill (2012) downstream of the first rotor blade row.

The results computed by the 0 ND CFD model for the near stall flow rate did not agree with data of Gill (2012) at all. This was the case for both the pressure ratio, and the velocity profile at the outlet boundary of the domain. A possible explanation for this discrepancy is that the compressor flow field is highly transient at this mass flow rate. It is therefore unlikely that accurate results for this flow rate could be obtained by conducting a steady state analysis.

Table E.1: Static-to-static pressure ratios measured by Gill (2012), and calculated using the coarse, medium and fine meshes.

	Gill (2012)	Coarse	Medium	Fine
Design	1.0087	1.0084	1.0084	1.0084
High	1.0069	1.0059	1.0059	1.0059
Stall	1.0081	1.0020	1.0023	1.0023

Appendix F

Preliminary transient CFD analysis

F.1 Boundary conditions and initial conditions

The reference pressure, rotation speed, and boundary conditions applied to the 0 ND CFD model are identical to those used by Raubenheimer (2011) for the simulations of the prototype excitation system. The reference pressure for the domain was set to 101.3 kPa. The reference frame of the mesh block downstream of the interface was set as rotating at 3000 rpm. The rotation speed of the hub downstream of the interface was also specified to be 3000 rpm. The relative static pressure at a radius of 180 mm was set to -1211 Pa for the radial equilibrium boundary condition at the outlet of the domain.

Steady state analyses were first conducted using the coarse, medium, and fine meshes. The steady state solution obtained for each mesh was used as the initial conditions for the transient analysis performed using that mesh. The axial velocity components at both the inlet and patch boundaries were set equal to the inlet axial velocity profile used by Raubenheimer (2011). The axial velocity profile of Raubenheimer (2011) is plotted in figure F.1. The radial and tangential velocity components at both the inlet and patch boundaries were set equal to zero.

Once the steady state analyses were complete, a transient analysis was performed for each mesh. The axial and radial velocity components at the patch boundary were then set to equations (F.1.1a) and (F.1.1b), respectively for each transient analysis. The tangential velocity components at the patch boundary were set equal to zero. Equations (F.1.1a) and (F.1.1b) were used by Raubenheimer (2011) to represent the nozzle jet of each prototype exciter. Equations (F.1.1a) and (F.1.1b) cause the velocity vectors at the patch boundary to be orientated at a constant angle of 20 °C with respect to the compressor shroud. The magnitude of the velocity vectors at the patch boundary vary as a sinusoidal function of time between 150 m/s and 208 m/s. The pulsation frequency of the jet created is 1200 Hz.

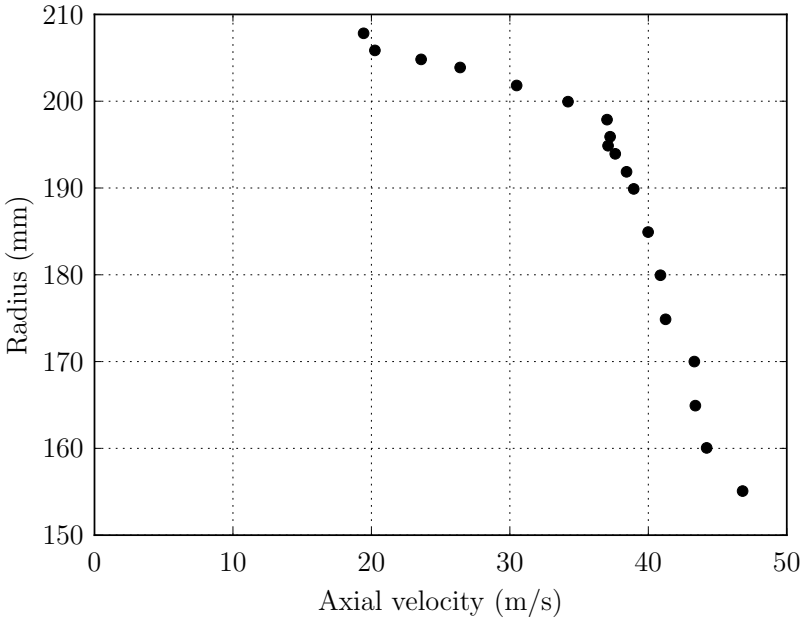

Figure F.1: Inlet axial velocity profile measured by Raubenheimer (2011).

$$V_r = -61.22 - 9.919\sin(2\pi 1200t) \tag{F.1.1a}$$

$$V_z = 168.2 + 27.25\sin(2\pi 1200t) \tag{F.1.1b}$$

F.2 Results of transient simulations

The integration time step selected was 5.5555×10^{-5} s. This is the same time step size used by Raubenheimer (2011) for the simulations of the prototype excitation system. A time step size 5.5555×10^{-5} s results in there being 360 time steps per each rotation of the compressor rotor. The number of iterations per time step was set equal to 10 iterations. The duration of the simulation was set to 0.03 s. This duration corresponds to one and a half rotations of the rotor.

The force perpendicular to the root, acting on blade 2 in the 0 ND CFD model, is plotted as a function of time in figure F.2 for the coarse, medium, and fine meshes. The force acting perpendicular to the root, obtained for each of the three meshes, settles into a repetitive steady state pattern after 0.0025 s. The curves obtained using the medium and fine meshes are coincident for the entire duration of the simulation. The amplitude of the force perpendicular to the root predicted by the coarse mesh is visibly larger than the amplitudes predicted using the medium and fine meshes. Unlike the solutions obtained using the medium and fine meshes, the solution obtained using the coarse mesh is therefore not completely mesh independent.

A FFT was computed of the force perpendicular to the root obtained for each mesh. A time step of 5.5555×10^{-5} s means that the samples in the time domain

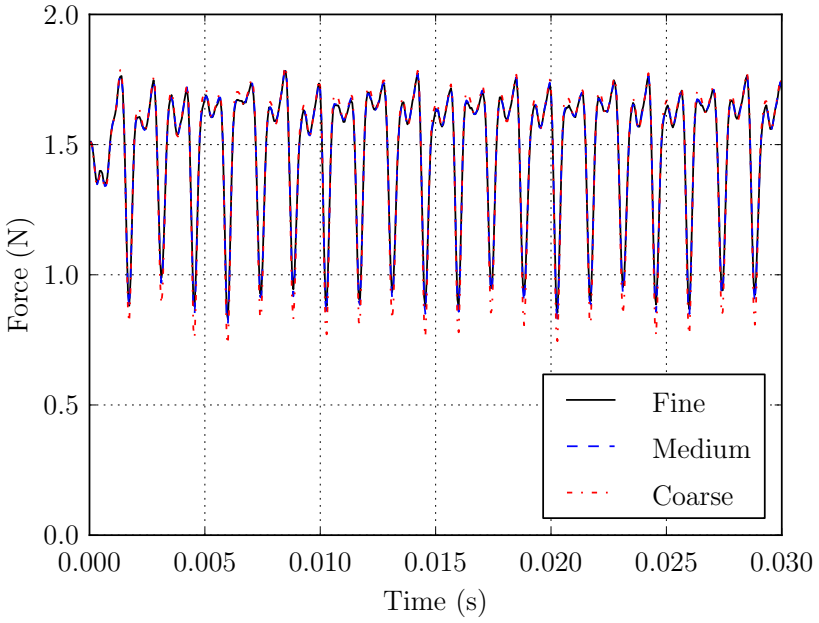

Figure F.2: Force perpendicular to the root calculated for blade 2 using the coarse, medium and fine meshes.

occur at a frequency of 18000 Hz. The FFT was computed using 360 samples from the time domain. The samples were selected from the portion of the time domain after the force perpendicular to the root had settled into a steady state pattern. This resulted in an FFT containing 181 samples in the frequency domain that are spaced at 50 Hz intervals from 0 Hz to 9000 Hz.

The FFT of the force perpendicular to the root, acting on blade 2, is provided in figure F.3 for the coarse, medium, and fine meshes. The FFTs computed for the three meshes all exhibit peaks at 700 Hz, 1200 Hz, and 1400 Hz. The peak at 700 Hz is the component at the nozzle bypass (14×50 Hz $= 700$ Hz). The peak at 1400 Hz is a harmonic of the component at the nozzle bypass frequency. The component at 1200 Hz represents the excitation force induced by the pulsating nozzle jets.

The FFT obtained for each mesh confirmed the observations made from the results in the time domain. The FFT obtained using the medium mesh and the FFT obtained using the fine mesh were almost identical. The FFT obtained for the coarse mesh predicts a larger amplitude for the components at 700 Hz and 1400 Hz than is predicted by the medium and fine meshes. The FFTs therefore again indicated that the solution computed using the medium mesh and the solution computed using the fine mesh are both mesh independent. However, the solution obtained using the coarse mesh is not quite mesh independent.

Figure F.3 shows that the component at 1200 Hz is barely detectable. This was also observed by Raubenheimer (2011) during the simulations of the prototype excitation system. The amplitudes computed by Raubenheimer (2011) for the 700 Hz and 1400 Hz components were 0.256 N and 0.221 N respectively.

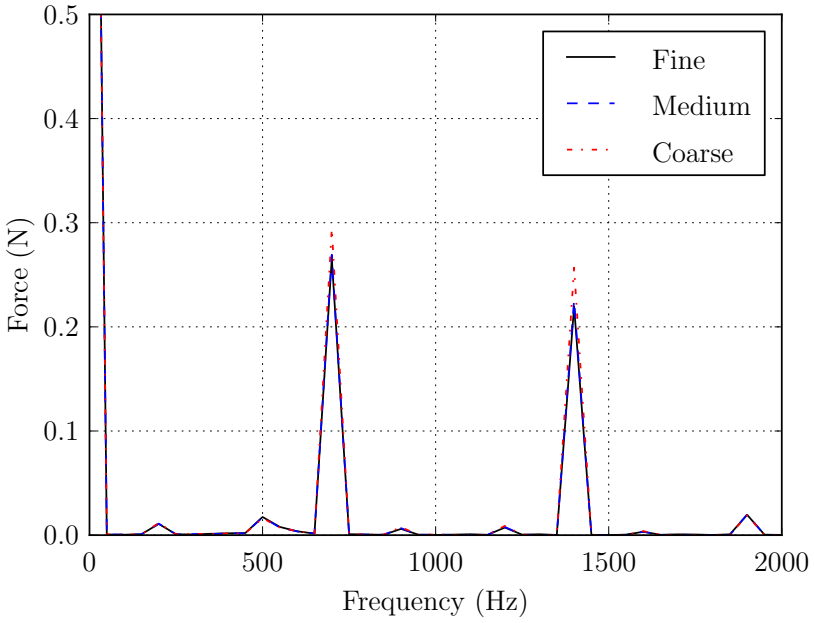

Figure F.3: FFT of the force perpendicular to the root calculated for blade 2 using the coarse, medium and fine meshes.

The amplitudes of the components at 700 Hz and 1400 Hz, calculated using the medium and fine meshes for each blade, were respectively 4 % and 0.5 % larger than the values computed by Raubenheimer (2011).

Raubenheimer (2011) used the Spalart-Almaras turbulence model for the simulations of the prototype vibration excitation system. The turbulence model used for the 0 ND CFD model was the $k - \omega$ SST model. Raubenheimer (2011) also used the software package Numeca/Fine Turbo whereas Ansys CFX was used to create the 0 ND CFD model. Taking into account these differences, the correlation between the solution of Raubenheimer (2011), and the solutions obtained using the medium and fine meshes was deemed satisfactory. Even though the solution obtained using the coarse mesh was not completely mesh independent, it was still considered a reasonable approximation of the aerodynamic forces acting on each of the blades.

Appendix G

Estimation of blade forces

A method was devised for estimating the amplitude of the component of the force perpendicular to the root existing at the excitation frequency. The method estimates the amplitude of the component at the excitation frequency from the bridge voltage of the strain gauge assembly attached to blade 25. The vibration excitation system is designed to make each blade in the first rotor blade row vibrate in the first bending mode. The estimation method therefore assumes that the blade is vibrating at the excitation frequency, and in the mode shape of the first bending mode. This appendix begins by providing the derivation of the estimation method. The amplitude of the component of the force perpendicular to the root existing at an excitation frequency of 660 Hz is then estimated.

G.1 Method for estimating forces

The solution to equation (2.2.1), for a mechanical system undergoing underdamped forced vibration, is expressed by equation (2.2.15). As explained in section 2.2.3, equation (2.2.15) consists of a complimentary solution and a particular solution. The complimentary solution vanishes as time increases. In the case of each rotor blade, the particular solution is likely to contain components at the excitation frequency and the nozzle bypass frequency. Consider only the component at the excitation frequency. Assume that this component consists of the blade vibrating in the first bending mode at the excitation frequency.

$$\mathbf{d}_{\text{part}}(t) = a\mathbf{u}_1 \sin(\omega_{\text{ef}} t) \tag{G.1.1}$$

In equation (G.1.1), a is a constant representing the amplitude of the component at the excitation frequency. Converting equation (G.1.1) to the modal coordinate system, by applying the inverse of the transformation in equation (2.2.5), results in equation (G.1.2).

$$\mathbf{q} = a\mathbf{P}^{-1}\mathbf{u}_1 \sin(\omega_{\text{ef}} t) \tag{G.1.2}$$

Solving equation (2.2.3) for $\mathbf{P}^{-1}$ and substituting the resulting expression into equation (G.1.2) yields equation (G.1.3).

$$\mathbf{q} = a\mathbf{P}^T\mathbf{M}\mathbf{u}_1 \sin(\omega_{\text{ef}}t) = b\sin(\omega_{\text{ef}}t) \begin{bmatrix} \mathbf{v}_1\mathbf{M}\mathbf{v}_1 \\ \mathbf{v}_2\mathbf{M}\mathbf{v}_1 \\ \vdots \\ \mathbf{v}_n\mathbf{M}\mathbf{v}_1 \end{bmatrix} \tag{G.1.3}$$

The vector $\mathbf{u}_1$ only differs from $\mathbf{v}_1$ by a constant multiple. The product of a and this constant multiple has been replaced in equation (G.1.3) by the constant b.

Equation (2.2.3) is equivalent to the two conditions expressed by equations (G.1.4a) and (G.1.4b).

$$\mathbf{v}_i\mathbf{M}\mathbf{v}_i = 1 \tag{G.1.4a}$$

$$\mathbf{v}_i\mathbf{M}\mathbf{v}_j = 0 \quad i \neq j \tag{G.1.4b}$$

Applying the conditions expressed by equations (G.1.4a) and (G.1.4b) to equation (G.1.3) produces equation (G.1.5).

$$\mathbf{q} = b\sin(\omega_{\text{ef}}t) \begin{bmatrix} 1 \\ 0 \\ \vdots \\ 0 \end{bmatrix} \tag{G.1.5}$$

The expressions for $\dot{\mathbf{q}}$ and $\ddot{\mathbf{q}}$ can be found by simply differentiating equation (G.1.5) with respect to time.

$$\dot{\mathbf{q}} = b\omega_{\text{ef}}\cos(\omega_{\text{ef}}t) \begin{bmatrix} 1 \\ 0 \\ \vdots \\ 0 \end{bmatrix} \tag{G.1.6}$$

$$\ddot{\mathbf{q}} = -b{\omega_{\text{ef}}}^2\sin(\omega_{\text{ef}}t) \begin{bmatrix} 1 \\ 0 \\ \vdots \\ 0 \end{bmatrix} \tag{G.1.7}$$

Substituting equations (G.1.5), (G.1.6), and (G.1.7) into equation (2.2.6) and solving for $\mathbf{r}$ results in equation (G.1.8). In this case, $\mathbf{r}$ represents the component of the blade force that is responsible for exciting $\mathbf{d}_{\text{part}}(t)$.

$$\mathbf{r}(t) = b(\mathbf{P}^T)^{-1} \begin{bmatrix} 1 \\ 0 \\ \vdots \\ 0 \end{bmatrix} \left(({\omega_{\mathrm{n},1}}^2 - {\omega_{\mathrm{ef}}}^2) \sin(\omega_{\mathrm{ef}} t) + 2\zeta_1 \omega_{\mathrm{n},1} \omega_{\mathrm{ef}} \cos(\omega_{\mathrm{ef}} t) \right) \tag{G.1.8}$$

Finally, solving equation (2.2.3) for $(\mathbf{P}^T)^{-1}$, substituting the resulting expression into equation (G.1.8), and simplifying yields equation (G.1.9).

$$\mathbf{r}(t) = b\mathbf{M}\mathbf{v}_1 \left(({\omega_{\mathrm{n},1}}^2 - {\omega_{\mathrm{ef}}}^2) \sin(\omega_{\mathrm{ef}} t) + 2\zeta_1 \omega_{\mathrm{n},1} \omega_{\mathrm{ef}} \cos(\omega_{\mathrm{ef}} t) \right) \tag{G.1.9}$$

The sinusoids and cosinusoids on the right hand side of the expression can be converted to the following form by making use of trigonometric identities.

$$\mathbf{r}(t) = \hat{\mathbf{r}} \sin(\omega_{\mathrm{ef}} t + \phi_{\mathrm{ef}}) \tag{G.1.10}$$

The values of $\hat{\mathbf{r}}$ and ϕ_{ef} are given by equations (G.1.11) and (G.1.12), respectively. Equations (G.1.11) and (G.1.12) allow $\hat{\mathbf{r}}$ and ϕ_{ef} to be calculated provided that ζ_1, $\omega_{\mathrm{n},1}$, ω_{ef}, $\mathbf{M}$, $\mathbf{v}_i$ and b are known.

$$\hat{\mathbf{r}} = b\sqrt{({\omega_{\mathrm{n},1}}^2 - {\omega_{\mathrm{ef}}}^2)^2 + (2\zeta_1 \omega_{\mathrm{n},1} \omega_{\mathrm{ef}})^2}\mathbf{M}\mathbf{v}_1 \tag{G.1.11}$$

$$\phi_{\mathrm{ef}} = \arctan\left(\frac{2\zeta_1 \omega_{\mathrm{n},1} \omega_{\mathrm{ef}}}{{\omega_{\mathrm{n},1}}^2 - {\omega_{\mathrm{ef}}}^2} \right) \tag{G.1.12}$$

G.2 Estimation of excitation force

Equation (G.1.11) was used to estimate the component of the force perpendicular to the root that exists at the excitation frequency. The data of Van der Spuy *et al.* (2012), presented in appendix B, was used for this estimate. The data of Van der Spuy *et al.* (2012) was collected with the vibration excitation system set to an excitation frequency of 660 Hz and a supply pressure of 2.5 bar, and the 0 ND excitation mode. The single blade FE model was used in section 4.3.1 to calculate the mode shape and the natural frequency of the first bending mode. The values of $\omega_{\mathrm{n},1}$ and $\mathbf{v}_1$ are therefore already known. The mass matrix $\mathbf{M}$ was obtained by opening the FE model in Ansys Mechanical APDL and then writing the mass matrix to a text file. The amplitude of the 660 Hz component of the tip deflection perpendicular to the root, measured by Van der Spuy *et al.* (2012), was 0.089 mm. The amplitude of the tip deflection perpendicular to the root was used to calculated the value of b.

The values of all of the variables in equation (G.1.11) are known except for the value of ζ_1. Calculations by Van der Spuy *et al.* (2012) showed that the

structural damping ratio for the first bending mode was less than 0.02. However, the calculations did not provide the exact value of the damping ratio. The 660 Hz component of force perpendicular to the blade root was therefore determined for a range of possible damping ratios. This provided a lower and an upper bound for the 660 Hz component of the force. The range of damping ratios considered is expressed by equation (G.2.1).

$$0 < \zeta_1 < 0.02 \tag{G.2.1}$$

The value of $\hat{\mathbf{r}}$ was determined for the range of ζ_1 in equation (G.2.1). The vector component of each element of $\mathbf{r}$, in the direction perpendicular to the root, was then calculated. Finally, the vector components were all summated to find the resultant force in the direction perpendicular to the root. The amplitude of the 660 Hz component of the resultant force perpendicular to the root is expressed by equation (G.2.2).

$$0.0359 \text{ N} < \hat{r}_{\text{perp}} < 0.239 \text{ N} \tag{G.2.2}$$

Appendix H

Initial conditions for the FSI simulations

Initial conditions were required for both the CFD model and the FE model that make up each FSI model. The initial conditions of each CFD model were at first set equal to the same steady state solution that had been used as the initial conditions of that CFD model during the transient analysis in section 5.9. Correspondingly, the initial conditions of each FE model was set so that the blades were initially undeformed and stationary. However, it was found that defining the initial conditions of each FSI model in this way caused each blade to exhibit spurious vibrations at the natural frequency of the first bending mode. This appendix begins by presenting the results the original analysis performed, using the 0 ND FSI model. The derivation of the more appropriate set of initial conditions for each FSI model is then considered.

H.1 Original analysis

The 0 ND FSI model was used to simulate the scenario where the compressor is operating without the vibration excitation system functioning. The velocity components on the inlet and patch boundaries was set equal to the undisturbed axial velocity profile in appendix C that was measured for the 32 hole rotors. The initial conditions of the 0 ND CFD model was set equal to the steady state solution that was used as the initial conditions of the 0 ND CFD model in section 5.9 for the 32 hole rotors. The initial conditions of the 0 ND FE model was specified so that the blade is undeformed and stationary at the start of the simulation. The vibration of the blades was simulated for 200 time steps at a time step size of 5.4112×10^{-5} s. The number of stagger iterations per time step was set equal to 2 iterations.

The tip displacement, in the direction perpendicular to the root of blade 1, is plotted in figure H.1 as a function of time. The tip displacement predicted by the 0 ND FSI model was found to be identical for all three blades. This was

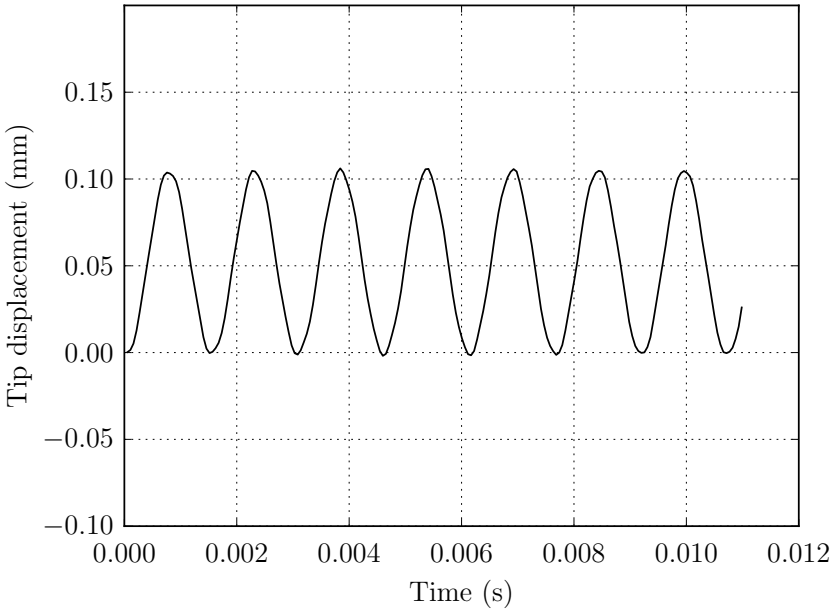

Figure H.1: Tip displacement perpendicular to the root calculated by the 0 ND FSI model for the undisturbed compressor flow field and $\zeta_1 = 0$.

also the case for the forces acting on the blades in the 0 ND FSI model. The tip displacement perpendicular to the root in figure H.1 appears to be sinusoidal with time. This suggests that the blade is vibrating only in a single mode. The frequency of vibration was estimated from the time between successive peaks to be 653 Hz. This value is close to the natural frequency of the first bending mode computed in section 4.4. In addition, the amplitude of vibration remains constant with time. Each blade therefore appears to be experiencing undamped free vibration in its first bending mode. The amplitude and mean value of the tip deflection perpendicular to the root both have a value of 0.053 mm.

Raubenheimer (2011) measured the vibration of blade 25, in the actual compressor, with the compressor operating at a rotation speed of 3000 rpm, a mass flow rate 2.5 kg/s and an undisturbed flow field. Equation (3.3.2b) was then used by Raubenheimer (2011) to estimate the tip displacement perpendicular to the root from the measured bridge voltage. The rotation speed and mass flow rate selected for the 0 ND FSI model was 2880 rpm and 2.51 kg/s, respectively. The response at the natural frequency of the first bending mode, estimated by Raubenheimer (2011), was therefore based on strain data collected at a slightly higher rotation speed than that selected for the 0 ND FSI model. However, the difference in rotation speed was deemed small enough that response of the blade at a rotation speed of 2880 rpm should be similar to the blade displacement estimated by Raubenheimer (2011) at 3000 rpm.

The amplitude of the component of the tip displacement perpendicular to the root, existing at the natural frequency of the first bending mode, was estimated by Raubenheimer (2011) to be 0.006 mm. As presented in appendix B, the am-

plitude of the vibration induced by the vibration excitation system was estimated by Van der Spuy *et al.* (2012) to be approximately 0.1 mm. The amplitude of the tip displacement perpendicular to the root, plotted in figure H.1, is 780 % larger than the amplitude estimated by Raubenheimer (2011). The amplitude of vibration predicted by the 0 ND FSI model is therefore significantly larger than the amplitude estimated by Raubenheimer (2011) from the measured bridge voltage.

The mean value of the tip deflection in figure H.1 represents the equilibrium position about which the vibration of the blade occurs. Even though the blade is undeformed at the start of the simulation, the blade tip is deflected 0.053 mm from the equilibrium position. Since the blade is experiencing undamped free vibration, the blade will continue vibrating indefinitely at an amplitude of 0.053 mm. The blade response predicted by the 0 ND FSI model is therefore spurious as it is purely caused by the initial conditions of the FSI model.

H.2 Derivation of new initial conditions

If the spurious vibrations in figure H.1 are not eliminated, they will be present in the blade response predicted by the 0 ND FSI model during the simulations of the vibration excitation system. A large amount of structural damping was therefore used to damp out the spurious vibrations. Once the spurious vibrations had decayed away, structural damping was deactivated. The resulting solution was then used as the initial conditions of the FSI model. Two sets of initial conditions were derived in this manner for the 0 ND FSI model for the 32 hole rotors and 16 hole rotors. A separate set of initial conditions was also derived for the +2 ND FSI model for the 32 hole rotors.

It was stated in section 2.2.2 that the damping model used by Ansys Mechanical is Rayleigh damping. According to the Rayleigh damping model, the damping ratio for each mode is expressed by equation (2.2.10). The value of β for each FE model was set equal to 1.08×10^{-4} s^{-1} in Ansys Mechanical. Ansys Mechanical automatically sets the value of α equal to zero. This yielded a damping ratio for the first bending mode of 0.22. The appropriate undisturbed axial velocity profile in appendix C was applied to both the inlet and patch boundaries for the derivation of the initial conditions of the 0 ND FSI model for either the 32 hole rotors or the 16 hole rotors. The undisturbed axial velocity profile measured for the 32 hole rotors was applied to both the inlet and patch boundaries for the derivation of the initial conditions of the +2 ND FSI model.

Figure H.2 shows the tip displacement of blade 2, in the direction perpendicular to the root, calculated during the simulation performed to obtain the initial conditions of the 0 ND FSI model for the 32 hole rotors. The tip displacements obtained for blade 1 and blade 3 were again identical to that of blade 2. As shown figure H.2, the amplitude of the tip displacement had decreased below 0.006 mm after 200 time steps. This is within the amplitude estimated by Raubenheimer (2011). The solution in figure H.2 was therefore used as the initial conditions

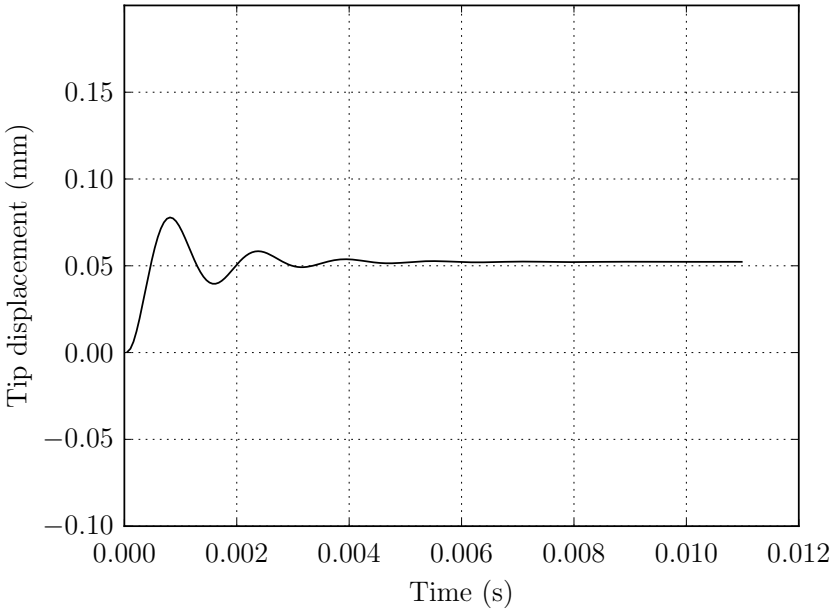

Figure H.2: Tip displacement perpendicular to the root calculated by the 0 ND FSI model for the undisturbed compressor flow field and $\zeta_1 = 0.22$.

of the 0 ND FSI model for the simulation of the vibration excitation system for the 32 hole rotors.

Appendix I

Sensitivity to stagger iterations

This appendix discusses the simulations performed in order to determine the sensitivity of the 0 ND FSI model to the number of stagger iterations per time step. The 0 ND FSI model was used to simulate the scenario where the vibration excitation system has been fitted with the 32 hole rotors, and is set to the 0 ND mode, an excitation frequency of 660 Hz, and a supply pressure of 2.5 bar. A transient CFD analysis of this scenario was already performed in section 5.9.1. For each FSI simulation, the initial conditions of the 0 ND CFD model was set to the same steady solution used for the transient CFD analysis. Correspondingly, the initial condition of the 0 ND FE model was set so that the blades were undeformed and stationary at the start of the simulation.

Three separate FSI simulations were performed with the number of stagger iterations per time step set equal to 1 iteration, 2 iterations, and 6 iterations. As explained in section 2.4, executing only 1 stagger iteration per time step represents a weak staggered coupling. Executing 6 stagger iterations per time step constitutes a strong staggered coupling. Executing 2 stagger iterations per time step represents the minimum number of stagger iterations required to achieve a strong staggered coupling. The time step size selected for each simulation was 5.4112×10^{-5} s. Each simulation was run for 200 time steps. This is equivalent to approximately half of a rotation of the compressor rotor. The duration of each simulation was selected to be just long enough to evaluate the effect of the number of stagger iterations per time step on the solution.

The force perpendicular to the root, acting on blade 1, is plotted in figure I.1 as a function of time for 1 stagger iteration, 2 stagger iterations, and 6 stagger iterations per time step. All three curves in figure I.1 are coincident. Performing more than 1 stagger iteration per time step therefore has no influence on the blade force computed by the 0 ND FSI model. This indicates that a weak staggered coupling is sufficient for predicting a value for the blade force that is independent of the number of stagger iterations.

The tip displacement of blade 1, in the direction perpendicular to the root, is plotted as a function of time in figure I.2 for each number of stagger iterations.

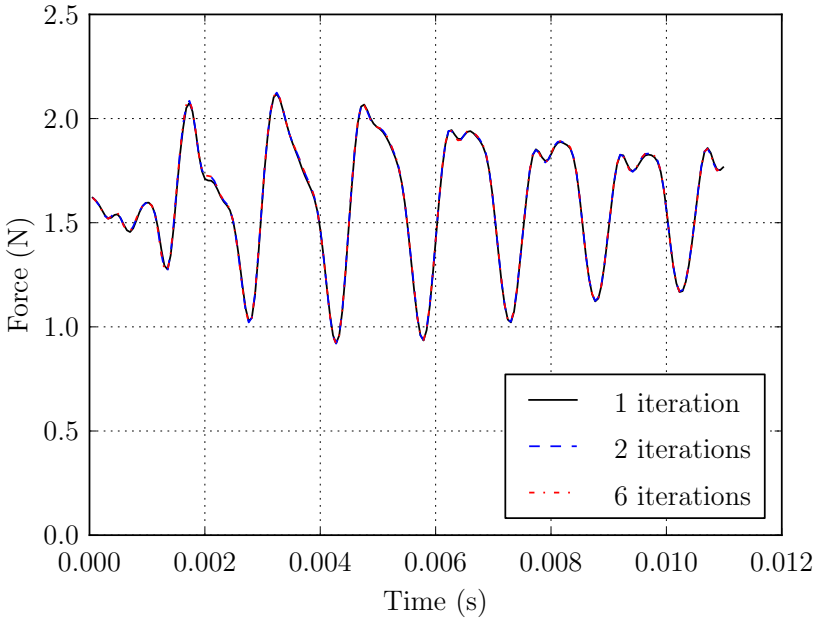

Figure I.1: Force perpendicular to the root plotted as a function of time for different numbers of stagger iterations per time step.

As was observed for the blade force, the curves of tip displacement obtained for 2 stagger iterations and 6 stagger iterations per time step are again coincident. However, there is a visible difference between the curve obtained for 1 stagger iteration per time step and the curves obtained for 2 stagger iterations and 6 stagger iterations per time step. The curve obtained for 1 stagger iteration per time step begins to lag behind the other two curves as time increases. This indicates that the frequency of vibration obtained when using a weak staggered coupling is slightly lower than that obtained when using a strong staggered coupling.

The computation times required, per time step, to execute 1 stagger iteration, 2 stagger iterations and 6 stagger iterations were 6 minutes, 21 minutes, and 59 minutes, respectively. Using a strong staggered coupling with 2 stagger iterations therefore results in a computation time that is 3.5 times longer than if weak staggered coupling is used. Using a strong staggered coupling with 6 stagger iterations, instead of a weak staggered coupling, causes the computation time to increase by a factor of 10.5 times.

The results in figure I.1 and figure I.2 show that using a weak staggered coupling leads to the solution of the 0 ND FSI model that is visibly different to that obtained when using a strong staggered coupling. However, the difference between the solution obtained using a weak staggered coupling and the solution obtained using a strong staggered coupling is small. In addition, using a weakly coupled approach, as opposed to a strongly coupled staggered approach, reduces the computation required by at least a factor of 3.5 which is significant. A weak staggered coupling was therefore employed for each FSI model.

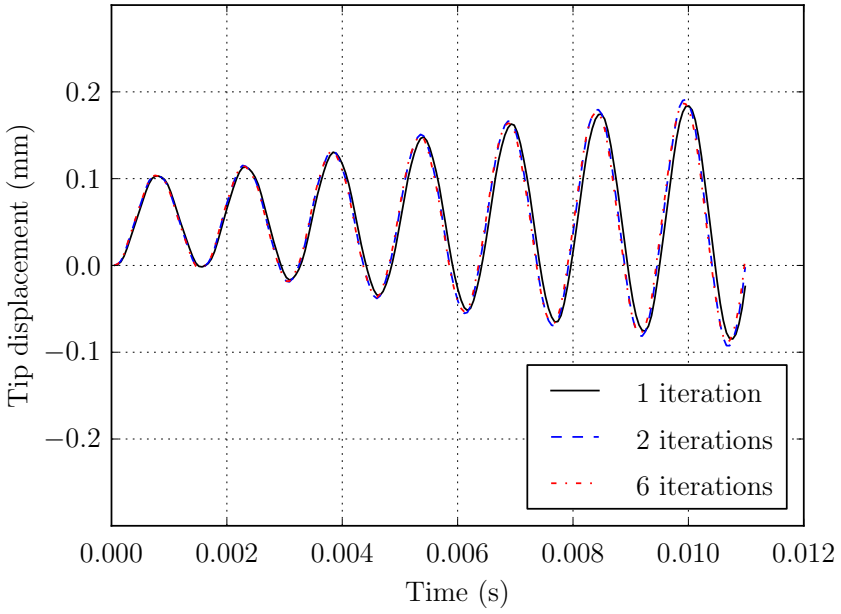

Figure I.2: Tip displacement perpendicular to the root plotted as a function of time for different numbers of stagger iterations per time step.

Appendix J

Blade force from the FSI models

This appendix presents the blade forces calculated during the FSI simulations in chapter 6. The blade force computed using the 0 ND FSI model during the simulations of 0 ND mode are first presented. This is followed by the blade force obtained using the +2 ND FSI model during the simulation of the +2 ND model. In each case, the blade force predicted by the FSI model is compared to the results of the corresponding transient CFD simulation in section 5.9.

J.1 Blade forces obtained for the 0 ND mode

The force perpendicular to the root, acting on blade 2 in the 0 ND FSI model, is plotted as a function of time in figure J.1. As was observed during the transient CFD simulations of the 0 ND mode in section 5.9.1, the force perpendicular to the root in figure 5.10 settled into a periodic steady state pattern after 0.025 s. Approximately two periods of this steady state pattern are visible in figure 5.10 after this point in time. The force perpendicular to the root calculated by the 0 ND FSI model for the 16 hole rotors was also observed to settle into a periodic steady state pattern after 0.025 s.

The FFT of the force perpendicular to the root, acting on blade 2 in the 0 ND FSI model, is plotted in figure J.2 for both the 32 hole rotors and 16 hole rotors. The blade force computed during the transient CFD simulations in section 5.9.1 exhibited components at 660 Hz and 672 Hz, as well as the harmonics of these two components. In order to minimise spectral leakage, the number of samples used to calculate each FFT was selected so that the window of the FFT contained a whole number of periods of each of these components. The samples were also taken from the region in the time domain after the force perpendicular to the root had settled into a steady state pattern. Each FFT was therefore calculated from the last 3080 samples in the time domain. The resulting FFT had samples in the frequency domain that were spaced at 6 Hz intervals from 0 Hz to 9240 Hz.

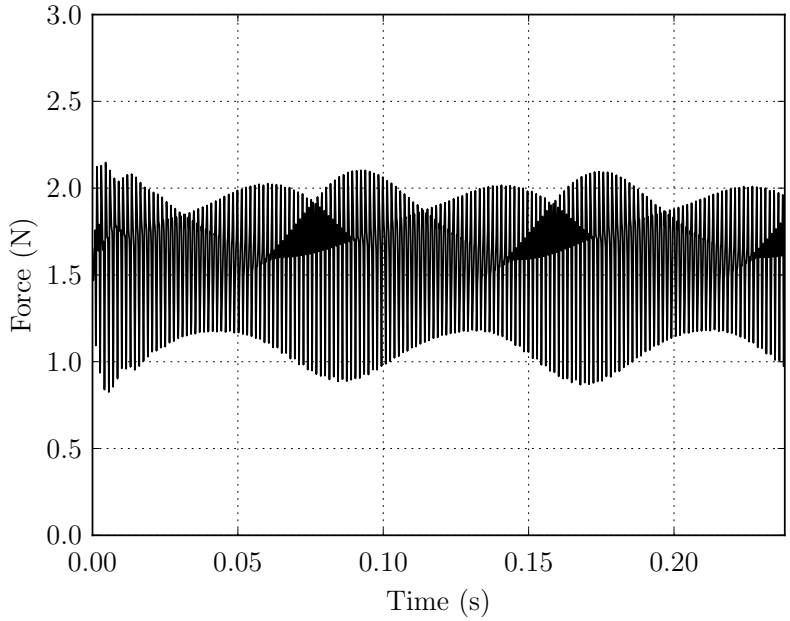

Figure J.1: Force perpendicular to the root calculated by the 0 ND FSI model for blade 2 for the 32 hole rotors and an excitation frequency of 660 Hz.

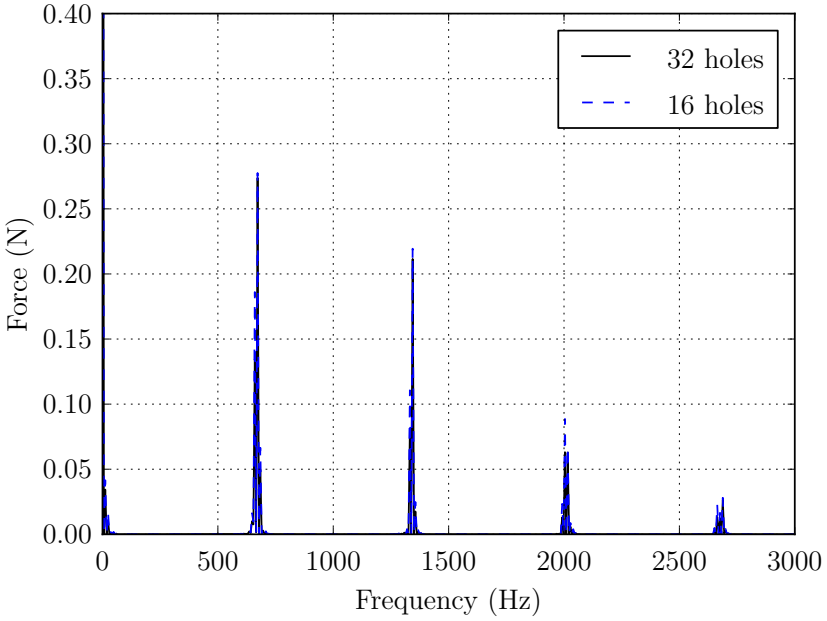

Figure J.2: FFT of the force perpendicular to the root calculated by the 0 ND FSI model for blade 2 for an excitation frequency of 660 Hz.

The FFTs calculated for the three blades in the 0 ND FSI model were all identical for the 32 hole rotors. This was also the case for the FFTs computed for the three blades for the 16 hole rotors. Each FFT exhibited the same clusters of peaks near 670 Hz, 1340 Hz, 2010 Hz, and 2680 Hz that were observed during the transient CFD simulations. The zoomed in view in figure J.3 shows that that the cluster of peaks near 670 Hz is composed of two major components at 660 Hz and 672 Hz, and two minor components at 648 Hz and 684 Hz.

The components at 660 Hz and 672 Hz are the components at the excitation frequency and the nozzle bypass frequency, respectively. As already mentioned in section 5.9.1, it is unclear what the cause is of the peaks at 648 Hz and 684 Hz. The magnitude of the 660 Hz component of each blade in the 0 ND FSI model had a magnitude of approximately 0.135 N for the 32 hole rotors, and 0.186 N for the 16 hole rotors. Both of these values are only 5 % lower than the magnitude of the 660 Hz component calculated for the same rotor disk type during the transient CFD analyses.

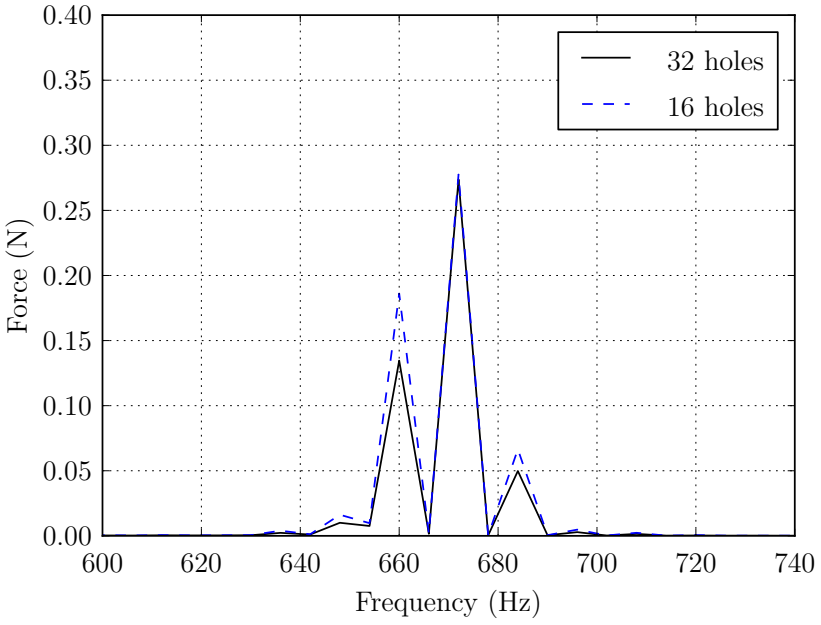

Figure J.3: Zoomed in view of the FFT of the force perpendicular to the root calculated by the 0 ND CFD model for an excitation frequency of 660 Hz.

J.2 Blade forces obtained for the +2 ND mode

The force perpendicular to the blade root acting on blade 14 in the +2 ND FSI model is plotted in figure J.4 as a function of time for the 32 hole rotors. As observed during the transient CFD simulations in section 5.9.2, the force perpendicular to the root settled into a steady state pattern after 0.025 s. The

force acting on each of the other blades in the +2 ND FSI model also settled into a steady state pattern after 0.025 s.

Figure J.4 contains the FFTs of the force perpendicular to the blade root calculated for blade 3 and blade 14 in the +2 ND FSI model. Each FFT was computed using the last 3080 samples in the time domain. The samples were therefore selected from the portion of the time domain after the force perpendicular to the root had settled into a steady state pattern. The number of samples used to calculate the FFT was chosen so that the window of the FFT was contained a whole number of periods of the components at 660 Hz and 672 Hz, as well as the harmonics of these two components. This was done in order to minimize spectral leakage. The resulting FFT had samples in the frequency domain that were spaced 6 Hz apart from 0 Hz to 9240 Hz.

The FFTs computed for the blades in the +2 ND FSI model were all identical. As was observed for the 0 ND mode, the FFT shows clusters of peaks near 670 Hz, 1340 Hz, 2010 Hz, and 2680 Hz. The same components were also visible in the FFT of the blade force obtained during the transient CFD simulation of the +2 ND mode in section 5.9.2. The zoomed in view of the FFT in figure J.6 again shows that the cluster of peaks near 670 Hz has two prominent components at 660 Hz and 672 Hz, and two minor components at 648 Hz and 684 Hz. The clusters of peaks at 1340 Hz, 2010 Hz and 2680 Hz are the harmonics of the 660 Hz and 672 Hz components. The magnitude of the 660 Hz component of each blade had a value of 0.190 N. This value is only 7 % lower than the value obtained for the 660 Hz component from the transient CFD simulations in section 5.9.2.

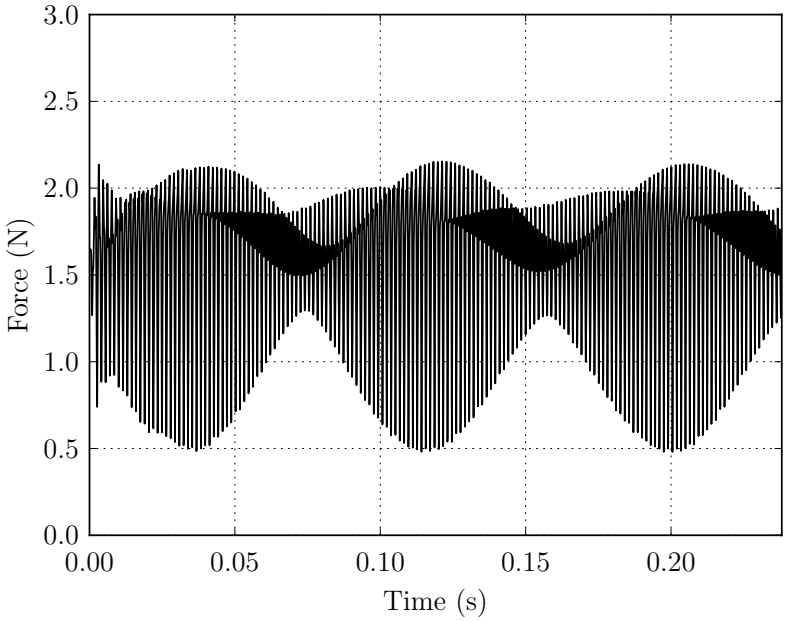

Figure J.4: Force perpendicular to the root calculated by the +2 ND FSI model for blade 14 for an excitation frequency of 660 Hz.

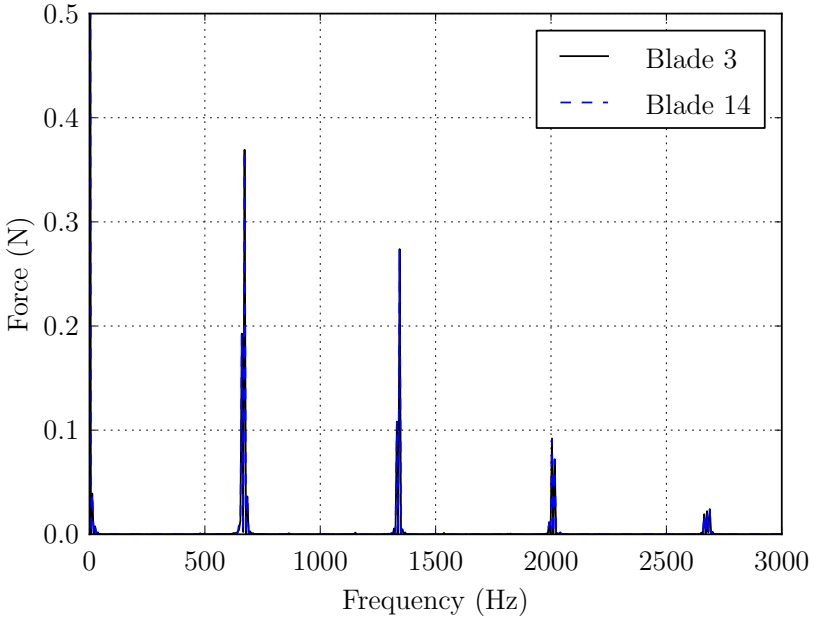

Figure J.5: FFT of the force perpendicular to the root calculated by the +2 ND FSI model for blade 3 and blade 14 for an excitation frequency of 660 Hz.

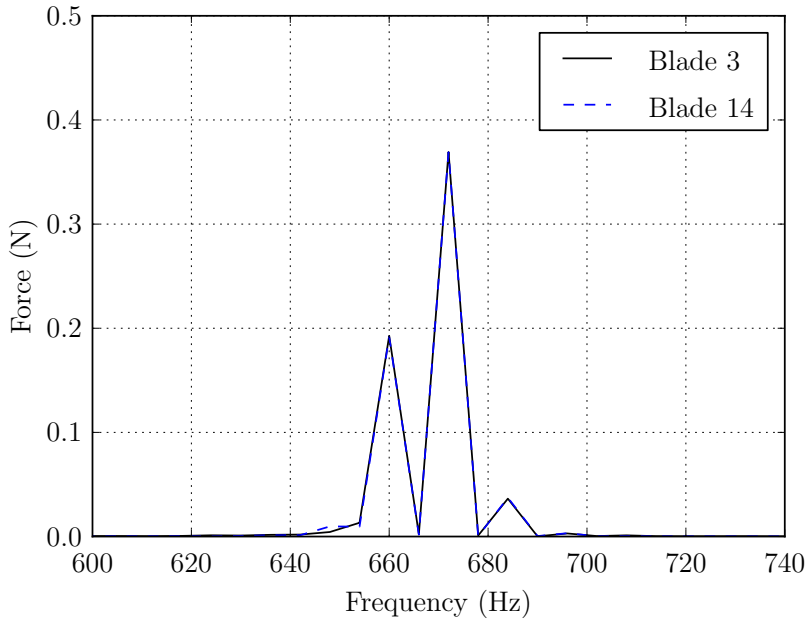

Figure J.6: Zoomed in view of the FFT of the force perpendicular to the root calculated by the +2 ND FSI model for blade 3 and blade 14 for an excitation frequency of 660 Hz.

List of References

(2012*a*). *Ansys CFX Reference Guide, Release 14.5.* Ansys Inc., Canonsburg.

(2012*b*). *Ansys CFX-Solver Modeling Guide, Release 14.5.* Ansys Inc., Canonsburg.

(2012*c*). *Ansys CFX-Solver Theory Guide, Release 14.5.* Ansys Inc., Canonsburg.

(2012*a*). *Ansys Mechanical APDL and Mechanical Appplications Theory Reference, Release 14.5.* Ansys Inc., Canonsburg.

(2012*b*). *Ansys Mechanical APDL Element Reference, Release 14.5.* Ansys Inc., Canonsburg.

(2012*c*). *Ansys Mechanical Application User's Guide, Release 14.5.* Ansys Inc., Canonsburg.

Armstrong, E.K. and Stevenson, M.A. (1960). Some practical aspects of compressor blade vibration. *Journal of the Royal Aeronautical Society*, vol. 64, pp. 117–130.

Ball, S.J., Ashforth-Frost, S., Jambunathan, K. and Whitney, C.F. (1999). Appraisal of a hot-wire temperature compensation technique for velocity measurements in non-isothermal flows. *International Journal of Heat and Mass Transfer*, vol. 42, pp. 3097–3102.

Budynas, R., Shigley, J. and Nisbett, J. (2003). *Shigley's Mechanical Engineering Design.* Eigth edn. McGraw-Hill, New York.

Cook, R.D. (1995). *Finite Element Modelling for Stress Analysis.* John Wiley & Sons, Inc., New York.

Cumpsty, N.A. (1989). *Compressor Aerodynamics.* Longman, Harlow.

El-Aini, Y., deLaneuville, R., Soner, V. and Capeco, V. (1997). High-cycle fatigue of turbomachinery components industry perspectives. *AIAA*, vol. 97, p. 3365.

Farhat, C., Van der Zee, K.G. and Geuzaine, P. (2006). Provably second-order time-accurate loosely-coupled solution algorithms for transient nonlinear computational aeroelasticity. *Computer Methods in Applied Mechanics and Engineering*, vol. 195, pp. 1973–2001.

Figliola, R.S. and Beasley, D.E. (2006). *Theory and Design of Mechanical Measurements.* 4th edn. John Wiley and Sons, Inc., New Jersey.

Gill, A. (2006). *A Comparison between Stall Prediction Models for Axial Flow Compressors*. Master's thesis, Mechanical Engineering, Stellenbosch University, Stellenbosch, South Africa.

Gill, A. (2012). *Four Quadrant Axial Flow Compressor Performance*. Ph.D. thesis, Mechanical Engineering, Stellenbosch University, Stellenbosch, South Africa.

Gnesin, V., Rzadkowski, R. and Kolodyazhnaya, L. (2000). A coupled fluid-structure analysis for 3d flutter in turbomachines. In: *Proceedings of ASME Turbo Expo*. Munich.

Im, H.S. and Zha, G.C. (2012). Simulation of non-synchronous blade vibration of an axial compressor using a fully coupled fluid/structure interaction. In: *Proceedings of ASME Turbo Expo*. Kluwer Academic Publishers, Copenhagen.

Inman, D.J. (2009). *Engineering Vibrations*. 3rd edn. Pearson Education, Inc., New Jersey.

Matthies, H.G. and Steindorf, J. (2003). Strong coupling methods. In: *Analysis and Simulation of Multifield Problems*. Springer:Verlag.

Michler, C. (2005). *Efficient Numerical Methods for Fluid-Structure Interaction*. Master's thesis, Technische Universiteit Delft, Delft.

Piperno, S. and Farhat, C. (1997). Design and evaluation of staggered partitioned procedures for fluid-structure interaction simulations. In: *Fifth World Congress on Computational Mechanics*. San Francisco.

Raubenheimer, G.A. (2011). *Vibration Excitation of Axial Compressor Rotor Blades*. Master's thesis, Mechanical Engineering, Stellenbosch University, Stellenbosch, South Africa.

Srinivasan, A.V. (1997). Flutter and resonant vibration characteristics of engine blades. *Journal of Engineering for Gas Turbines and Power*, vol. 119, no. 4, pp. 742–775.

Storti, M.A., Nigro, N.N., Paz, R.R., Dalcn, L.D., Ros Rodriguez, G.A. and Lpez, E. (2006). Fluid-structure interaction with a staged algorithm. *Mecánica Computacional*, vol. XXV, pp. 887–905.

Vaassen, J.M., DeVincenzo, P., Hirsch, C. and Leonard, B. (2011). Strong coupling algorithm to solve fluid-structure-interaction problems with a staggered approach. *International Journal of Heat and Mass Transfer*, vol. 12, no. 4, pp. 325–332.

Van der Spuy, J., Raubenheimer, G. and Gill, A. (2012). Future report no: Ftr-5-49. Deliverable report, Stellenbosch University.

Wegman, E.J., Dunn, D., Grobler, J.H. and Snedden, G. (2010). Future report no: Ftr-4-wp3-csir-9. Partner progress report, Council for Scientific and Industrial Research.

Zill, D.G. and Cullen, M.R. (2006). *Advanced Engineering Mathematics*. 3rd edn. Jones and Bartlett Publishers, Sudbury.